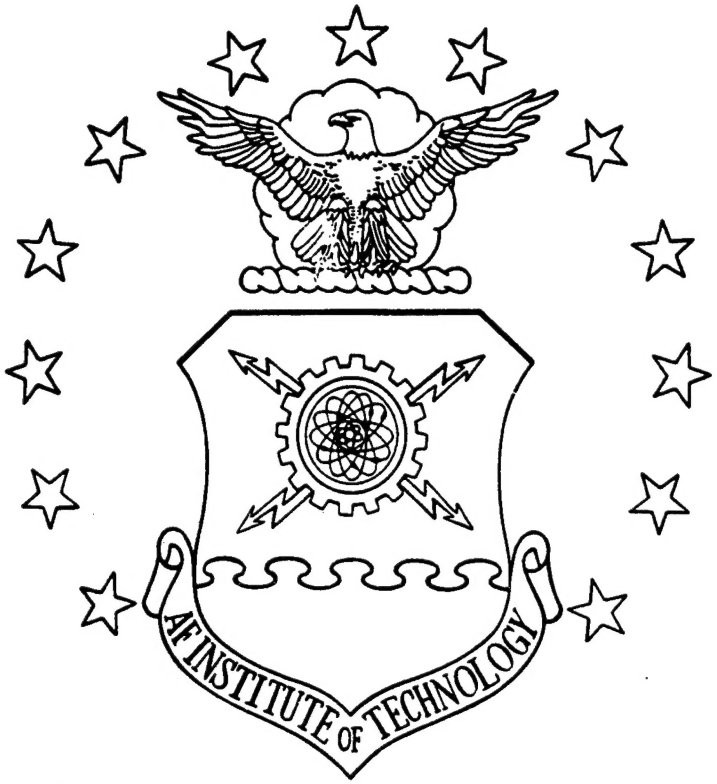

DEPARTMENT OF THE AIR FORCE

AIR UNIVERSITY

AIR FORCE INSTITUTE OF TECHNOLOGY

Wright-Patterson Air Force Base, Ohio

Investigation of the Optical Properties of Ordered Semiconductor Materials

DISSERTATION

Jack E. McCrae, Jr., Maj, USAF

"The views expressed in this dissertation are those of the author and do not reflect the official policy or position of the Department of Defense or the U. S. Government"

AFIT/DS/ENP/97-10

INVESTIGATION OF THE OPTICAL PROPERTIES OF ORDERED SEMICONDUCTOR MATERIALS

DISSERTATION

Presented to the Faculty of the Graduate School of Engineering

of the Air Force Institute of Technology

Air University

In Partial Fulfillment of the

Requirements for the Degree of

Doctor of Philosophy

Jack E. McCrae, Jr., B.S., M.S.

Major, USAF

January 1997

Approved for public release; distribution unlimited

AFIT/DS/ENP/97-03

Investigation of the Optical Properties of Ordered Semiconductor Materials

Jack E. McCrae, Jr.,
Maj, USAF

Approved:

Committee Chairman: Robert L Hengehold — Dr Hengehold — 1/21/97

Committee Member: Yung Kee Yeo — Dr Yeo — 1/21/97

Committee Member: Thomas W. Listerman — Dr Listerman — 1/21/97

Committee Member: Melvin C Ohmer — Dr Ohmer — 1/21/97

Dean's Representative: Alan V. Lair — Dr Lair — 1/21/97

Accepted:

Dean, School of Engineering — 12/5/97

Preface

I want to thank my research advisor Dr Robert Hengehold, and the rest of my research committee, Dr Yung Kee Yeo, Dr Mel Ohmer, and Dr Thomas Listerman for their assistance with this dissertation. I owe Dr Yeo additional thanks for his tremendous effort in guiding me through the publication of two papers while I was at AFIT. I thank Dr Ohmer for providing me with the samples upon which this research is based, and also for many useful discussions about this field. I want to thank my wife Kim for support through all phases of this project. Many other AFIT students helped me out along the way, so I'll just mention my contemporaries who had to endure the whole while with me: Roy Calfas, Bill Cooley, Rob Franklin, Greg Vansuch, Dave Lee (Honorary non-December Grad), and of course my wife Kim again. Many thanks to Belinda Johnson and Greg Smith for their assistance with this project too.

Table of Contents

List Of Figures

List Of Tables

Abstract

Optical Studies have been conducted upon $CdGeAs_2$ and $ZnGeP_2$, two of the most promising semiconductors being developed for mid-infrared non-linear optics applications. These experiments included photoluminescence (PL) studies of both compounds as well as photoreflectance (PR) measurements upon $CdGeAs_2$. In addition, Hall effect measurements were carried out upon $CdGeAs_2$, to aid in interpretation of the optical data. PL was measured as a function of laser power, sample temperature, and crystal orientation for $CdGeAs_2$, the optical and defect properties of this ordered semiconductor being largely unknown. One broad weak peak near 0.38 eV, and another somewhat narrower and often far brighter peak near 0.57 eV were found by low temperature (4 K) PL measurements. The high energy PL peak shifts first towards lower, then higher, and back to lower energies again as the temperature increases from 2.2 to 295 K. This high energy peak is attributed to donor-acceptor pair dominant transitions at low temperatures, but it is attributed to band-to-band transitions dominant transitions at higher temperatures. Strongly polarized PL was observed with the E field of the PL parallel to the material's c-axis. A polarization ratio as high as 6:1 was observed. PL on $ZnGeP_2$ in the mid-IR revealed a previously unreported PL peak near 0.35 eV. PR measurements on $CdGeAs_2$ allowed the estimation of the bandgap as a function of temperature. The low temperature bandgap proved to be lower than that reported for electroreflectance measurements on other samples of this compound. Hall effect measurements on $CdGeAs_2$ reveals the dominant acceptor level lies about 120 meV above the valence band.

Chapter I. Introduction.

The Air Force has great interest in mid-infrared (3-5 μm) laser devices for countermeasure and remote sensing applications. Since lasers operating in this wavelength region are presently quite limited in their capabilities, non-linear optical techniques can be used to cover this spectral range by halving or doubling the wavelength output from other lasers. The materials studied here, Cadmium Germanium Arsenide ($CdGeAs_2$) and Zinc Germanium Phosphide ($ZnGeP_2$) appear uniquely well suited for these purposes. $CdGeAs_2$ has the highest non-linear coefficient of any known compound and shows great promise for use in doubling the frequency of CO_2 lasers into the 5μm region. $ZnGeP_2$ shows great promise for use as the non-linear optical element in an optical parametric oscillator, a device which divides the output wavelength of a pump laser operating near 2μm into a pair of wavelength outputs tunable across the 3-5 μm region. Unfortunately, extrinsic optical absorption present in all samples of these crystals grown to date has hampered this utilization for these materials. While better and better crystals of these materials are being grown presently, progress is slow, and the source of this absorption is not fully understood. Poor understanding of the mechanisms underlying this extrinsic absorption makes it difficult to predict ways to reduce it and thus create better crystals. The purpose of this research is to better understand the fundamental optical properties and defect structures of these materials.

A photoluminescence (PL) study was conducted on $CdGeAs_2$ as a function of sample, polarization, temperature, and laser power. At low temperatures the PL spectrum consists of two main peaks: a weak peak is observed near 0.38 eV and a stronger peak is observed near 0.57 eV. These peaks are believed to be due to radiative recombination between donor-acceptor pairs (DAP's). The PL signal persisted up to room temperature where the spectrum consists of a single peak near 0.55 eV, believed to be due to band-to-

band recombination. Photoluminescence in the visible and mid-IR regions was also collected from $ZnGeP_2$, where the evidence suggested that both DAP's and free-to-bound transitions were involved in the luminescence observed.

Photoreflectance (PR) spectra were obtained from $CdGeAs_2$ to aid in the interpretation of the PL spectra. These spectra are used to estimate the bandgap of $CdGeAs_2$ as a function of temperature. The PR experiment was conducted at various temperatures, laser powers, and sample orientations, and upon several different samples as well. The results obtained indicate that the low temperature bandgap of the samples studied here is not as high as results reported by others.

Hall effect measurements on $CdGeAs_2$ were undertaken to try to identify the energy of the acceptor levels involved in PL. The energy level so obtained was too deep to be involved with the near band edge luminescence observed. These measurements showed that all the crystals studied were p-type.

The PR results serve to confirm that the room temperature PL observed is due to band-to-band recombination. The Hall effect results, considered in conjunction with the optical absorption spectra of these samples, demonstrates that both compensation and crystal quality need to be considered when attempting to explain the optical losses seen. Variations seen in the PL between these samples helps corroborates this conclusion.

The following chapter discusses the properties of chalcopyrite semiconductors and previous efforts in this area. Chapters 3, 4, and 5 detail the experiments conducted for this work involving PL, PR and the Hall Effect respectively. Overall conclusions and recommendations for future work are in chapter 6.

Chapter II. Background.

2.1. Crystals, Symmetry and Birefringence.

It is said that GaAs can do everything Si can do, plus it can emit light - the chalcopyrite semiconductors can take this one step further - they can, in principle at least, do everything Si and GaAs can do plus they can frequency double light. Non-linear optics has become the most important and most vigorously pursued application for ordered semiconductor materials. In order to be useful for non-linear optical applications such as frequency doubling, parametric amplification and oscillation, and sum and difference frequency mixing (all second order processes) a crystal must be birefringent (there are minor exceptions to this rule). Whether or not a crystal has the possibility of being birefringent can be determined from the crystal's atomic structure - it's point group symmetry. The chalcopyrite structure is closely related to the zincblende structure and can be constructed by taking two zincblende unit cells, stacking one on top of the other and placing the cations in a certain ordered fashion; this is illustrated in Fig. 1, which compares a typical chalcopyrite semiconductor ($ZnGeP_2$) to the mineral zincblende (ZnS). Due to this ordering of the cation sublattice most chalcopyrite crystals are also compressed slightly in the vertical direction, there is also a slight distortion of the location of the anion sites because the bond lengths will be slightly different to the differing cations. The cubic symmetry of the original zincblende structure is broken by the operations of ordering, compressing, and distorting the structure. Materials with cubic symmetry (e.g. Si and GaAs crystals) cannot be birefringent, and thus phase matching differing wavelengths of light is virtually impossible. The chalcopyrite structure has point group symmetry $\bar{4}2m$, which is a tetragonal symmetry group; these materials are normally uniaxial. A particular chalcopyrite material might be isotropic anyway, but this would be only coincidental. The amount of birefringence present helps

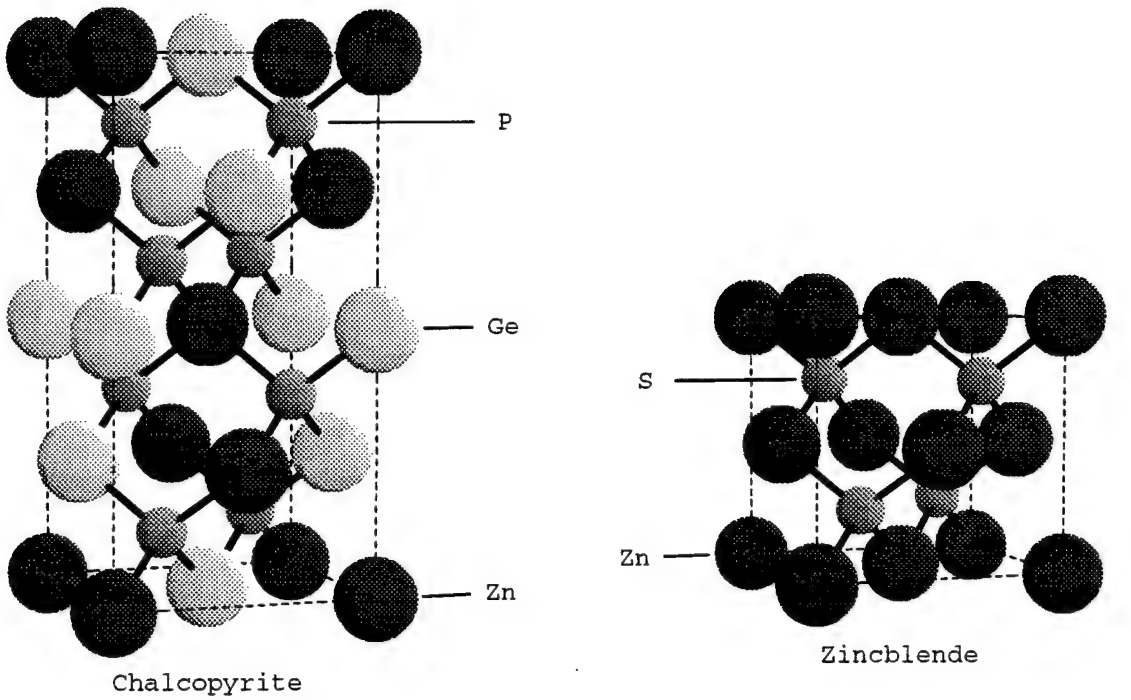

Figure 1. Chalcopyrite and Zincblende Crystal Structures Compared

determine the wavelength range over which a crystal can be used. Some materials, such as $ZnGeP_2$ and $CdGeAs_2$, have enough birefringence to be usable for non-linear optics over most of their ranges of transparency. $ZnGeAs_2$, on the other hand, appears to be nearly isotropic.

2.2. The Chalcopyrite Wigner-Seitz Cell and Brillouin Zone.

While the chalcopyrite unit cell can be constructed from two zincblende unit cells, the behavior of the primitive cells is a little more complex. The zincblende (and diamond structure as well) structure can be regarded as two interpenetrating face-centered cubic (FCC) lattices separated by one quarter of the body-diagonal. The primitive cell for zincblende is then that of the FCC lattice. For the zincblende structure every cation site is translationally equivalent to every other cation site. This is obviously not the case for chalcopyrites because half the cations are different elements, but it goes further than this - only half of the sites of each cation type are translationally equivalent, the other half appear rotated as well. This is easy to see in Fig. 1 across the vertical face diagonals where like cation types are seen to alternate in pairs. The sites which are translationally equivalent, relative to a cation shown in a corner, are the other corners (obvious), plus the site in the center of the cell (a little harder to see). This arrangement of equivalent sites determines the crystal's Bravais lattice to be body centered tetragonal. For the reasons discussed above, the primitive cell for chalcopyrites will need four times the volume of a zincblende primitive cell, all other parameters being equal. Fig. 2 shows the Wigner-Seitz cell for zincblende embedded in the chalcopyrite cell, along with boxes which represent the non-primitive unit cells from Fig. 1. In reciprocal lattice space the opposite relationship must hold: the zincblende Brillouin zone will be four times larger than that of the chalcopyrite. The Brillouin zones for these two crystal structures are compared in Fig. 3.

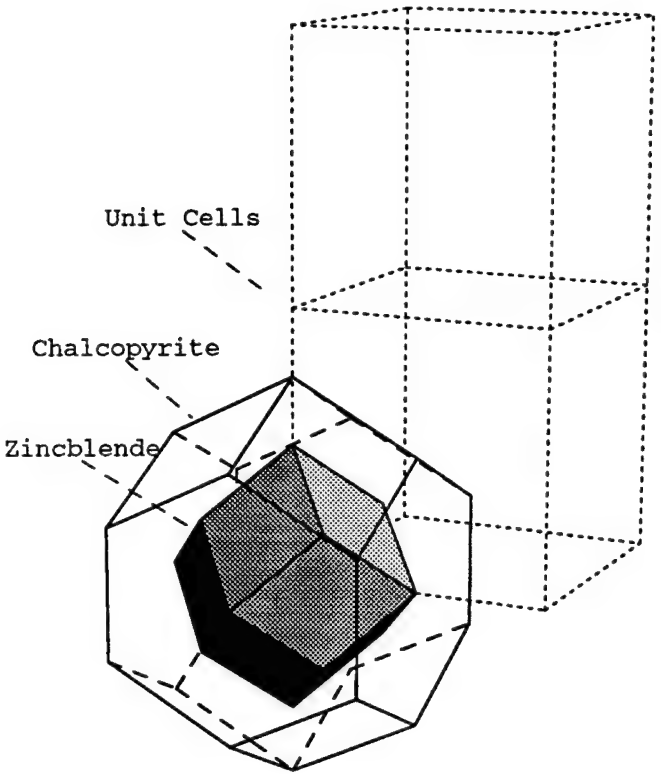

Figure 2. Chalcopyrite and Zincblende Wigner–Seitz Cells Compared

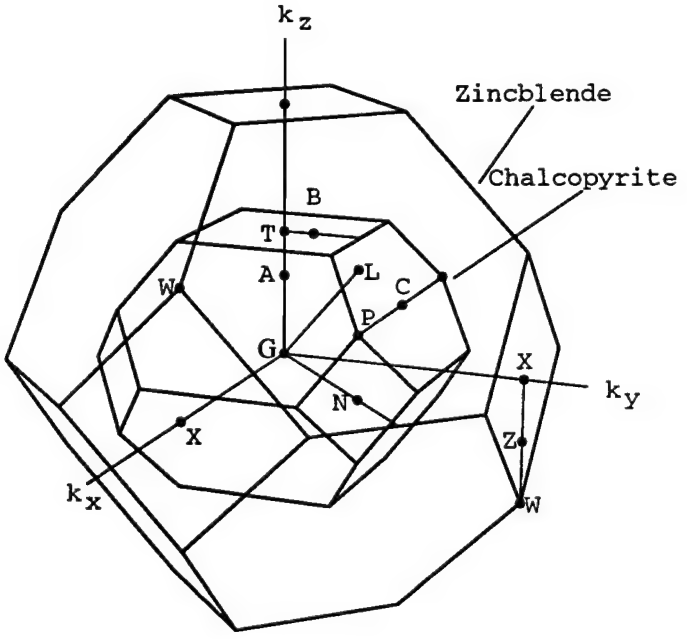

Figure 3. Chalcopyrite and Zincblende Brillouin Zones Compared

2.3. Ternary Chalcopyrites as Analogs of Binary Compounds.

The above discussion of crystal structures highlights the differences between chalcopyrite and zincblende compounds, but in many ways zincblende and chalcopyrite semiconductors are very similar. Fig. 4 illustrates how II-IV-V_2 and I-III-VI_2 compounds are built up from group IV semiconductors substitutionally. Fig. 5 shows a particular case: from a germanium crystal, we form gallium arsenide by replacing half of the germanium atoms with gallium (germanium's immediate neighbor on the left in the periodic table) and the other half with arsenic (germanium's immediate neighbor on the right in the periodic table); taking the next step we now form zinc germanium arsenide by replacing half the gallium atoms with zinc (gallium's immediate neighbor on the left in the periodic table) and the other half with germanium (gallium's immediate neighbor on the right in the periodic table). Thus $ZnGeAs_2$ is called a II-IV-V_2 analog of the III-V compound GaAs. Note that any compound derived this way maintains an average of 4 electrons per atom and all atoms remain bonded to each of their 4 nearest neighbors. While Fig. 5 is a non-physical 2-dimensional projection of the structures for these compounds, all the bonds shown are to the correct type of atom, and the 4 electrons per atom rule is obeyed both globally and locally. Fig. 5 reveals nothing about the actual crystal structures involved, for instance, the smallest closed loops of atoms in Fig. 5 have 4 atoms bonded in a ring, in the actual crystals, such a circuit contains 6 atoms (this is discernible on Fig.1). In two dimensions there really isn't much choice in how to place the atoms and still observe these rules; in three dimensions however, there are several ways to order the individual atoms into a unit cell as small (or even smaller) as that shown in Fig. 1, and only the particular arrangement shown is Fig. 1 is the chalcopyrite structure. Many II-IV-V_2 and I-III-VI_2 compounds happen to crystallize in this chalcopyrite structure.

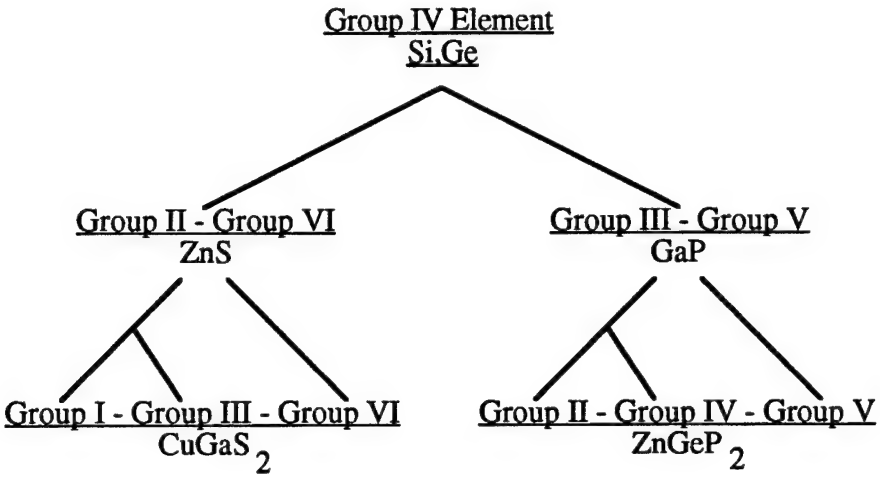

Figure 4. Derivation of II-IV-V_2 and I-III-VI_2 compounds from other diamond like semiconductors[1]

2.4. Implications of Chalcopyrite Lattice Constants.

Many of the properties of particular chalcopyrite semiconductors can be inferred from those of their nearest binary analogs, and evidence suggests that the compression of the unit cell is the dominant source for chalcopyrite physical properties which break cubic symmetry (e.g. birefringence).[1] For this reason a frequent starting point for consideration of a given chalcopyrite is the closest II-VI or III-V binary compound, where the compression of the structure and the chemical differences of the compounds involved can be treated as perturbations. This compression can be quantified as the crystals c/a ratio (the lattice constant 'c' being the height of the unit cell shown in Fig. 1, and 'a' being the length of either side). Since for an uncompressed crystal c/a would be 2, the degree of compressive strain can be taken as 2-c/a, where values then range from zero (or even slightly negative) to about 0.2 for compounds studied to date. While even this maximum value might be considered small (it amounts to 10%), in terms of what can be obtained by physically compressing more commonly used semiconductor crystals, it is immense. Because the ordered semiconductors which will be examined in this study

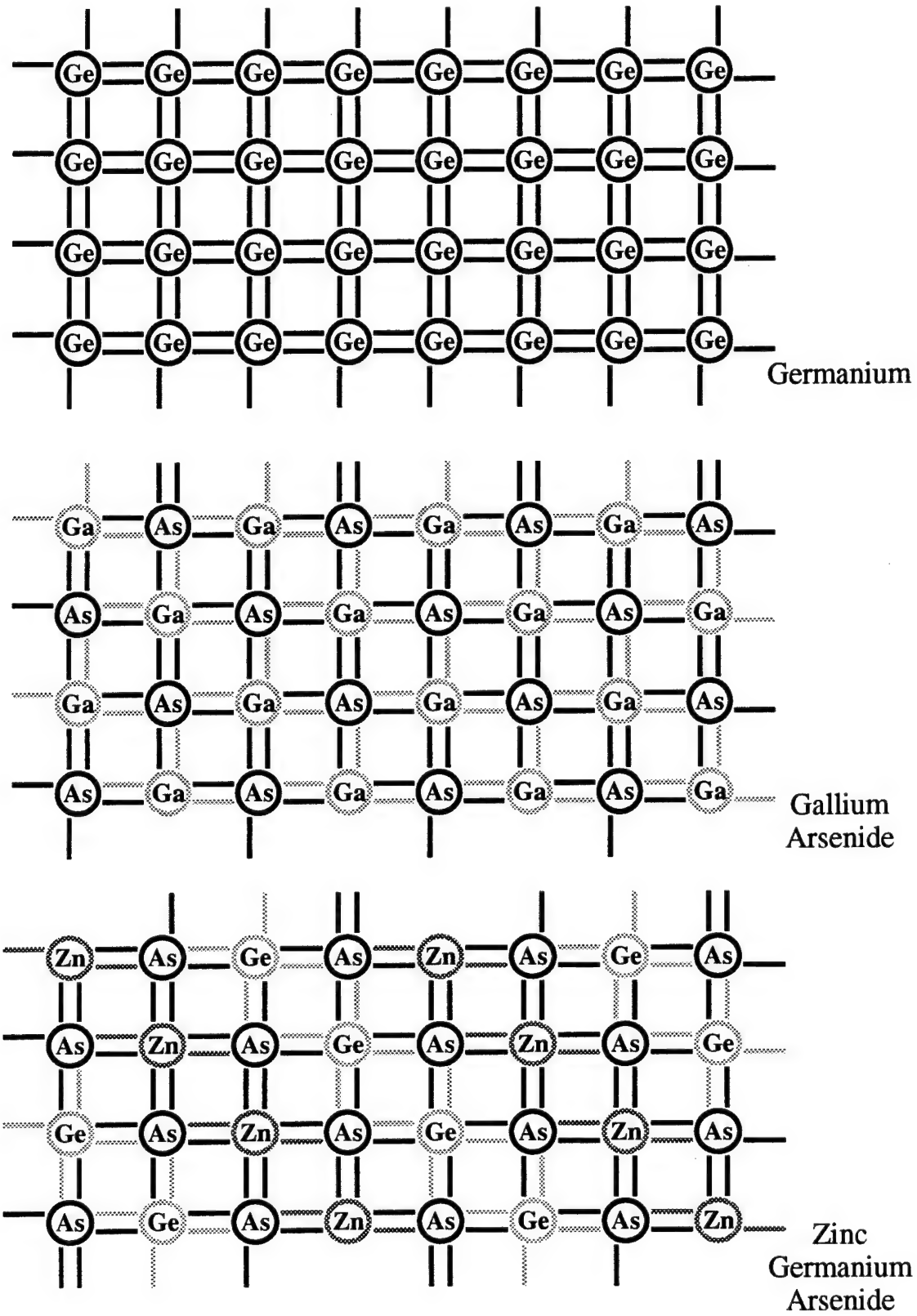

Figure 5. Two-Dimensional Schematic of Atomic Bonding in Diamond-Like Semiconductors

have at least as much in common with their III-V analogs as they do with each other, their characteristics will now be considered individually.

2.5. $CdGeAs_2$.

$CdGeAs_2$ has been studied for more than 30 years because of its interesting electronic properties,[2] its suitability to non-linear optical applications,[3] and it ability to form a glassy phase.[4] Only one report has been made on luminescence from this compound,[5] in this case the material was excited by an electron beam at 80 K. The luminescence was seen to peak at 0.607 eV, near the band gap. The observed narrowing of the spectrum as pumping increased was attributed to stimulated emission. Fig. 6 shows the spectra reported; the linewidth of the narrower peak is instrument limited.

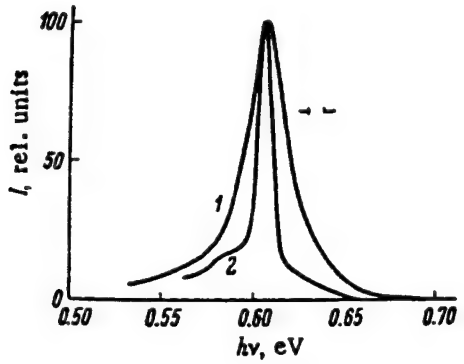

Figure 6. Spontaneous and stimulated radiation spectra of $CdGeAs_2$ crystals at T = 80 K; j (A/cm^2): 1) 0.3; 2) 2.0.

Reports vary as to the bandgap of $CdGeAs_2$. Measurements based upon optical absorption place the bandgap at 0.53 eV at room temperature,[2,6] while electroreflectance suggests the bandgap is 0.57 eV at room temperature.[7] Bandgap information at lower temperatures is rather sketchy; one study places it at 0.67, 0.65, and 0.59 eV at 10, 100, and 270 K respectively based on photoconductivity,[8] while the peak at 0.607 eV at 80 K shown in Fig. 6 has also been taken as the bandgap.[5] Electroreflectance results give 0.65

eV for the bandgap at 77 K.[9] Fig. 7(a) shows the electroreflectance spectrum reported at room temperature and Fig. 7(b) shows the electroreflectance spectrum at 77 K. Theoretical work using the empirical pseudopotential method and including the spin-orbit interaction shows a direct bandgap of 0.55 eV .[10] A more recent theoretical effort using the same technique achieves a value of 0.59 eV for the bandgap.[11] $CdGeAs_2$ does not have an exact binary III-V analog, but its properties could be expected to fall somewhere between those of GaAs and InAs if these materials were placed into the chalcopyrite Brillouin zone. This doesn't help much towards estimating the bandgap since GaAs has a bandgap of 1.42 eV at 300 K and InAs has a bandgap of 0.36 eV at 300 K; this range is wider than the worst disparities in estimates for the bandgap of $CdGeAs_2$. However, it does suggest that $CdGeAs_2$ should have a direct bandgap since GaAs and InAs are both direct.

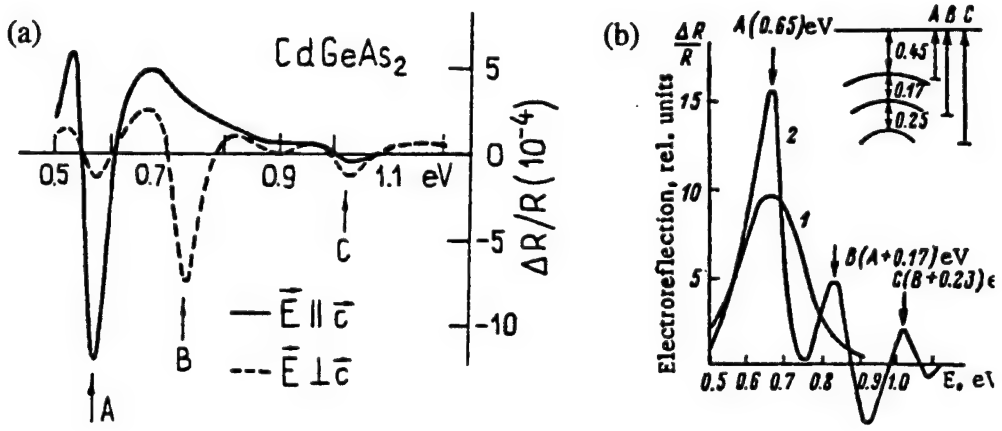

Figure 7. (a) Room Temperature Electroreflectance Spectrum of $CdGeAs_2$ reported by Shileika.[7] (b) 77 K Electroreflectance Spectrum of $CdGeAs_2$ reported by Akimchenko.[9]

While the exact values of the bandgap and other numerical parameters remain in doubt for $CdGeAs_2$, qualitative features of the band structure are more well agreed upon.

Fig. 8 shows a flat band structure model and selection rules for the $CdGeAs_2$ bandgap. The selection rules give the polarization of the electric field of absorbed or emitted photons with respect to the materials c-axis. Symbols shown in parentheses indicate transitions which are only allowed when state mixing due to the spin-orbit interaction is taken into account, and are thus expected to be much weaker. A model exists for predicting the relative strengths of transitions where one transition is allowed and one is only weakly allowed.[1] The intensity ratio is given by:

$$I_{\|}/I_{\perp} = (2+3E/\Delta_{so})^2 \qquad [1]$$

where $I_{\|}$ is the intensity of a transition between the Γ_6 conduction band and one of the Γ_7 valence bands as shown in Fig. 8, with the electric field polarized in the direction of the c axis; $I_{\perp}$ is the intensity of a the same transition with the electric field polarized perpendicularly to the c axis; E is the energy difference between the Γ_7 valence band involved and the Γ_6 valence band; and Δ_{so} is the amount of spin-orbit splitting there would be between the valence bands if there was no crystal field interaction. Δ_{so} can be estimated from the separation between the light and heavy hole bands and the split off band (at $k = 0$) in an analogous III-V compound. The splitting of the valence band can also be computed through this model. The energy differences between the Γ_7 valence bands and the Γ_6 valence band is given by:

$$E_{1,2} = -\frac{1}{2}\left(\Delta_{so} + \Delta_{cf}\right) \pm \left[\left(\Delta_{so} + \Delta_{cf}\right)^2 - \frac{8}{3}\Delta_{so}\Delta_{cf}\right]^{1/2} \qquad [2]$$

Where $E_{1,2}$ is the energy splitting of interest, Δ_{so} is as before and Δ_{cf} is the crystal field splitting - the amount of splitting there would be between the valence bands due to the non-cubic crystal field if the spin orbit interaction were not present. This crystal field splitting is shown in Fig. 8 as such, that is before the spin-orbit interaction is applied; the sign convention is such that direction shown for Δ_{cf} in Fig. 8 is negative. When (one set of) reported values of $\Delta_{so} = 0.33$ eV and $\Delta_{cf} = 0.21$ eV are used one obtains an

anticipated intensity ratio of $I_{\parallel}/I_{\perp} = 12$ for transitions between the highest valence and lowest conduction band in $CdGeAs_2$.

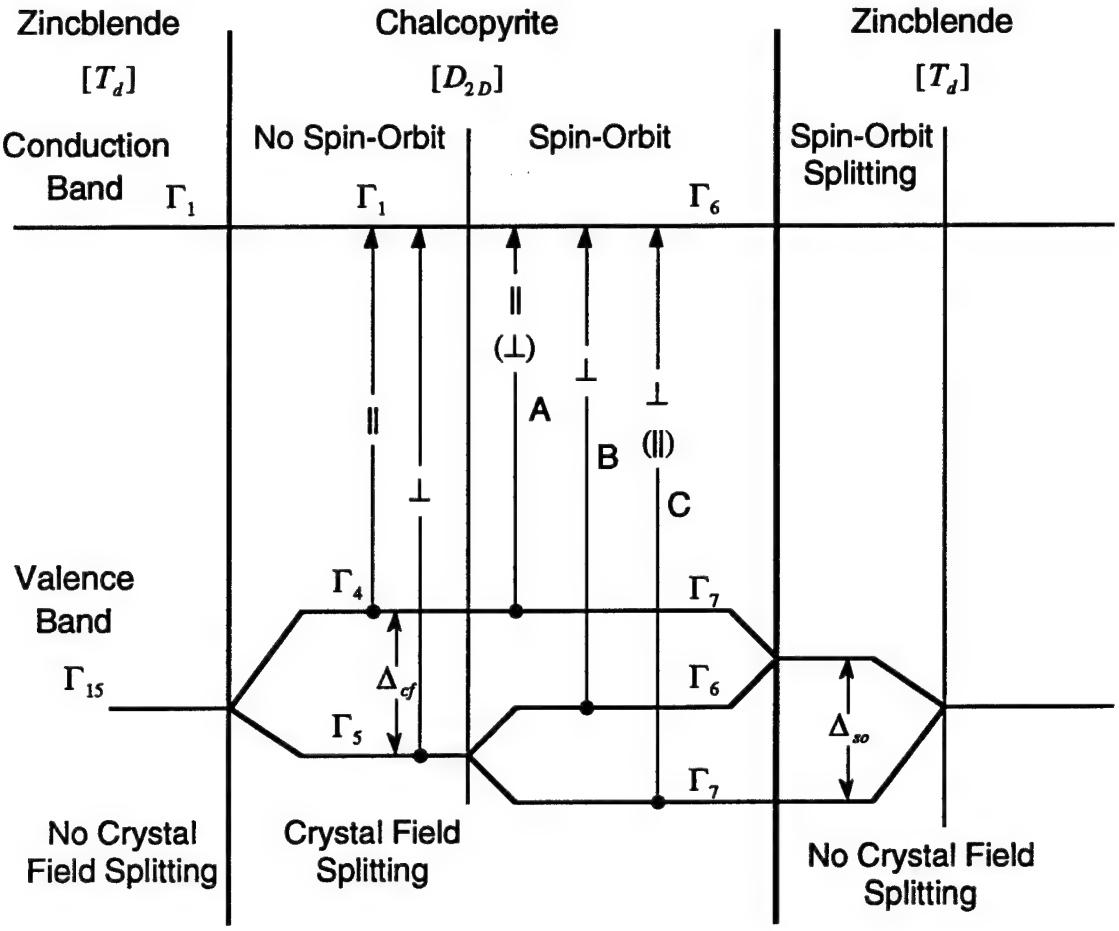

Figure 8. Band Structure and Selection Rules for $CdGeAs_2$[1]

The band structure of $CdGeAs_2$ near $k = 0$ is shown in Fig. 9; the hole masses are shown to be quite anisotropic. The values shown on the right for the separation between the energy levels are disputable as another author[1] uses the same illustration but suggests values of $E_g = 0.57$ eV, $E_1 = 0.16$ eV, and $E_2 = -0.29$ eV. The energy band structure for $CdGeAs_2$ shown in Fig. 10 was calculated by the empirical pseudopotential method and including the spin-orbit interaction.[11]

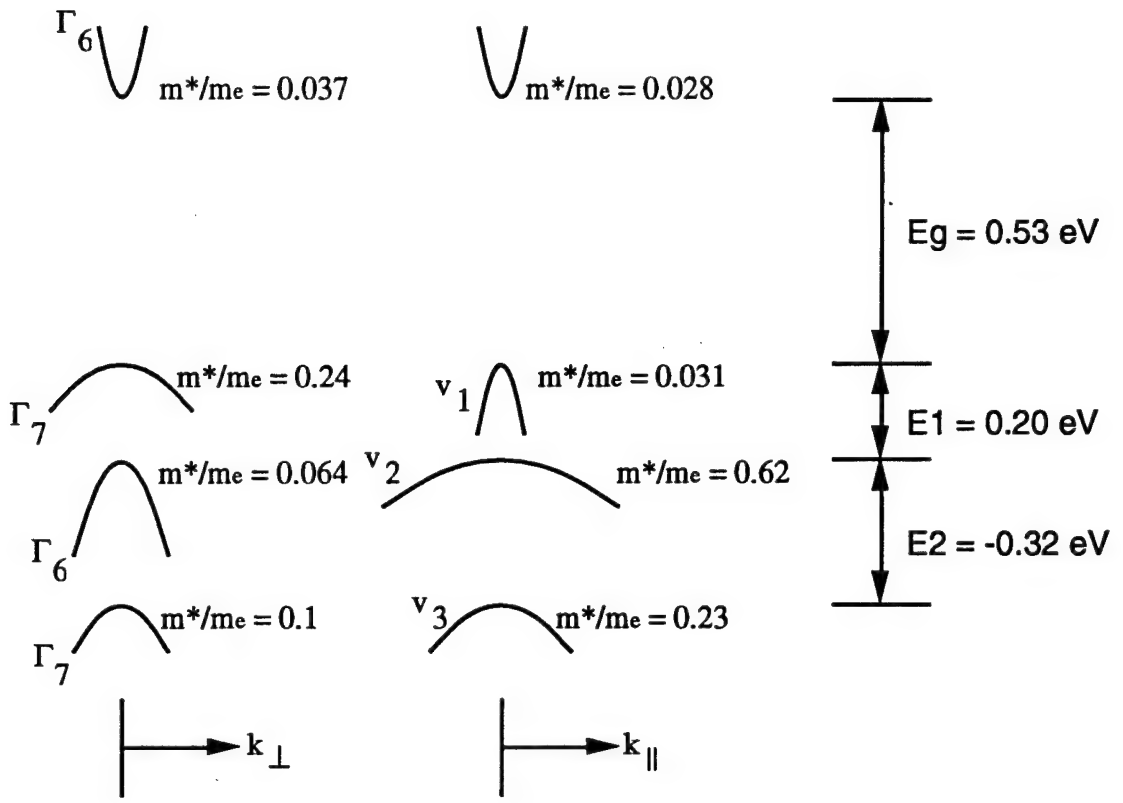

Figure 9. Band Structure of $CdGeAs_2$ near k=0 (after Kildal[12]) with Effective Masses (from Borisenko[13])

Optical absorption measurements have been used to measure the bandgap and other band splittings of $CdGeAs_2$. As stated above, several groups have used the absorption edge to assign a bandgap to $CdGeAs_2$, additionally, an optical absorption peak deeper in the infrared has been attributed to band-to-band absorption between the top two valence bands.[12,13,14] These works place the light hole band (Γ_7) 0.16 - 0.20 eV below the heavy hole band (Γ_6). While band-to-band absorption between the valence bands is one source of below bandgap losses which hampers the use of $CdGeAs_2$ for non-linear optics, removing losses involving defect states directly seems to be the greater challenge.

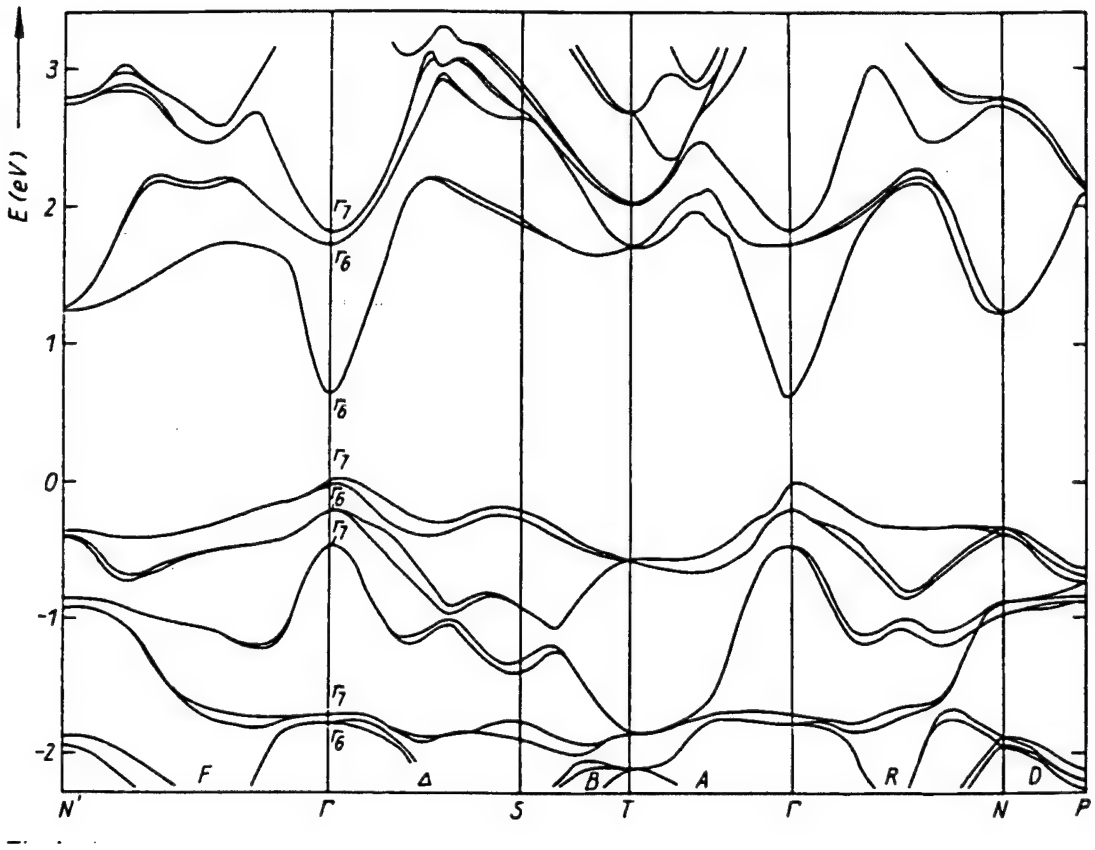

Figure 10. Computed Band Structure of $CdGeAs_2$.[11]

Intersubband absorption can be stopped by ensuring that all valence band states are occupied; compensating the acceptors which make most $CdGeAs_2$ samples p-type helps fill the upper states involved in this absorption. Additionally, cooling the crystal also reduces the number of free holes in the valence bands (by freezing out deep acceptors and lowering the intrinsic hole concentration as well). However, other losses still remain.

Defect states within the bandgap can contribute to the below band-edge absorption via either photoionization of the defects or activation of donor-acceptor pairs (The latter mechanism has been recently proposed as the source of $ZnGeP_2$'s below band edge absorption).[15] A good fit of the temperature dependence of the resistivity and Hall

coefficient has been made to a model for states within the gap of $CdGeAs_2$ consisting of donors, shallow acceptors and deep acceptors with an ionization energy near 0.30 eV.[16] The concentration of deep acceptors was seen to vary over almost four orders of magnitude between growth runs, with little change in impurity concentration. Therefore, the deep acceptors were concluded to be native defects. The below band edge absorption shoulder was seen to extend to energies well below 0.30 eV, and for this reason it was questioned whether the absorption shoulder could be attributed to photoionization of carriers.

Photoconductivity spectra show strong sensitivity to the polarization of the light detected,[17] obeying the selection rules shown in Fig. 8. The polarization response was strong enough that the development of $CdGeAs_2$ photodiodes and photoresistors was recommended for use in analyzing linearly polarized radiation in the 1.4 - 2.3 μm region.

Electron irradiation, followed by annealing, has been shown to be capable of converting p-type $CdGeAs_2$ to n-type $CdGeAs_2$.[18] It is suggested that the irradiation creates additional donors (As vacancies) and acceptors (Ge and Cd vacancies) in the crystal, and that the induced acceptor states anneal out while the induced donors do not, thus making the crystal more n-type. Thermal annealing has also been seen to improve the homogeneity of $CdGeAs_2$'s electrical properties.[6]

Recent results achieved using electron paramagnetic resonance (EPR) have shown $CdGeAs_2$ to have an EPR active defect with an unpaired spin shared by four neighboring As ions. They suggest that the defect is either a vacancy or an antisite associated with the cation sublattice.[19] Additionally, there was some evidence of more than one EPR active defect.

2.6. $ZnGeP_2$

$ZnGeP_2$ is a close analog of GaP; in fact, a reasonable approximation to the band structure of $ZnGeP_2$ can be made by folding the band structure of GaP into the

chalcopyrite Brillouin zone. This is how the bandstructure of $ZnGeP_2$ was first approximated. This folding causes the indirect bandgap seen in GaP to appear as a direct bandgap in $ZnGeP_2$. This bandgap is called pseudo-direct because transitions at this critical point are only allowed to the extent that Zn and Ge behave differently within the lattice.[1] Because the effects of Zn and Ge on the lattice are not greatly different, the pseudo-direct transition should be weak. If the cations (Zn and Ge in this case) were indistinguishable to an electron traveling through the crystal, then the folding of the bands would be in principle only. The bandgap would appear to be indirect to any optical or electrical experiments which might be carried out. The band structure of $ZnGeP_2$ as computed by the empirical pseudopotential method is shown in Fig. 11, this figure ignores the effects of spin-orbit interactions.[20] If this effect is taken into account, the bands will be separated into sub-bands.[21] This splitting is shown in Fig. 12.

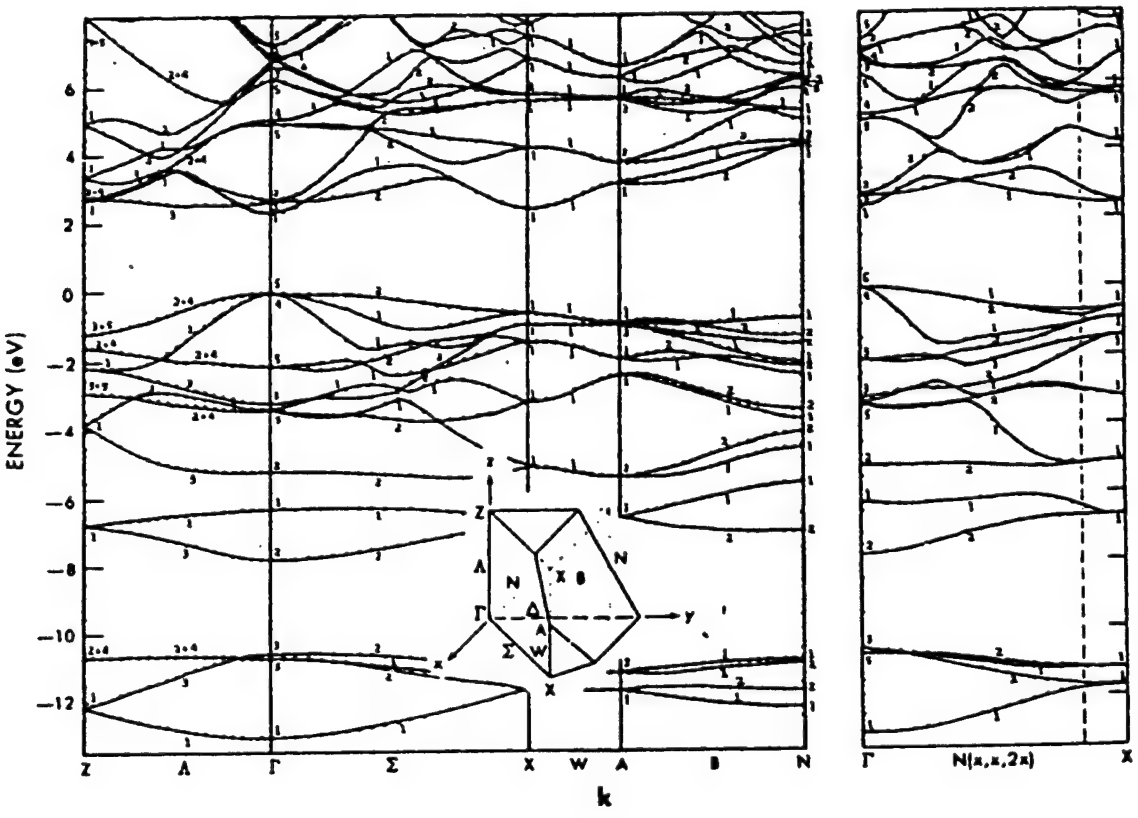

Figure 11. Band structure of $ZnGeP_2$[20]

Much previous work has been done with $ZnGeP_2$. It has been studied by PL, CL, and x-ray luminescence methods. A mechanism explaining the acceptor level luminescence, and the material's extrinsic near IR absorption has been described. Improvements in IR transparency have been achieved through electron beam processing and annealing. The PL of $ZnGeP_2$ has been shown to be strongly polarized as well.

One large study of PL from $ZnGeP_2$ examined crystals grown by differing techniques with a variety of deviations from stoichiometry and the presence of various dopants. The undoped samples showed peaks, near 1.6 or 1.3 eV, whose magnitudes varied with the stoichiometry of the sample, and the growth technique used.[22]

Another study, using CL, shows three weak features, near 1.6, 1.8 and 1.9 eV, spanning a large, broad impurity luminescence peak. This study also describes a weaker, feature rich, luminescence peak spreading from 2 to 2.4 eV, and attributed to band-to-band transitions. X-ray luminescence data showed comparable results, but with no structure seen on the weaker luminescence peak.[23]

$ZnGeP_2$'s extrinsic absorption in the near-IR has be attributed to a photoionization of a deep acceptor level, designated AL1 (acceptor level 1), with an ionization energy near 0.6 eV. AL1 is attributed to a native defect, possibly a zinc or germanium vacancy, or zinc on a germanium site. Long term annealing of the material near half of the melting point, and bombardment with 2 MeV electrons, have both been shown to decrease this IR absorption. It is proposed that the electron bombardment creates phosphorus vacancies which act as donors and thereby compensate the acceptor level.[24]

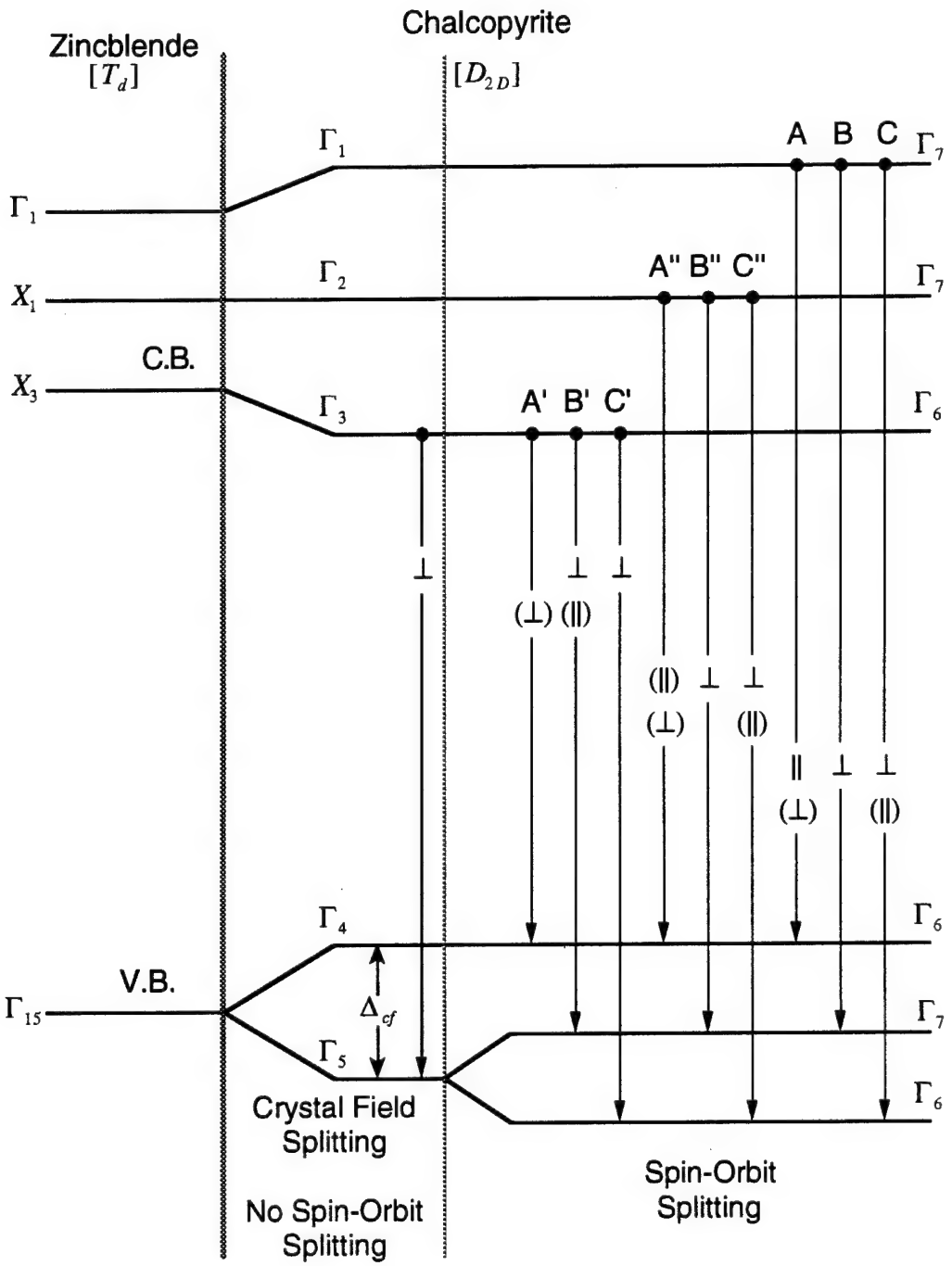

Figure 12. Bands of $ZnGeP_2$, including the spin-orbit interaction.; The $\parallel$ and $\perp$ symbols refer to the polarization of the electric field with respect to the c-axis for emitted photons. Transitions in parentheses are expected to be weaker since they are only allowed when the spin-orbit interaction is included. Primed and double primed transitions are pseudo-direct, unprimed transitions are direct[21]

The PL spectrum has been shown to vary considerably with polarization for $CuGaS_2$, a material structurally comparable to $ZnGeP_2$.[25] Recently the CL spectrum of $ZnGeP_2$ has been shown to be strongly polarization dependent.[26] The PL of $ZnGeP_2$ has been shown to be polarized with the emitted photons' electric fields predominantly aligned perpendicularly to the materials c-axis.[27] In this case the PL was also seen to vary considerably with the excitation mechanism, with the peak shifting to higher energies as the excitation laser moved from the visible to the ultraviolet, then the luminescence peak moved to higher energies still when cathodoluminescence was collected. This luminescence was attributed to transitions from the several conduction bands to states associated with the acceptor level AL1.

More recent results attribute both PL and below band edge absorption to transitions between donor acceptor pairs.[15] This work suggests a model where the predominant acceptor state is shallower than suggested earlier, and a phosphorus vacancy contributes deep donors, as illustrated in Fig. 13.

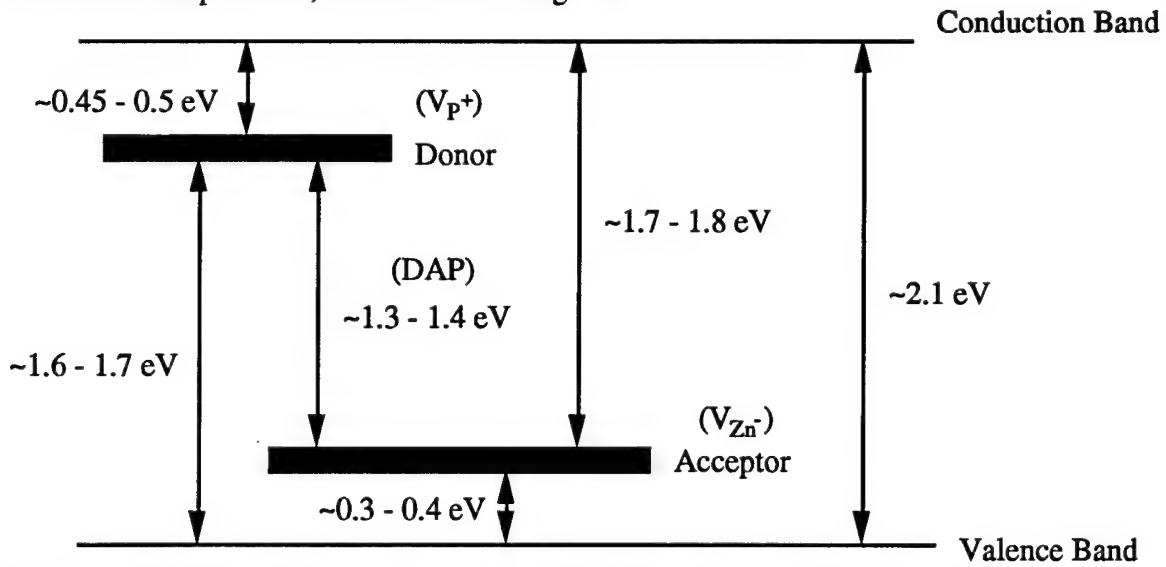

Figure 13. $ZnGeP_2$ Energy Level Diagram Showing donor-acceptor pair (DAP) Absorption.

Chapter III. Photoluminescence.

Photoluminescence spectroscopy consists of analyzing the light which is re-emitted from a sample of material when it is excited by another light source. Section 3.1 discusses the mechanisms by which light is re-emitted from an excited sample, section 3.2 discusses the equipment used for these experiments, and section 3.3 details the results achieved.

3.1. PL Theory.

There are many mechanisms by which semiconductor material can emit light. In short, when an electron moves from a high to a low energy state a photon might be emitted. Fig. 14 illustrates several of these possibilities. The wavelength of the emitted photon can be used to identify the mechanism whereby it was created, making luminescence spectroscopy an excellent diagnostic tool for probing impurity energy levels and the band structure of materials. The transitions outlined in Fig. 14 are grouped into three classes: (1) interband transitions, (2) transitions involving impurities or defects and (3) hot carrier intraband transitions. The first category is further broken down into (a) near-band-edge band-to-band transition and (b) hot carrier band-to-band transition. The second category consists of (a) conduction band to acceptor level, (b) donor level to valence band, (c) donor to acceptor level and (d) deep level transitions. Any of these illustrated transitions could result in the emission of a photon; whether this is likely or not depends upon both the transition mechanism and the material. Many other considerations serve to further complicate this already complex topic. An electron and a hole can orbit each other about their common center of mass; this hydrogen-atom-like system is called an exciton. Excitons can only exist for a meaningful length of time at very low temperatures. Since the electron and the hole attract each other, an exciton has

less potential energy than a free pair of charge carriers. Thus when an exciton recombines, any photon which is emitted has slightly less energy than the bandgap. Since this photon doesn't have quite enough energy to re-excite an electron from the valence band into the conduction band, it has a much better chance to escape from the crystal than photons created by transitions at or above the bandgap. Luminescence caused by transitions from the conduction band to an acceptor level is often called impurity luminescence; it is still be called impurity luminescence even when the acceptor level is created by a crystal defect, rather than an actual impurity.

Moving from the flat-band model of Fig. 14 to the reduced zone representation of the band structure, makes another distinction apparent. Semiconductors may be either direct gap, or indirect gap materials, depending upon whether or not the maximum of the valence band and the minimum of the conduction band occur for the same value of k. Fig. 15 compares these two possibilities, and contrasts their light emitting mechanisms. Because electrons will tend to equilibrate to the lowest energy state available, the top of the valence band will collect holes, as electrons move down into available lower energy states. For the same reason, the bottom of the conduction band will collect electrons. In a material with a direct gap, the k values of these distributions overlap, and photons can be emitted as carriers recombine directly. In a material with an indirect gap however, the story is not so simple. Since a transition from the conduction band to the valence band involving only the emission of a photon will not conserve crystal momentum it is highly unlikely. In order for an electron to make a transition from the conduction to the valence band, both a phonon and a photon may be emitted, thus allowing both momentum and energy to be conserved.

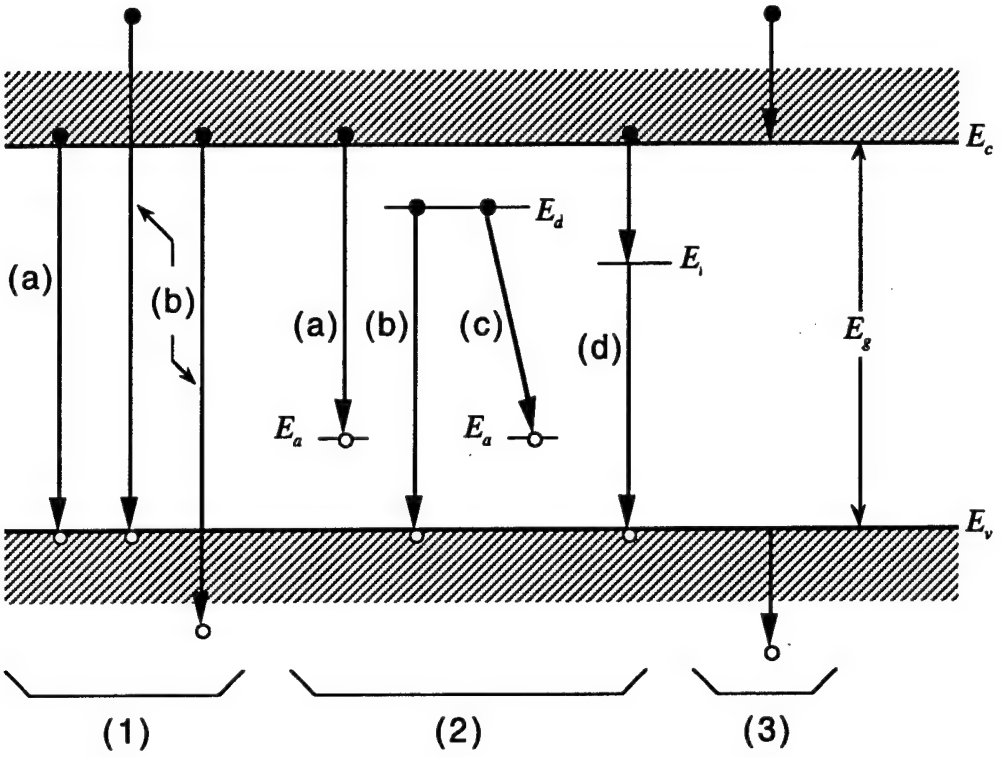

Figure 14. Basic transitions in a semiconductor.; E_g is the bandgap, E_v marks the top of the valence band, E_c marks the bottom of the conduction band, E_a is an acceptor level, E_d is a donor level, and E_t is a trap level[28]

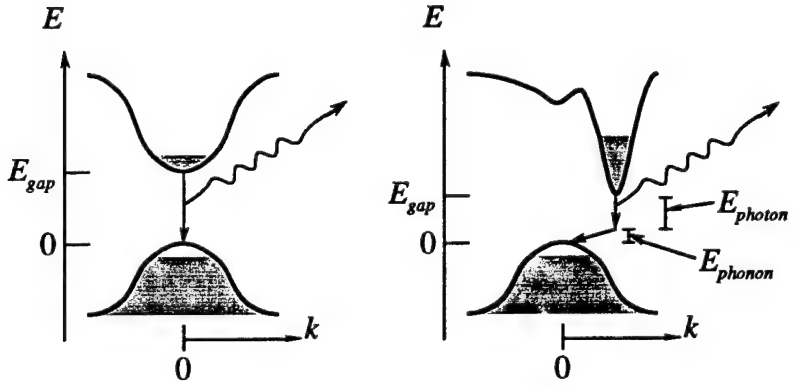

Figure 15. Direct vs Indirect Bandgap Transitions; (a) Electron and hole recombine and a photon is emitted. (b) Electron and hole recombine, emitting a photon and a phonon[29]

3.2. PL Equipment

The experimental setup consisted of three main subsystems: the liquid helium dewar and sample holder, the excitation laser and associated hardware, and the luminescence collection and detection equipment. Each of these subsystems and their operating procedures are described below. Fig. 16 schematically represents the experimental layout.

3.2.1. Liquid Helium Dewar and Sample Holder

The dewar used for this study was a Janis Research Company Supervaritemp 10-liter liquid helium optical cryostat. This dewar has four chambers: the liquid helium reservoir; the sample chamber; the vacuum jacket; and the liquid nitrogen jacket. The vacuum jacket must be evacuated to less than one microtorr of pressure before the dewar can be cooled down. When this vacuum is achieved, the sample chamber and the liquid helium reservoir can be evacuated by starting the mechanical pump plumbed to these chambers and opening the valves connecting the pump to these chambers. The valve to the vacuum jacket is then closed, and the turbopump is allowed to spin-down. Liquid nitrogen can then be poured into the liquid nitrogen reservoir. After one hour, the turbopump and its mechanical backing pump can be shut off; after several hours, the liquid helium reservoir will have cooled to near liquid nitrogen temperature and can be filled with liquid helium. The valve between the liquid helium reservoir and the pump is shut and the reservoir is back-filled with helium gas. Liquid helium is transferred from a storage dewar to the reservoir using a vacuum insulated transfer line.

The sample chamber is cooled by opening a small needle valve which allows liquid helium from the reservoir to enter the sample chamber. While helium is being transferred, the needle valve is occasionally opened a quarter of a turn. If the pump, which is still pulling on the sample chamber, begins to gurgle, liquid helium has begun collecting in the reservoir. If the pump gurgles after several turns of the valve, then

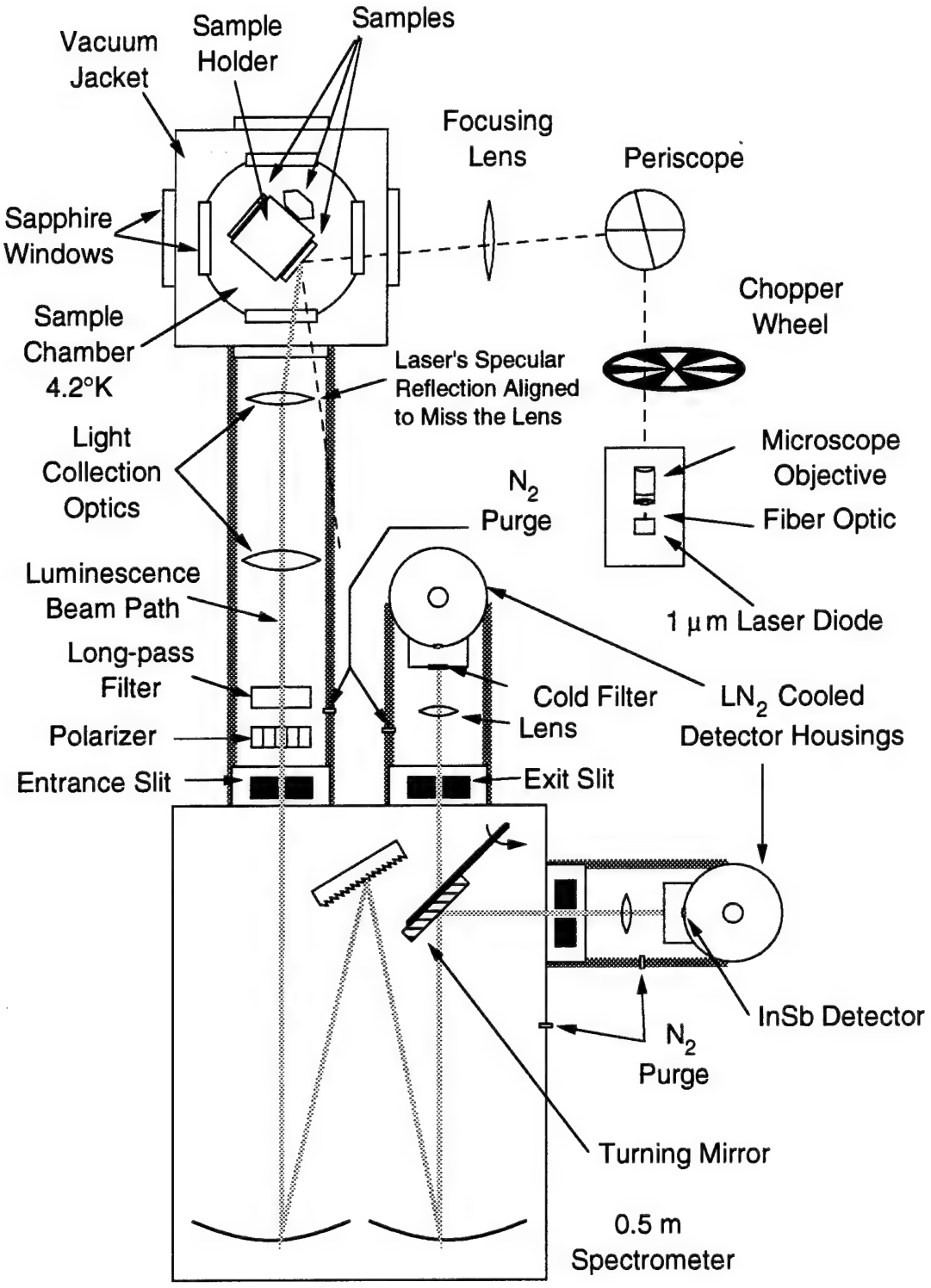

Figure 16. Mid-IR PL Experimental Layout

helium gas is in the reservoir, and the transfer rate may need to be increased by pressurizing the storage dewar to a few psi. If the pump doesn't gurgle at all, or if the needle valve cannot be turned, then a ice-block (probably water-ice but frozen nitrogen is also a risk) has plugged the needle valve, and the entire system must be brought to room temperature before cool-down can be re-attempted. While helium transfer is progressing, an electrical helium level gauge monitors the liquid helium level in the reservoir. When the helium transfer is complete, the sample chamber can be cooled down. The valve between the pump and the sample chamber is closed, and the needle valve is opened about a full turn. An electronic gauge monitors the temperature at the bottom of the sample chamber or on the sample holder. When the temperature on the sample holder stops falling and begins to rise, the pressure in the sample chamber has reached atmospheric and prevents more liquid helium from entering through the needle valve. A small relief valve is then opened at the top of the sample chamber to allow gravity to feed liquid helium into the sample chamber. The needle valve is adjusted to maintain a small pool of liquid helium below window level on the dewar. Some variations of this procedure are also used occasionally, however, allowing the pressure in the vacuum jacket to exceed the pressure in the helium reservoir or allowing water into the dewar where it can freeze could destroy the dewar, so great care must be exercised. To achieve temperatures lower than 4.2 K, the boiling point of liquid helium at atmospheric pressure, a vacuum may be drawn on the sample chamber while liquid helium is continuously being added. While this substantially increases the liquid helium consumption rate, temperatures as low as 1.6 K are attainable.

Normally, samples are mounted on the sample holder, and placed within the dewar before cool-down commences, but samples may be exchanged at any time. The sample holder is withdrawn from the chamber, the chamber is capped, and a slight overpressure of helium is used to keep the sample chamber clean. When the sample holder is warm and dry, it and the samples to be mounted are cleaned with methanol and

cotton swabs. The sample is then mounted with a spot of rubber cement, using tweezers. For thin samples, it is important to use as little cement as needed, in order to prevent strain in the sample when cooled down, due to differing coefficients of thermal expansion between the copper sample holder and the sample itself. Strain could change the luminescent properties of the sample; these risks are slight in this study since the samples are thick and the luminescence spectra are broad. Before re-inserting the sample holder, it was rapped to verify that the samples were not likely to fall off in the dewar. The sample holder is then placed back within the dewar. The sample holder rod extends up through a gasket to the top of the dewar, thus the samples can be rotated, raised and lowered within the sample chamber to help align the laser and luminescence beams.

3.2.2. Excitation Laser

For most PL experiments carried out thus far for this study a fiber coupled GaInAs diode laser operating at 1μm was used. The laser energy exits the fiber with a fairly large divergence, so a microscope objective is used to collimate the light into a narrow beam (~5 mm). The diode laser is capable of output powers in excess of 1 W, but the power supply actually used (HP Model E3611A DC Power Supply) limits it to just over 500 mW. The laser beam was chopped at 100 Hz by a chopper-wheel.. The laser beam then traversed a periscope and a focusing lens before finally hitting the target. The beam diameter is estimated to be as small as 1 mm on the target with careful focusing. The sample facet, which was originally set to near 45 degrees between both the laser beam and the light collection direction was then turned back towards the laser beam until it could be seen that the laser's specular reflection was missing the first collection lens. Surprisingly, this step of turning the sample more obliquely to the spectrometer entrance actually increased the luminescence signal. With further consideration, this does make sense, since this increases the laser intensity on the target, and while the total luminescence collected by the lenses is decreased, the brightness is not necessarily

decreased, and only a portion of the sample's image passes through the entrance slit anyway. Additionally, an Ion Laser Technology model 5400 air-cooled argon-ion laser, which is tunable to a number of visible wavelengths, was also used occasionally. The argon-ion laser was normally operated at 488.0 or 514.5 nm. Although the laser's internal power meter reported output powers as high as 40 mW, direct measurement with a power-meter indicated only 30 mW maximum.

3.2.3. Collection and Detection of Luminescence

The luminescence collection and detection equipment consisted of a pair of lenses, various long-pass filters, polarizers for the infrared, a Spex model 500M 1/2 meter spectrometer with a 4 inch square, 300 lines/mm grating blazed for 3 μm, a Cincinnati Electronics or EG&G Judson InSb photovoltaic detector, a Stanford Research Systems SR850 DSP lock-in amplifier, and an AT&T 386 Star PC running Spex software to log data and drive the Spex controller electronics. Additional support equipment included a power supply to power the detector preamplifiers.

A pair of lenses were used to collect the photoluminescence signal. To align these lenses, a high intensity lamp was shined upon the sample from the side of the sample chamber, the lenses were then positioned to form an image of the sample on a sheet of paper taped over the spectrometer's input port. When the lamp was removed, and the laser turned on, the diffuse reflection of the laser from the sample would also fall upon the paper. When the laser spot was seen to be on the right part of the sample, and the image of the sample fell upon the input port of the spectrometer, the coarse alignment of the system was considered complete. The spectrometer slit was then opened and the spectrometer was set to a wavelength where a strong photoluminescence signal was expected, typically 2.1 μm or 3.2 μm, for $CdGeAs_2$ samples. The lock-in amplifier was then turned on and set to a 300 mS time constant; its sensitivity scale was increased until the signal was found. Finally the collecting lenses were repositioned with their

micrometer adjustable stages until the signal was maximized. To optimize the signal in the vertical direction one or both collection lenses can be moved up and down to peak the signal, however, when the signal is nearly optimized it is easier to move the laser spot on the sample slightly up or down instead, since the lens mounts have no fine height adjustment mechanism. This approach is clearly not acceptable when the sample is being checked for site to site homogeneity. If the detectors had been moved since they were last aligned, their signals needed to be maximized too. Because the detectors have only a few square millimeters of active area, and also because the mounting hardware does not allow them to be placed right at the exit slits, a lens is used to reimage the exit slit onto the detector element. At this point a long pass filter or a polarizer could be placed at the entrance slit to the spectrometer and the system was ready to take data.

To begin a data run, the lock-in amplifier was first set to an appropriate time constant, the computer was then programmed with the starting and finishing wavelengths, the wavelength step size, the integration time per stop, and the exit port to be used on the spectrometer. Then the computer was instructed to take data. When the computer directs the monochromator to advance to the next wavelength, the monochromator accomplishes this quite quickly, and the computer begins averaging over the signal it is receiving from the lock-in. If the lock-in time constant is long compared to how fast the monochromator moves between points (normally this is the case) the output from the lock-in is still strongly influenced by the strength of the luminescence at the previous wavelength, and the measured spectrum will be smeared to longer wavelengths (assuming the monochromator is stepping to higher wavelengths with time). If the lock-in time constant is close to, or shorter than, the computer's integration time, this smearing will amount to a fraction of the wavelength step size. This gives a guide for setting the computer integration time: too short and the data from one wavelength is smeared into many succeeding data points, too long and time is wasted at each step making the run overly long. For example, many data runs have been taken covering 2.0-2.5 μm. Typically, the

time constants would both be set to 1 second, and the step size would be 1 nm. The spectrometer's slit width also sets a limit on the resolution of the spectrum; in most cases both slits were set to 2 mm. The spectrometer's dispersion is approximately 6.6 nm/mm, and again it is best to have all these limits nearly the same; except that the spectrometer slit width leads to symmetric smearing of peaks, which does not move their positions, so the spectrometer's resolution can reasonably set to the coarsest of the various limits on resolution present. This is clearly the case outlined here, since the slit width will widen peaks to at least 13 nm (FWHM), while the data collection equipment would smear peaks a further 1-2 nm towards higher energy.

3.3. PL on $CdGeAs_2$.

Photoluminescence spectra have been obtained from 10 different samples of this material, tabulated as Table 1. An example spectrum is show as Fig. 17. On every sample a broad, weak PL peak is seen near 0.38 eV, and most samples also have a brighter peak near 0.57 eV, for low temperature PL. The temperature, laser power, and polarization of the PL are all worth investigating.

3.3.1. PL Peak Near 0.38 eV.

The broad weak PL band near 0.38 eV seen by low temperature (~4 K) PL on every sample is evident on Fig. 17. One possibility is that this luminescence is due to transitions from donor states near the conduction band to acceptor states near the middle of the bandgap (DAP). It is also reasonable to guess that this luminescence is due to transitions from the states in the conduction band to deep acceptors; this process would be called free-to-bound (FB). While both of these processes might be involved, it is difficult to separate these effects since the peak is so weak that fairly long run times are required to exhibit it clearly, and raising the temperature or decreasing the laser power quickly buries this signal in noise.

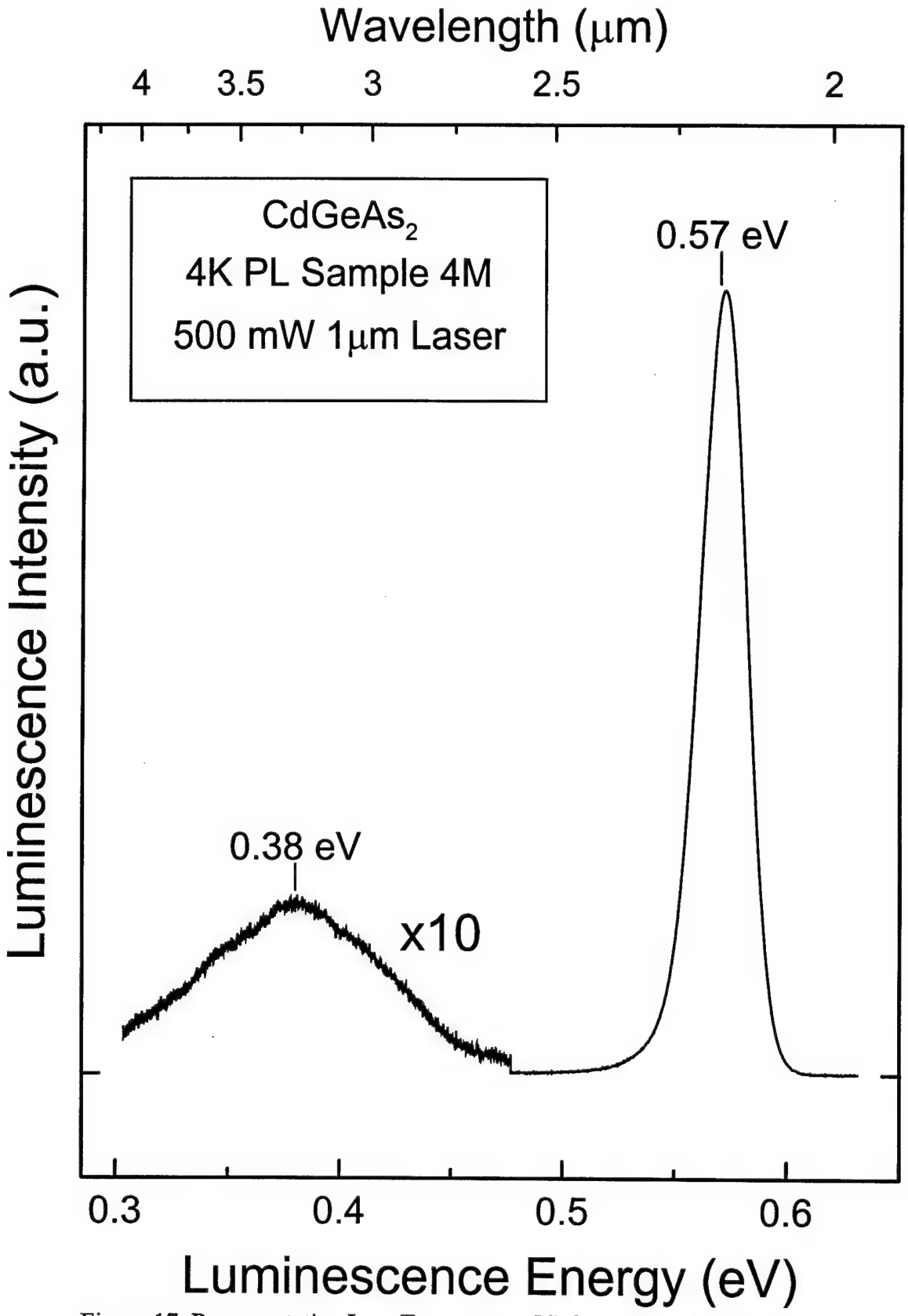

Figure 17. Representative Low Temperature PL Spectrum of $CdGeAs_2$.

Table 1. $CdGeAs_2$ Samples Studied		
Ident	Grown by	Orientation
5110	EKSMA	Unknown
5106	EKSMA	Unknown
5031	Ioffe	C-axis normal to facet <001>
2G	Sanders	C-axis in plane of facet <100>
4M	Sanders	C-axis in plane of facet <100>
4N	Sanders	C-axis in plane of facet <100>
4P	Sanders	C-axis in plane of facet <100>
4Q	Sanders	C-axis in plane of facet <110>
4O	Sanders	C-axis in plane of facet <100>
11A	Sanders	C-axis normal to facet <001>

3.3.2. PL Peak Near 0.57 eV.

Most samples have also demonstrated a much brighter and somewhat narrower emission band near 0.57 eV. This is the case on Fig 17. The variation of this higher energy peak with changes in temperature and laser excitation power suggest that this peak is comprised of DAP transitions between shallow acceptors and donors, as well as band-to-band transitions, with DAP dominating at low temperature and band-to-band predominating at high temperatures.

3.3.2.1. Temperature Dependence of High Energy Peak.

Fig. 18 shows a sequence of data collection runs at increasingly higher temperatures; these curves have been offset in position vertically and scaled to have

equal peak amplitudes. The peak intensity measured on each curve is marked, and these peaks are connected by an additional curve. The greater noisiness seen at higher temperatures is due to the greater multiplier required for scaling a weaker signal; the absolute noise is not detectably affected by the sample temperature. This is evidenced on Fig. 19 which again shows the measured spectra, but this time each is on the same scale. The accuracy with which the true PL peak position can be taken as the peak measured signal is clearly degraded where the signal appears noisy. For instance, this is quite noticeable on the 225 K curve, where it appears that the bulk of the PL energy falls at energies below the marked peak, and the marked peak itself seems to be due to the biggest noise blip across a broad maximum. Additionally, the amount of variation in peak position observed for slight temperature differences also demonstrates the amount of uncertainty in peak positioning. The use of more sophisticated peak positioning techniques will be discussed in a subsequent section. While the effective vertical scale is not linear in temperature, the trend is clear - first the peak position decreases in energy with increasing temperature, then it increases, peaks, and begins decreasing again. The variation of the PL peak energy with temperature is shown again in Fig. 20. At low temperatures, the PL signal can be interpreted as due to DAP transitions, thus the peak position is given by E_g-E_A-E_D, where E_g is the bandgap, E_A is the acceptor ionization energy and E_D is the donor ionization energy. As the temperature first starts to increase, this remains true, and the peak position moves as the bandgap moves (changes in E_A and E_D being insignificant on this scale). At high temperatures the luminescence mechanism is dominated by band-to-band recombination and the peak position is given essentially by E_g. Connecting these two regimes is a transition region, from approximately 50-100 K, where the luminescence mechanism is switching between these two processes. Thus the position of the PL peak moves anomalously in this transition region, towards higher energies as the temperature increases. Additional evidence that the luminescence mechanism switches comes from the variation of the luminescence intensity with

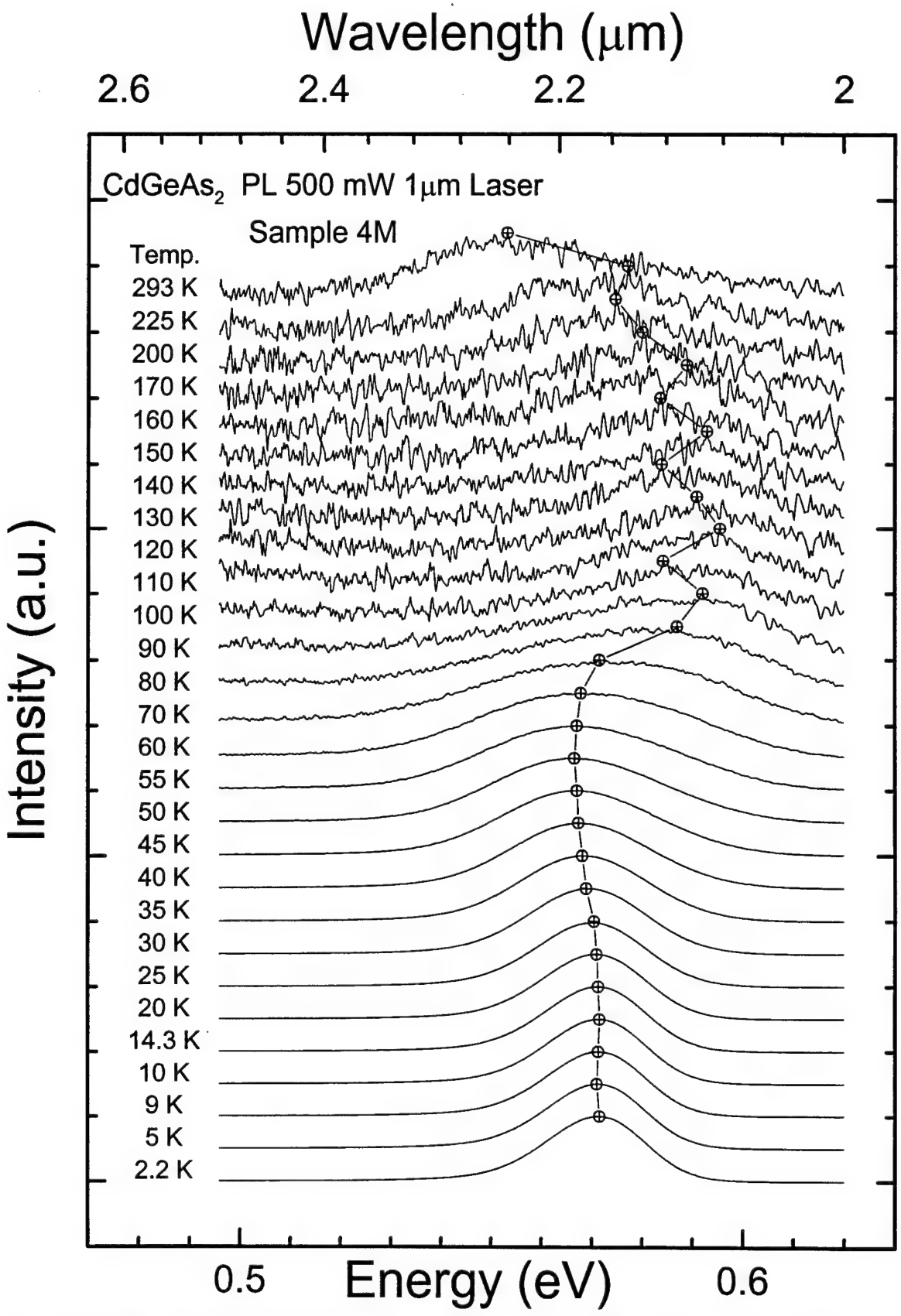

Figure 18. Temperature Dependance of PL Spectrum of $CdGeAs_2$, Scaled and Offset.

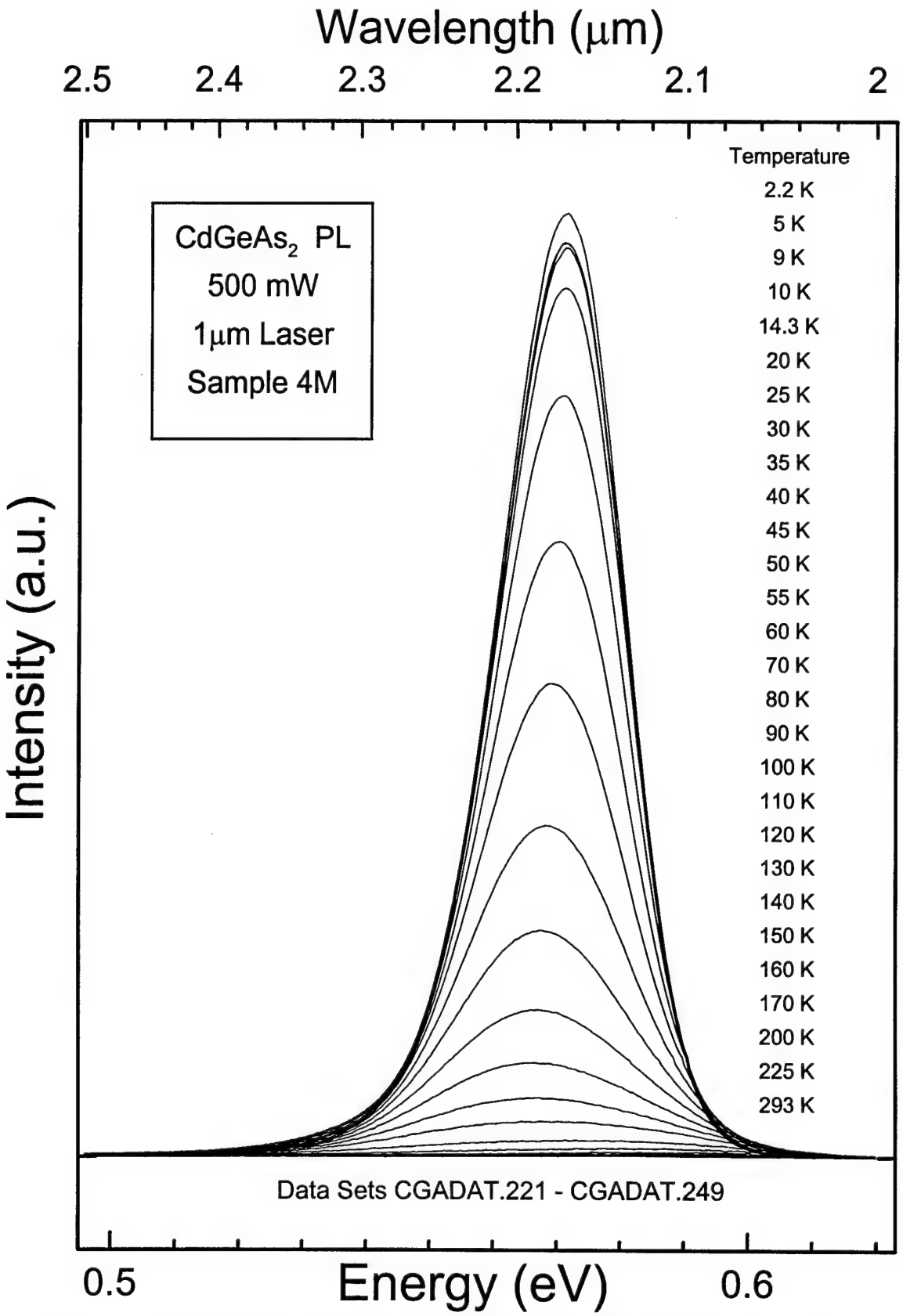

Figure 19. Temperature Dependance of PL Spectrum for $CdGeAs_2$, Raw Data.

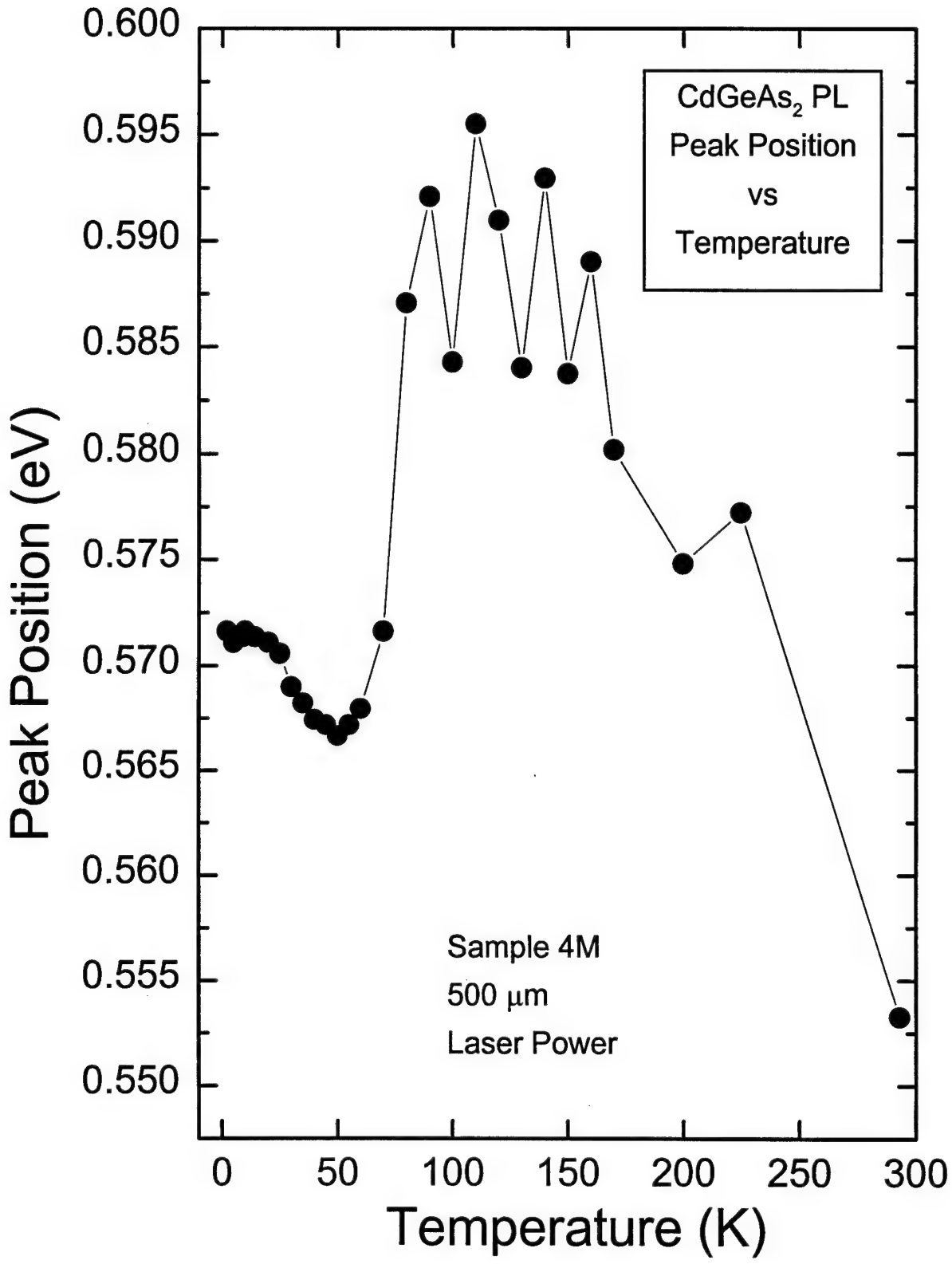

Figure 20. Motion of PL Peak Position with Temperature for $CdGeAs_2$.

temperature. Fig. 21 shows the area under the curves seen in Fig. 19 on a logarithmic scale (Actually, the log of the sum of all data points on each curve). At the extreme low end of the temperature scale (less than 10 K), the luminescence does not appear to be greatly affected by temperature; here the carriers are all frozen out, and there is not enough thermal energy to disturb any of the donor-acceptor pairs before they can decay radiatively. At low, but not extremely low, temperatures (15-100 K) the integrated intensity is effectively a straight line, indicating an exponential decay of the signal with increasing temperature, here at least one member of the donor-acceptor pairs is being ionized into its respective band before it can decay radiatively via a DAP transition. At high temperatures (above 150 K), the curve appears to be following a shallower, but rising line, indicating exponential growth of the luminescence, the high temperatures at which this process persists suggests that band-to-band recombination is being observed. Again there is a transition region across which the dominant radiative recombination process appears to be changing. In this case the transition occurs between about 100 and 150 K. The energies involved roughly confirm this story; from Fig. 20 it is apparent that the dopant ionization energies total about 25 meV, which is about kT at room temperature, so if the shallow acceptors and donors have about equal ionization energies, then kT at 150 K equals this energy. The transition region from 50-100 K seen on Fig. 20 then might seem to be too low in temperature to correspond with this explanation, but the difference in density of states between the defect levels allows ionization to proceed at temperatures lower than kT. It is also possible that free-to-bound type transitions are also occurring in the spectra observed, further complicating the situation; these transitions would be intermediate in energy between the DAP and band-to-band type recombinations proposed, and thus quite difficult to separate out.

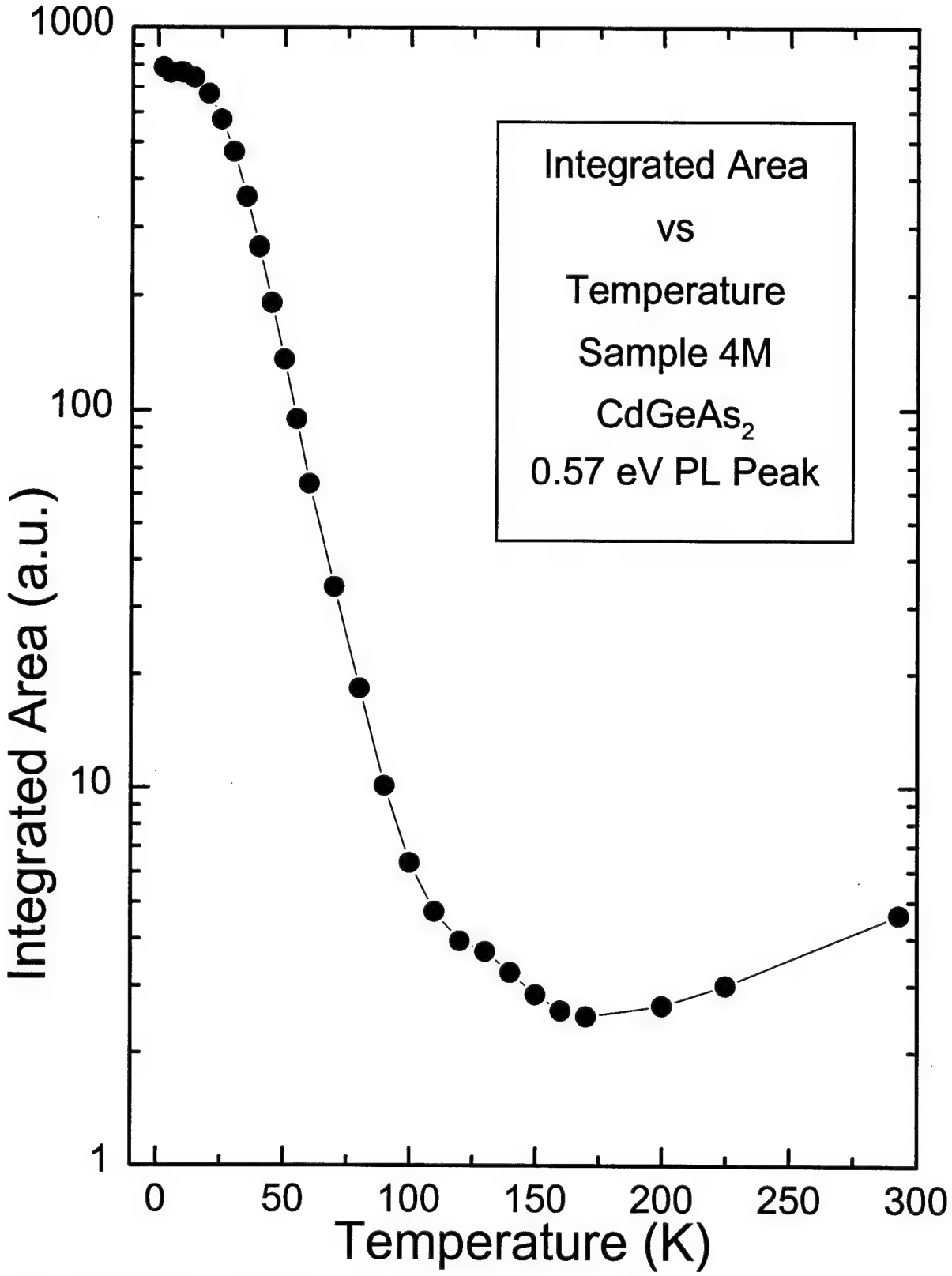

Figure 21. Change in PL Intensity with Temperature for $CdGeAs_2$, Logarithmic Scale.

3.3.2.2. Room Temperature PL of High Energy Peak.

The PL peak near 0.57 eV persists at least to room temperature, in fact this peak is two to three times as bright at room temperature as it is at 170 K where the integrated peak area passes through a minimum. Fig. 22 shows the spectrum of this peak, taken with longer time constants than the spectra in Figs. 18 & 19 to improve the signal-to-noise ratio. Since the sample is p-type (presumably all the samples are p-type, this particular sample was measured to be so at room temperature), the high energy tail of this peak should correspond to the distribution of electrons in the conduction band, that is should fall off like exp(-E/kT). This is indeed seen to be the case for kT near room temperature, and this lends additional support to the proposition that band-to-band recombination is the dominant source for the room temperature PL. Fig 23 shows this comparison on a logarithmic scale, where the tails on each side of the peak can seen to be fairly straight lines. At room temperature, the high energy tail of the PL peak is seen to decay more slowly than the low energy side; this situation is reversed for low temperature PL where the high energy tail decays more quickly. It can be seen on Fig. 19 and Fig. 23 that this is because the high energy tail lengthens with temperature, while if the low energy tail is growing with temperature, it isn't doing it as quickly.

3.3.2.3. Laser Power Dependence of High Energy Peak.

The behavior of the high energy PL peak was also examined as a function of laser power. As the laser power is decreased the luminescence can be seen to decrease and shift to lower energies. A series of spectra taken at successively lower laser powers is given as Fig. 24. The area under each of these curves as a function of laser power is shown in Fig. 25 on logarithmic scales (Again, the integrated values are actually computed by summing all the data points on each curve, effecting the integration over wavelength, since the spectrometer generates data per wavelength interval). The slope of the curve is close to 1, which is consistent with DAP or band-to-band recombination.

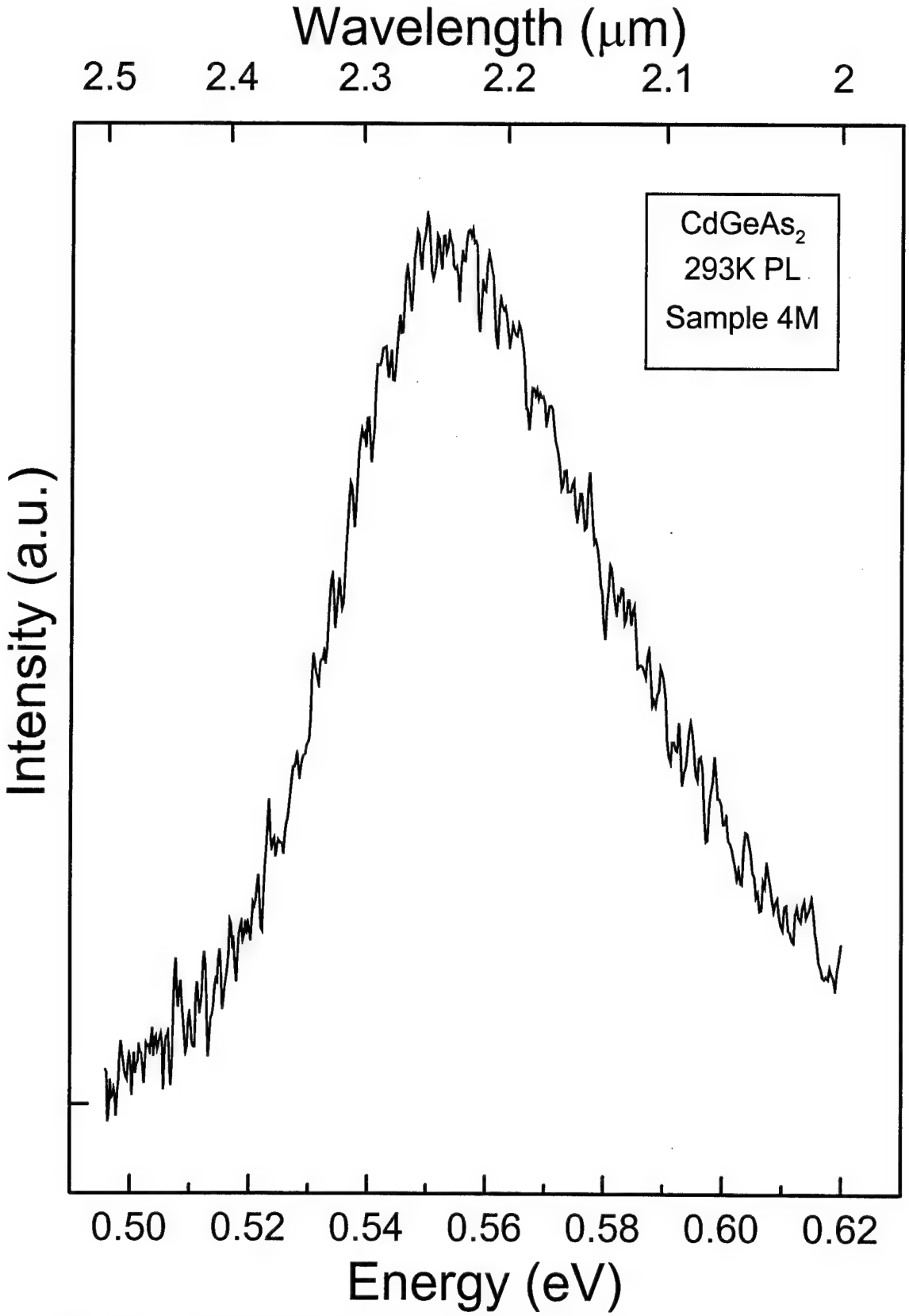

Figure 22. Room Temperature PL Spectrum for $CdGeAs_2$.

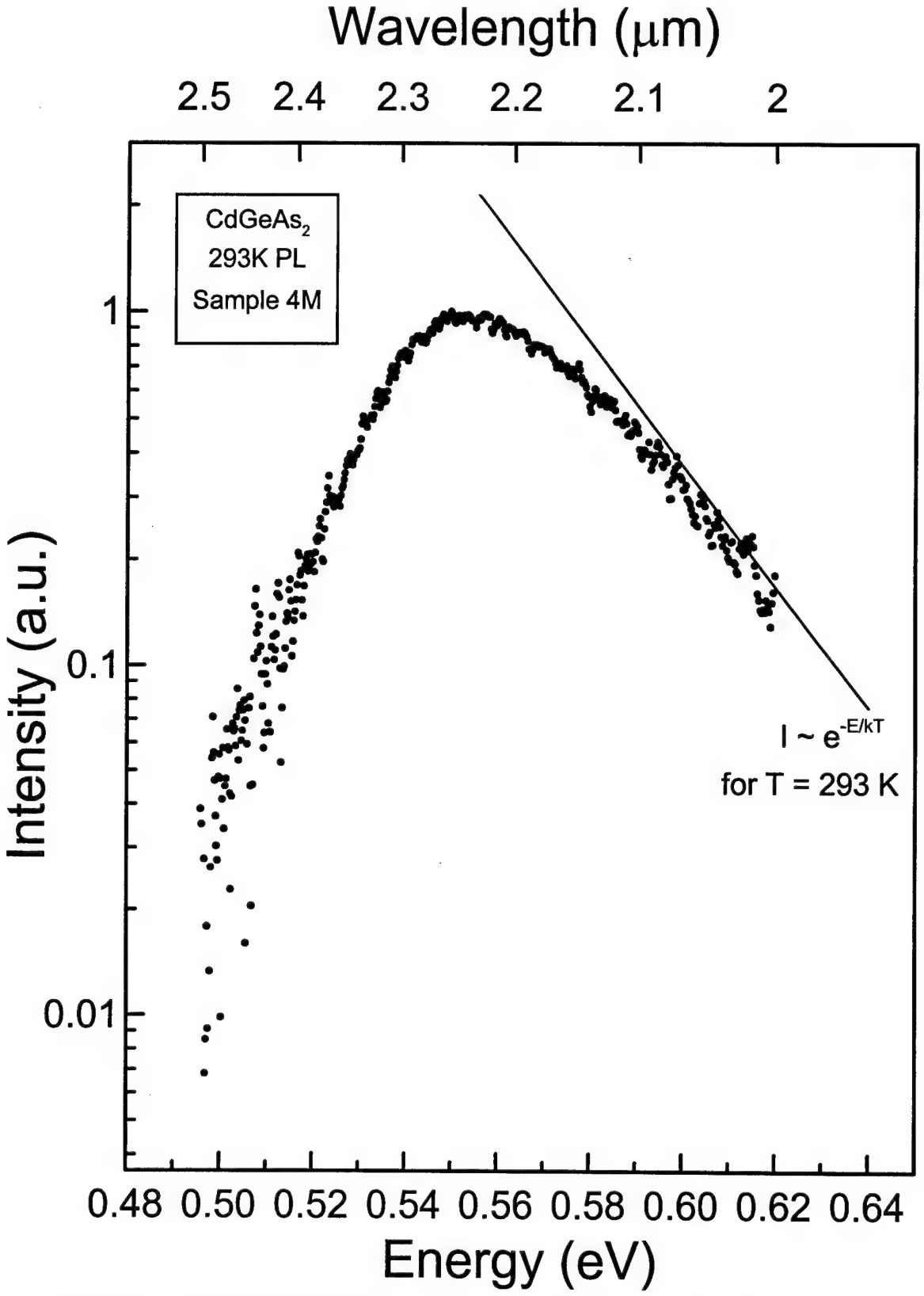

Figure 23. Room temperature PL spectrum for $CdGeAs_2$ on a logarithmic scale

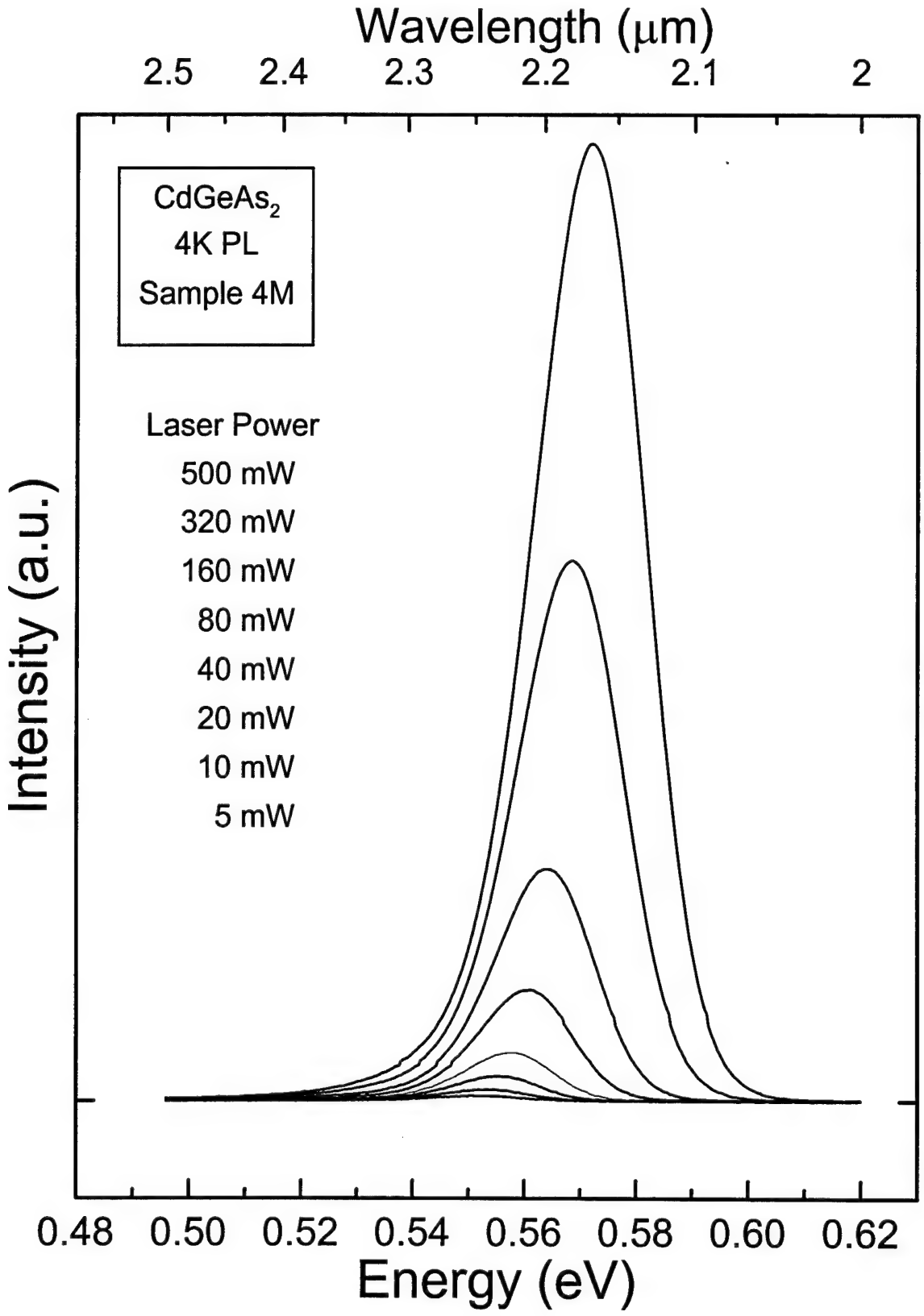

Figure 24. Laser Power Dependance of Low Temperature PL Spectrum for $CdGeAs_2$.

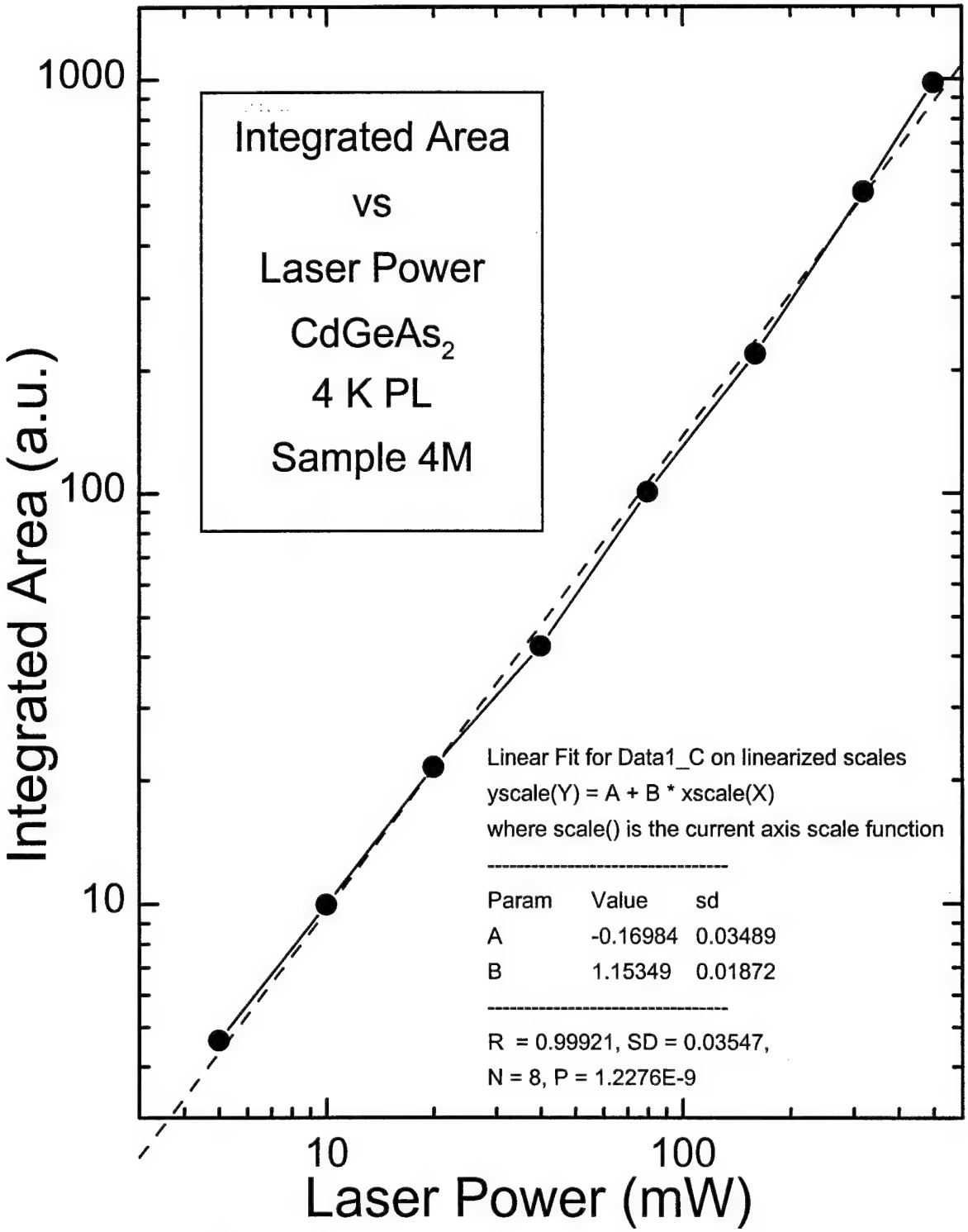

Figure 25. Change in PL intensity with Laser Power for $CdGeAs_2$, Log-Log Axes.

The motion of the peak with laser power is plotted on Fig. 26. A straight line fit to this data is not completely satisfactory, but the peak shift appears to be in the neighborhood of 10 meV/Decade. This peak motion suggests DAP recombination. Motion of the PL peak to higher energies with increasing excitation can also be expected once the pumping becomes hard enough to put the quasi-fermi levels within a few kT of the conduction and valence bands. It seems unlikely that the pumping is this hard. If this was the source of the whole peak shift, then the total peak shift of nearly 25 meV would imply the quasi-fermi levels were many kT's into the bands at high excitation (since this data was taken at 4 K), and amplified spontaneous emission should be evident. There appears to be good correlation between the kinks seen in the peak position vs laser power and integrated intensity vs laser power curves; it is difficult to tell if this represents changes in the luminescence mechanism, or only inaccuracy in the assignment of laser power to specific current levels.

3.3.2.4. Polarization Dependence of the High Energy Peak.

The high energy peak was seen to be quite strongly polarized. Fig. 27 shows the motion of this peak as a linear polarizer is rotated through 180 degrees. There is no noticeable change in the shape or position of the peak as the polarizer is rotated; only the overall intensity seems to be affected. The sample used in this case (4Q) did not luminesce as brightly as that used above and this data was taken on a coarser scale. This accounts for the additional noise seen on these spectra. The area under each one of these spectra is plotted as a function of the polarizer angle on Fig 28. The discussion above showed that the expected polarization for band-to-band transitions in this material should be about 12 to 1, but only about half of that is seen here. If only the narrowest band gap is involved however, the intensity of the transition alone is expected to be affected by polarization, as is seen here (i.e. there is no change in the shape of the spectrum or motion of the peak with polarization).

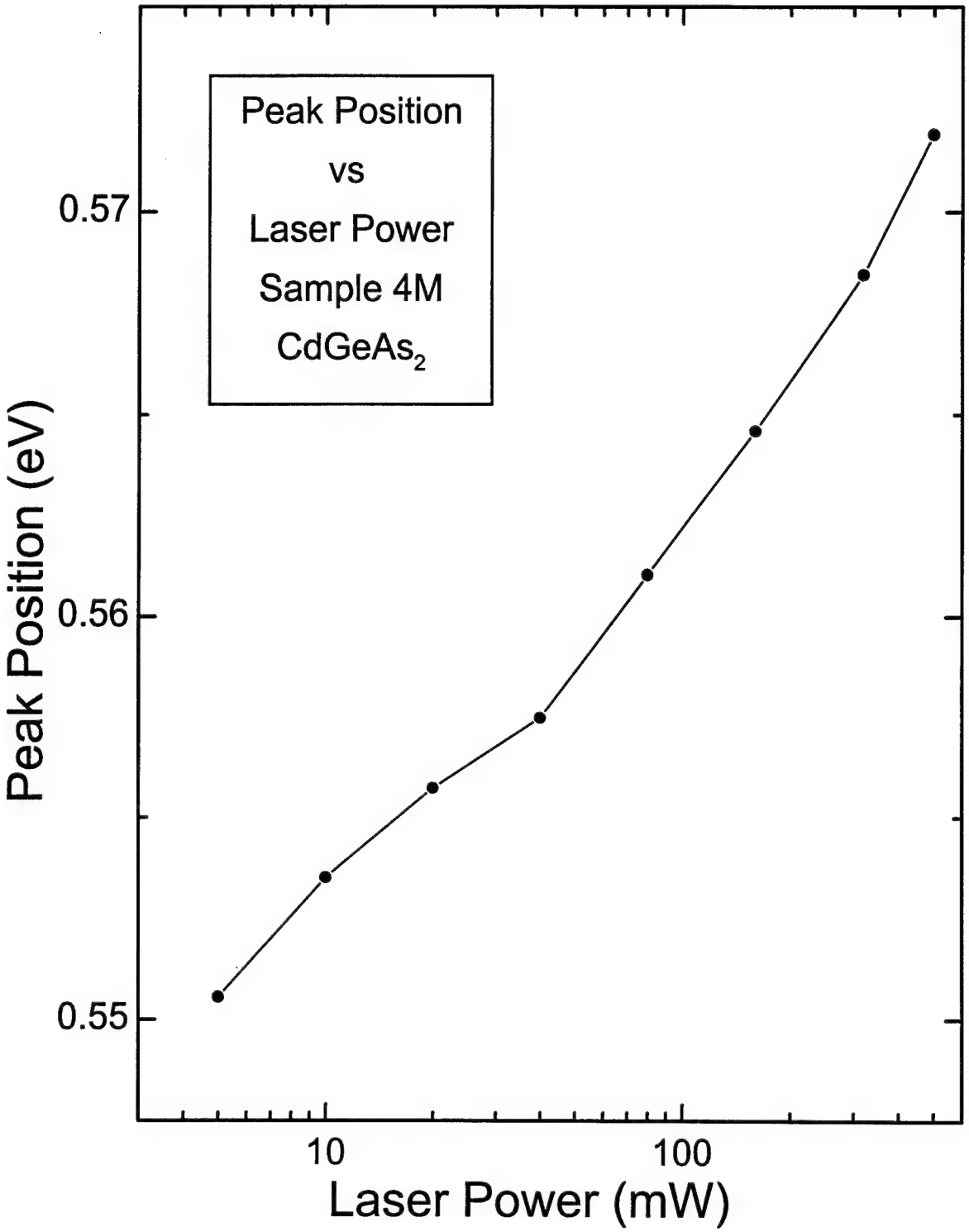

Figure 26. Motion of PL Peak Position with Laser Power for $CdGeAs_2$, Semilog Scale.

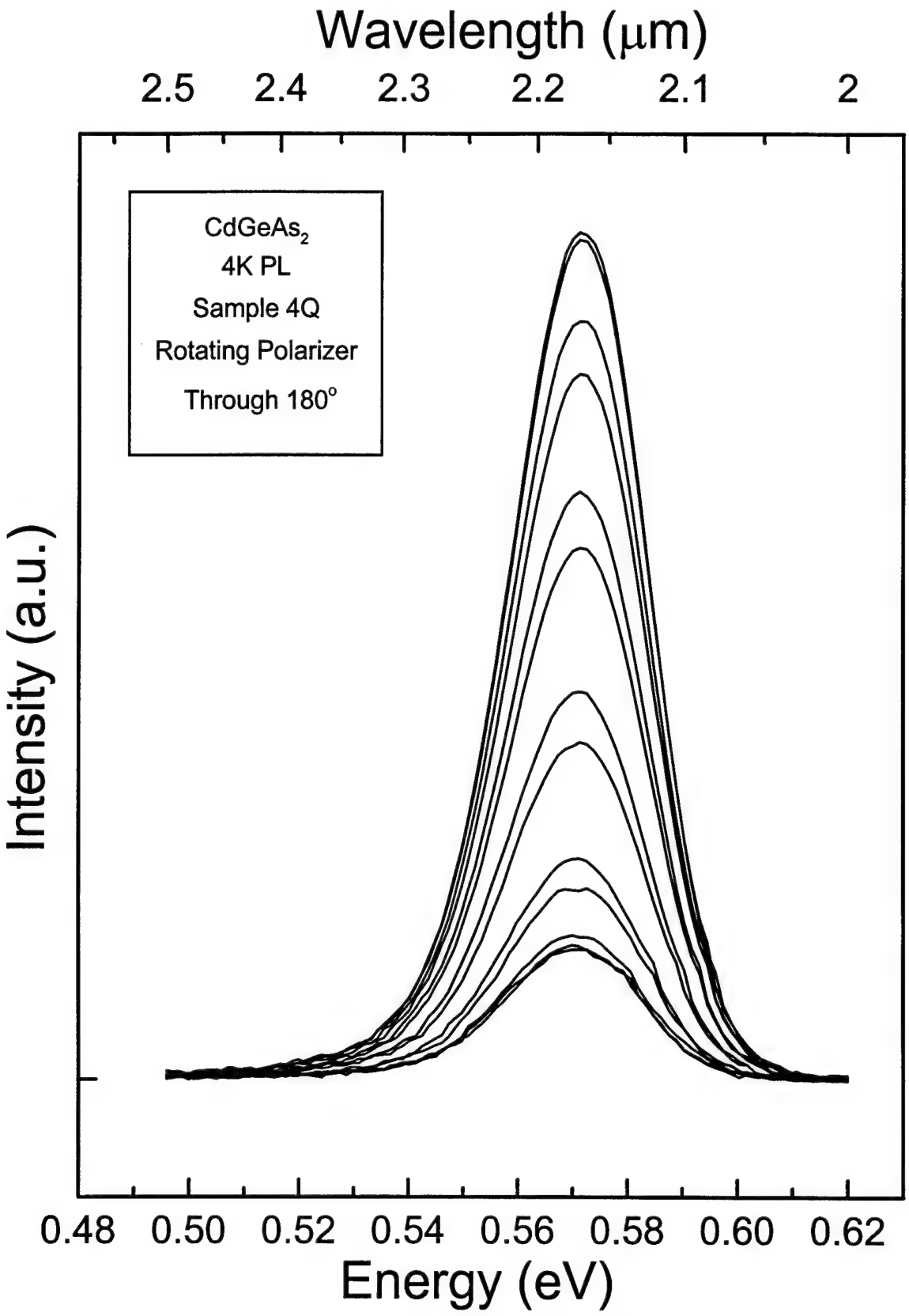

Figure 27. Changes in PL Spectra with Polarizer Angle for $CdGeAs_2$.

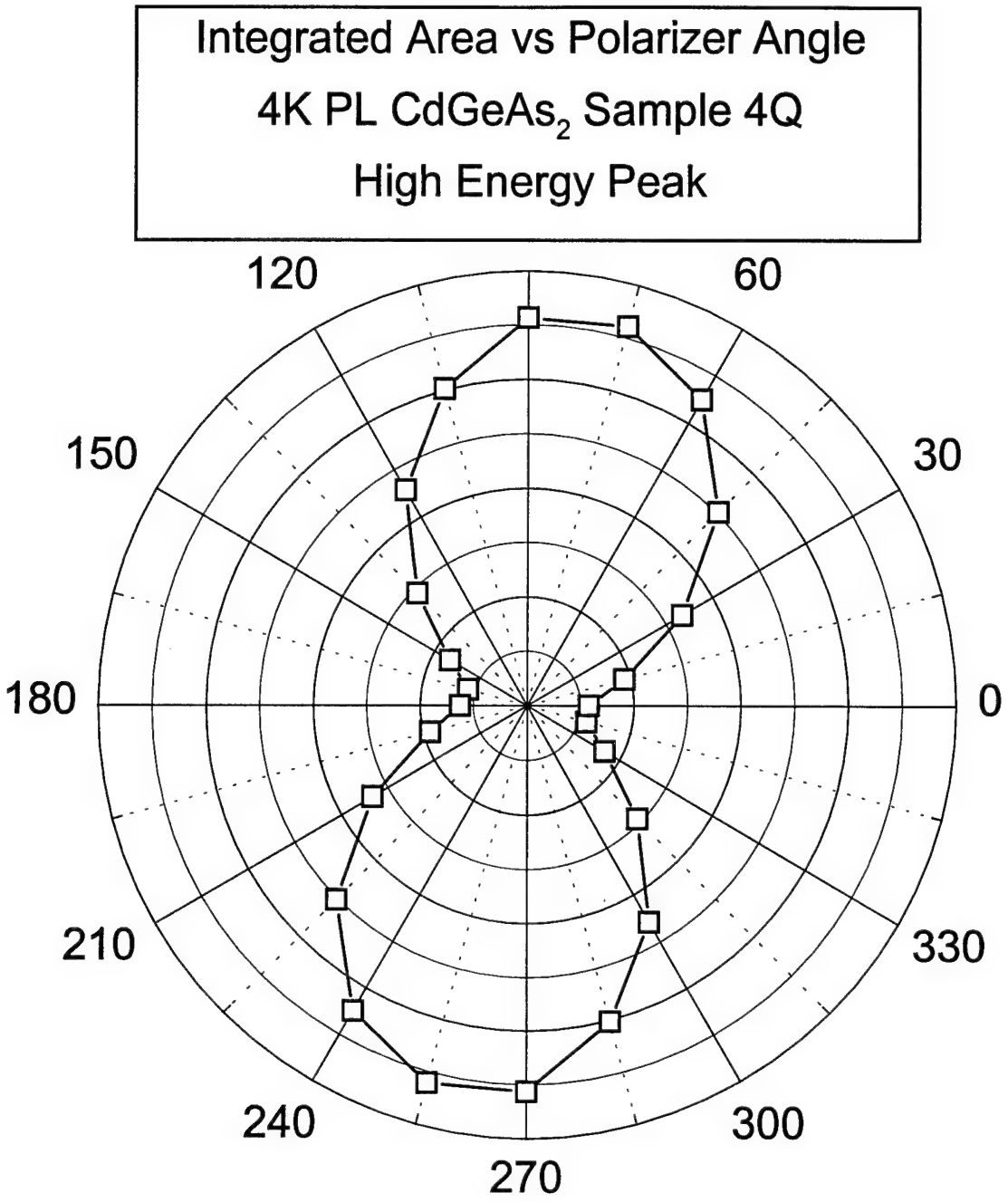

Figure 28. Variation in PL Integrated Intensity with Polarizer Angle for $CdGeAs_2$.

3.3.3. Spectra Corrected for System Response.

In order to accurately identify the location of peaks in the spectra, it is necessary to correct the measured spectra for the uneven response of the entire system to both wavelength and polarization. In the case of $CdGeAs_2$ including polarization was particularly important, since the PL was strongly polarized and the spectrometer has a strong polarization response of its own. The actual data used to correct the spectra are presented and discussed in appendix B. Fig. 29 shows a pair of spectra collected using a linear polarizer first parallel then perpendicular to the sample's c-axis. The c-axis was vertical in the sample chamber so that these two conditions could be cleanly separated; this was necessary because the sample's front facet is tilted at about 45 degrees to the entrance slit so the laser can be sent in through a side port on the cryostat. The variation in response of the spectrometer to polarization is expected to be maximized when comparing horizontal to vertical polarizations.

Fig. 30 shows the same spectra now corrected to make the left scale proportional to photon flux per unit wavelength. The sum of these two spectra, representing the total spectrum, is also shown. The tremendous noise seen above 0.8 eV shows where the cold filter cuts off; almost no light of higher energy made it to the detector during the calibration or data runs, so the curve here amounts to noise divided by noise. At the location on the sample used in this case (sample 2G), the low energy band is stronger than the high energy one; as the noisiness of both the corrected and uncorrected spectra hints, this is because the high energy band is much weaker than on the other samples shown. The intensity of the low energy band is much more consistent from sample to sample (varying by about a factor of 4).

Near 0.5 eV on the uncorrected vertical polarization spectrum there is an evidence of additional peak. This peak is weakened on the corrected spectrum, but it is still noticeable. This peak may indicate the presence of an additional acceptor level on this

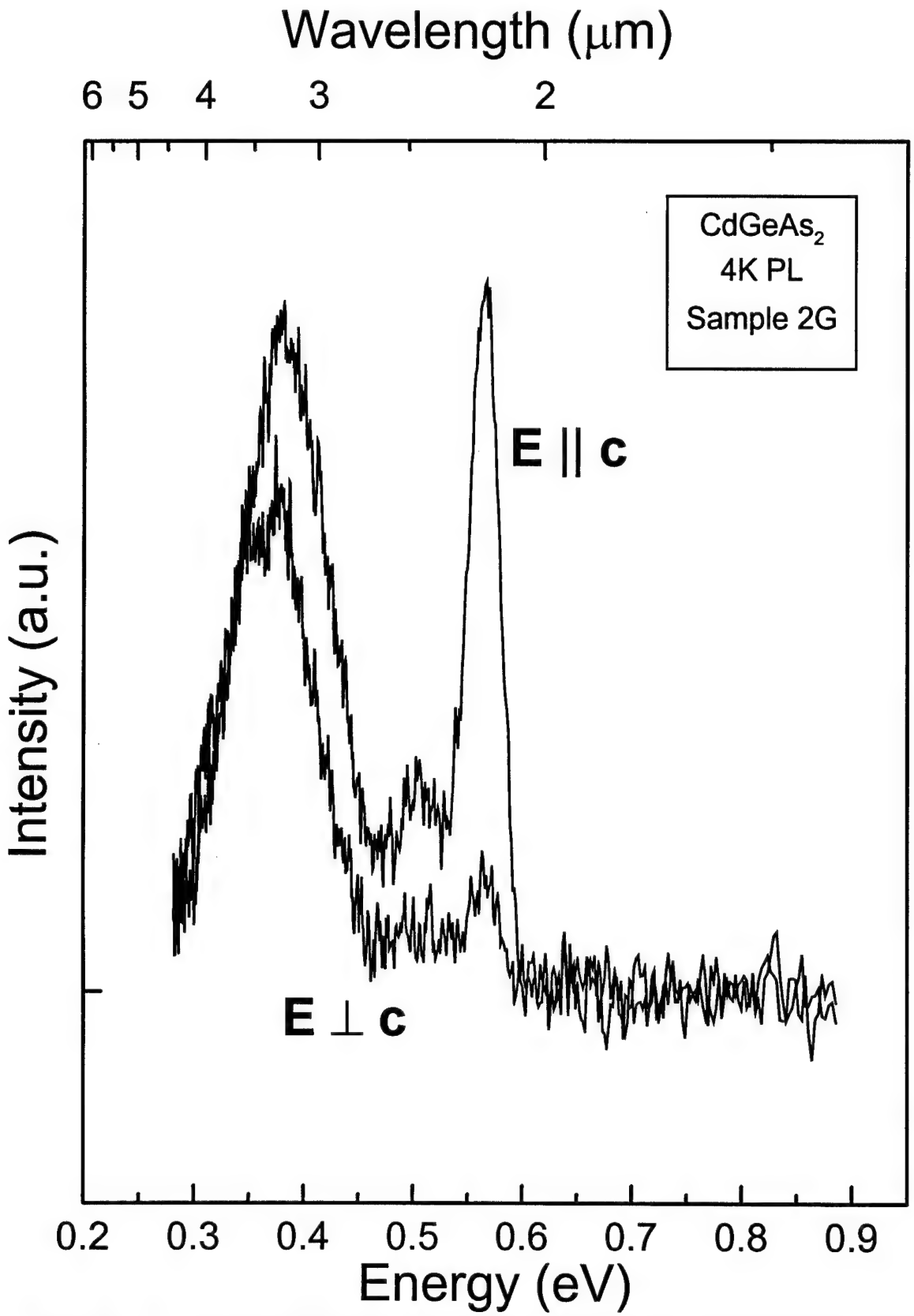

Figure 29. PL Spectra with Polarizer Parallel and Perpendicular to the c-axis for $CdGeAs_2$, Uncorrected Spectra.

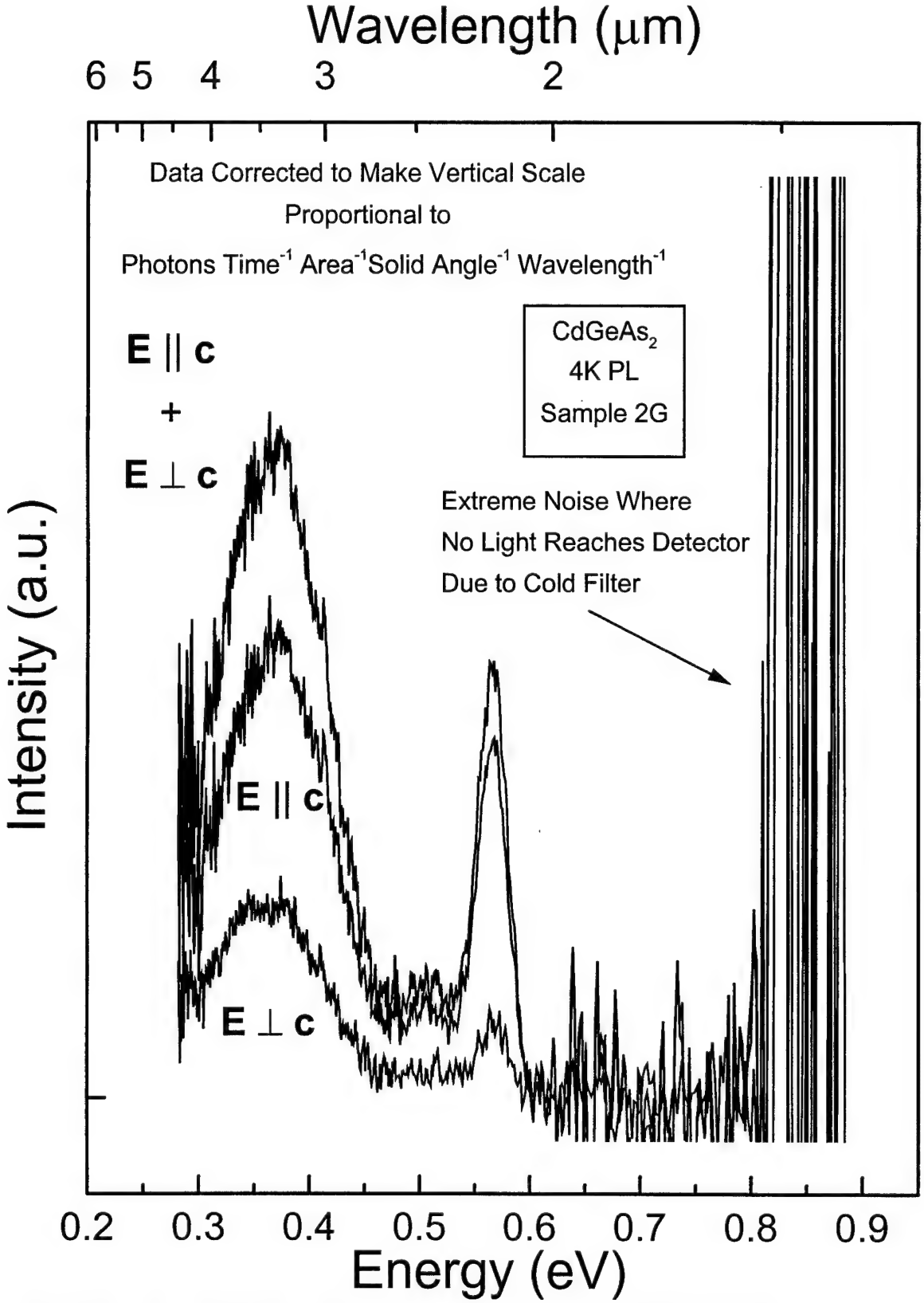

Figure 30. Polarized PL Spectra for $CdGeAs_2$, Corrected for Polarization Sensitive System Response.

sample. This is an interesting possibility because this particular sample (2G) is cut from the boule (2) which has shown the lowest optical absorption.

The degree of polarization (Π) can be computed as $\Pi = (I_{\perp}-I_{\parallel})/(I_{\perp}+I_{\parallel})$. This has been computed for the corrected spectra shown in Fig. 30, and is plotted as Fig. 31. This curve is unusable above about 0.6 eV where there isn't any light. At lower energies the trend is clear - the degree of polarization fades as the transitions being observed move away from the band edge.

3.3.4. Further Analysis of Room Temperature PL.

The laser power and polarization analyses carried out for low temperature PL and discussed above were repeated for the room temperature PL peak observed on sample 4M. Fig. 32 shows a sequence of PL spectra accomplished with decreasing laser power levels. Unlike the low temperature case, no peak shift is observable here. As the laser power varies by more than a decade across this set of spectra, a shift of more than 10 meV would be expected if the PL mechanism were the same here as in the case of the spectra on Fig. 24. Despite the noise level on these spectra (Fig. 32) a shift this large would have been noticeable. This provides additional evidence the room temperature PL is not due to DAP's. Fig. 33 shows polarization resolved room temperature PL spectra which have been corrected for the polarization sensitive response of the system. This correction has made these spectra especially noisy at high energies where the system response is falling. The PL peak for the **E**$\parallel$**c** polarization and the unpolarized case falls near 0.55 as it does for the uncorrected spectra. The PL peak is seen to be slightly blue-shifted for the **E**$\parallel$**c** polarization, the peak falling near 0.56 eV. While the emission for **E**$\parallel$**c** is seen to be stronger than that for **E**$\perp$**c** as expected, the reabsorption of the PL by the sample should also be greater for the **E**$\parallel$**c** polarization. This, in combination with the fact that the absorption is growing quickly with photon energy in this near-band-edge spectral region explains this blue-shifting nicely. The degree of polarization of the room

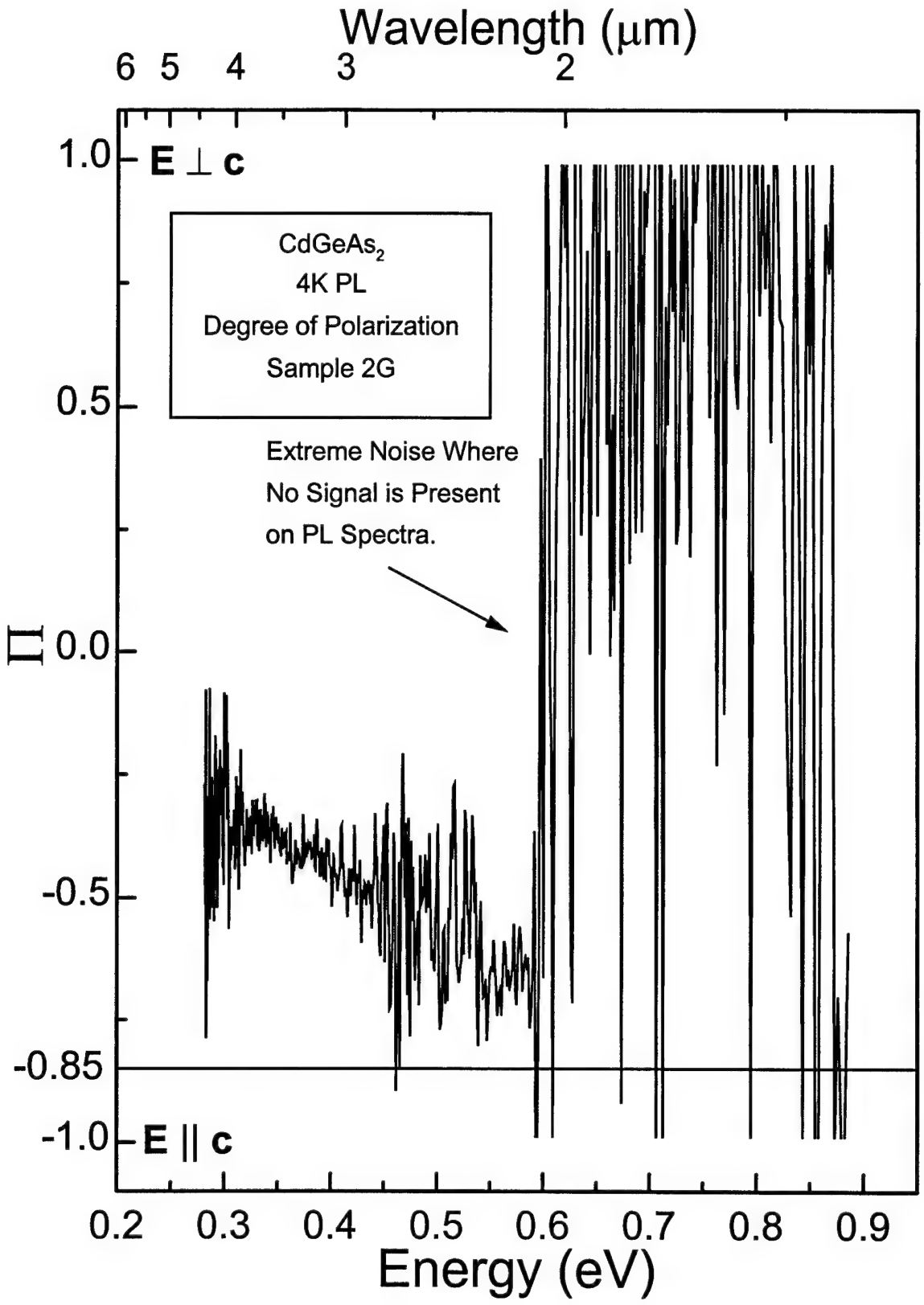

Figure 31. Degree of Polarization of PL Spectrum for $CdGeAs_2$.

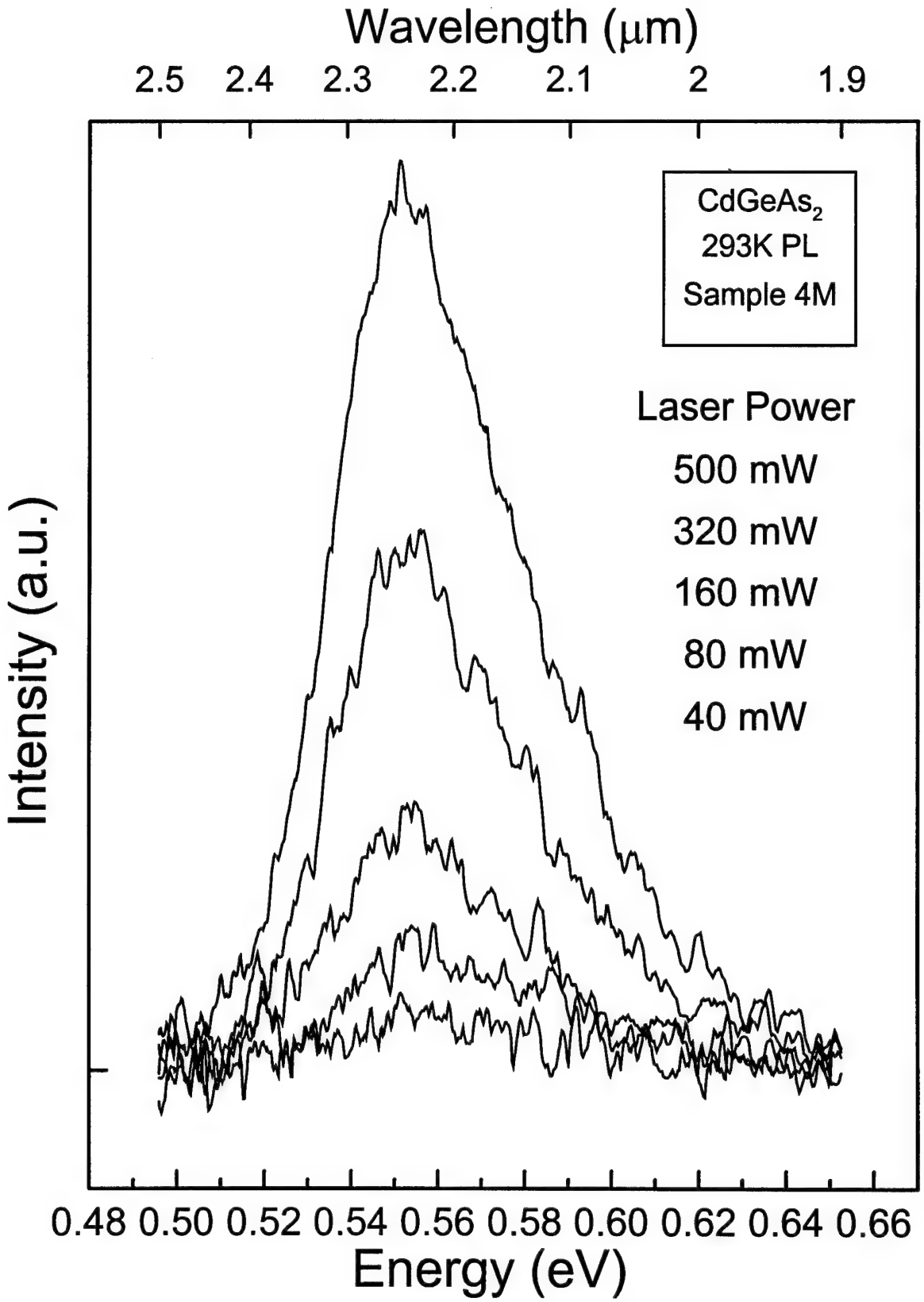

Figure 32. Room Temperature PL Spectrum for $CdGeAs_2$.

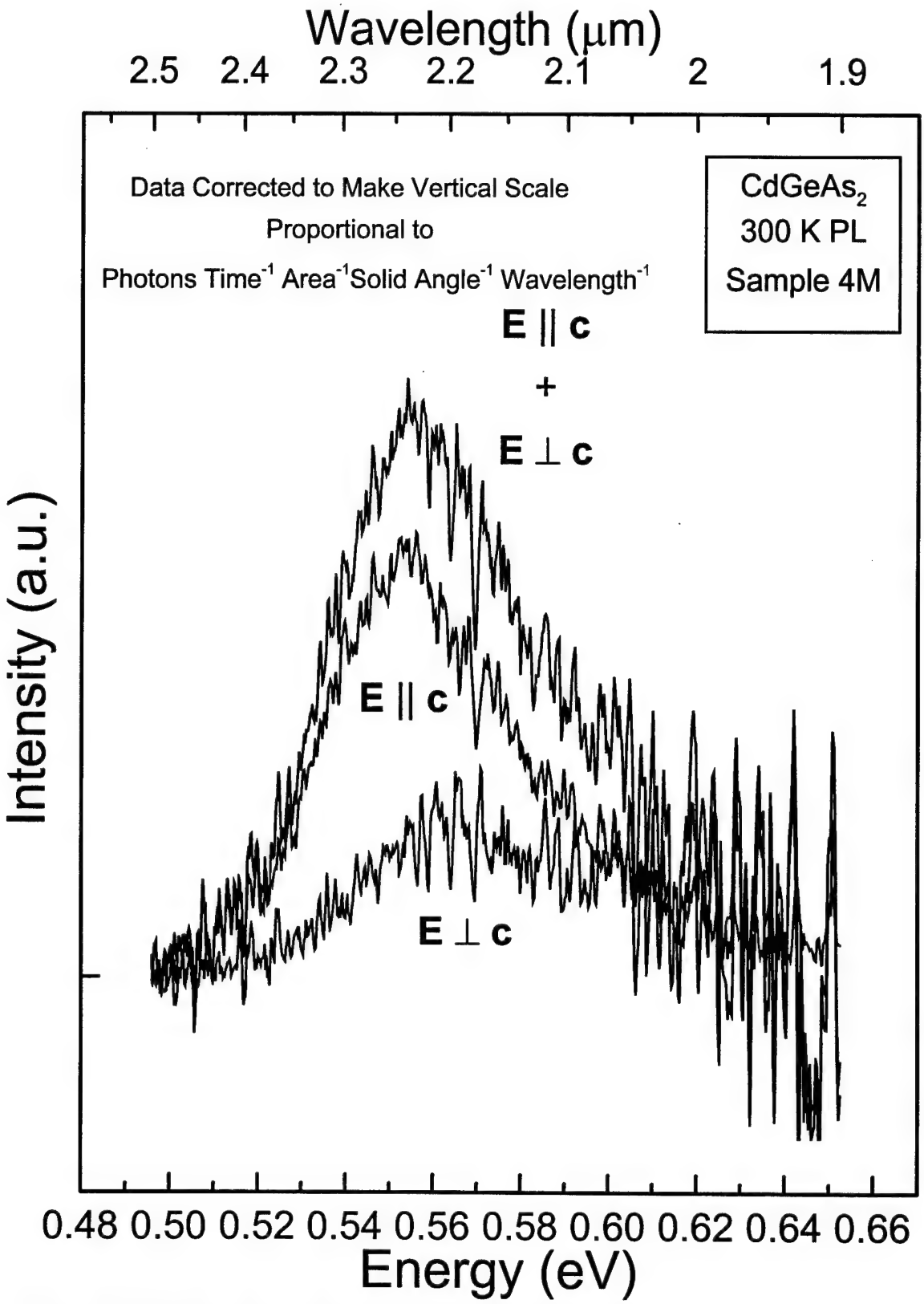

Figure 33. $CdGeAs_2$ Room Temperature PL Spectrum, Corrected for Polarization Sensitive System Response.

temperature PL emission is shown on Fig. 34. Unlike the low temperature case, illustrated on Fig. 31, the degree of polarization falls as the photon energy increases. At the lower energies displayed, just before the noise becomes dominant, the degree of polarization is seen to be approaching 0.85, which has been previously shown to be equivalent to the predicted 12:1 polarization ratio. If it is assumed that PL is created in a 12:1 polarization ratio, then this curve can be taken as evidence that not too much is reabsorbed in exiting the crystal. If half the PL emission were reabsorbed almost all of this loss would come from the E||c polarization, since the absorption coefficient should be 12 times larger for this polarization. This would then cut the measured polarization ratio about in half for the emitted light. A polarization ratio of 6:1 corresponds to a degree of polarization of about 0.7; the case realized at low energies on Fig. 34 is about in line with this estimate.

3.3.5. PL Uniformity.

The PL measured varied substantially from sample to sample, and even across a single sample. The low energy peak was apparent in all samples, it was always located near 0.38 eV, did not appear to move in position, and varied in brightness by about a factor of four across all samples studied. The high energy peak varied in intensity from sample to sample greatly, this amount can't really be quantified since it did not show up at all on one sample (sample 5031), so the variation was effectively infinite. Across the measured spectra where this peak was seen, it varied in intensity by two orders of magnitude. While sample 5031 had a different orientation than that of all but one of the samples with known orientations, this sample also appeared to be the poorest to the naked eye, showing some evidence of porosity or pitting even on polished facets. The absence of the high energy PL peak seems more attributable to the sample's quality than its orientation, although this orientation would greatly reduce the strength of the high energy peak if it were present.

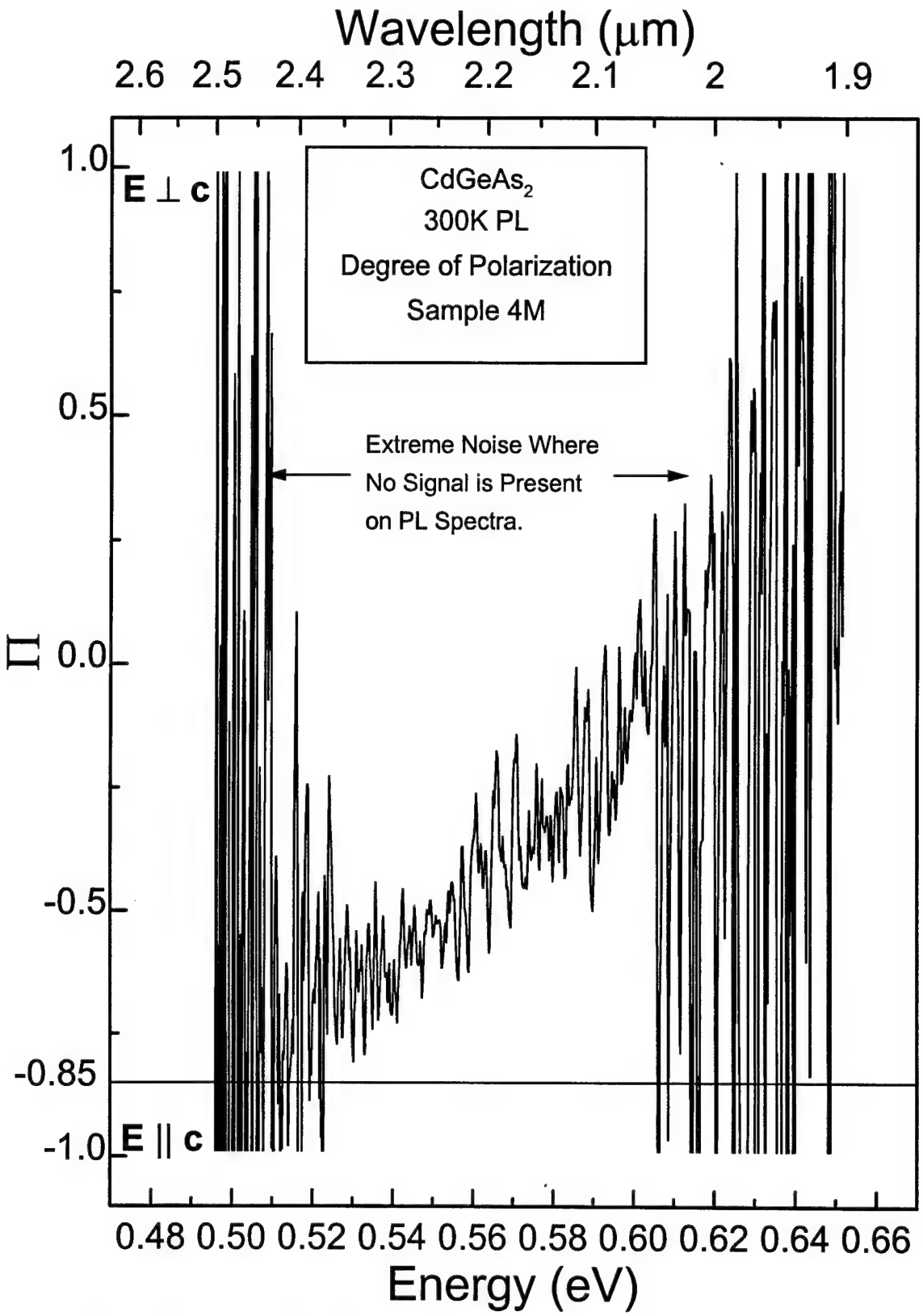

Figure 34. Degree of Polarization of Room Temperature PL Spectrum for $CdGeAs_2$.

As a comparison of the homogeneity of the samples studied, as well as a demonstration of their variability, spectra are provided of the most variable sample and one of the better ones; better being in terms of both brightness and uniformity. Fig. 35 shows a sequence of spectra taken on sample 5110, deliberately varying only the position on the sample where the laser spot fell. The low energy peak is seen to vary in magnitude by about a factor of four, while there is no noticeable change in its position. On the other hand the high energy peak varies in magnitude by almost twice as much, and the position of the peak is seen to move around apparently independently of its height. If there is a correlation to be made between the two peaks, it is that they seem to be competing with each other - the highest low energy peak is on the same curve as the lowest high energy peak. Sample 5110's PL is the brightest of any sample not grown by Lockheed Sanders, other than the PL variability it appears to be an excellent specimen. Fig. 36 shows a pair of spectra taken at opposite sides of sample 4M. There is but little change in the heights of the two peaks observed, and in position the peaks do not appear to move at all. The samples cut from boule 4 have the brightest PL, their superior uniformity is a bonus which makes data interpretation much less ambiguous.

3.3.6 Fitting to PL Results.

More sophisticated data analysis allows better use to be made of the PL data collected. The PL spectra can be fitted to functional forms characteristic to the physical processes involved, thereby estimating various physical parameters. The scatter apparent on Fig. 20 due to the noisiness of the signal (seen on Fig. 18) is also due to assignment of the peak position based solely on the maximum value in the spectra. This scatter can be greatly reduced by fitting the spectra to an appropriate mathematical function.

If the spectrum shown in Fig. 22 is predominantly due to band-to-band recombination, it is possible to fit this spectrum to the anticipated lineshape from this process. The lineshape expected for band-to-band recombination in a direct bandgap

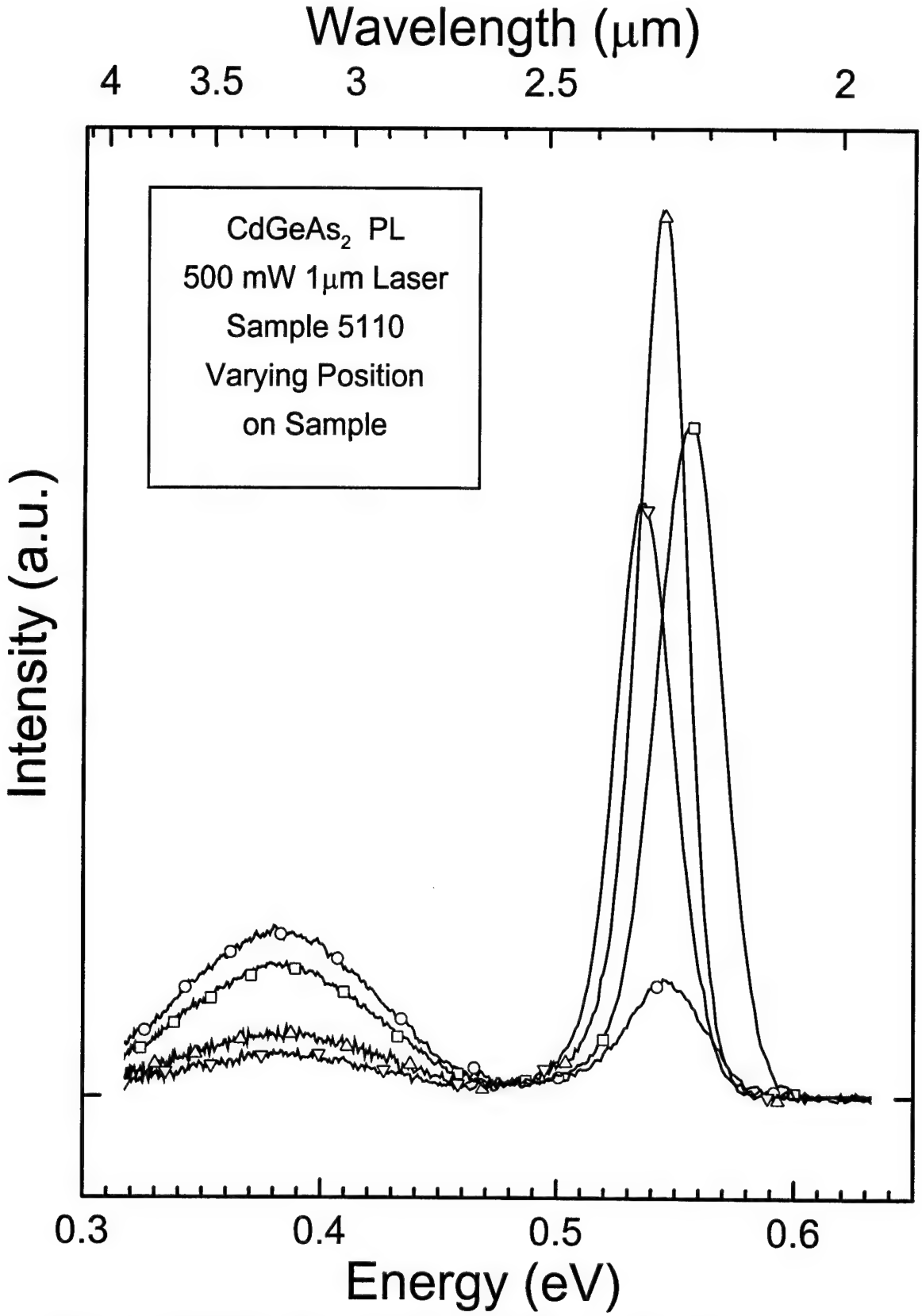

Figure 35. Variability of PL Spectrum for $CdGeAs_2$ Sample 5110.

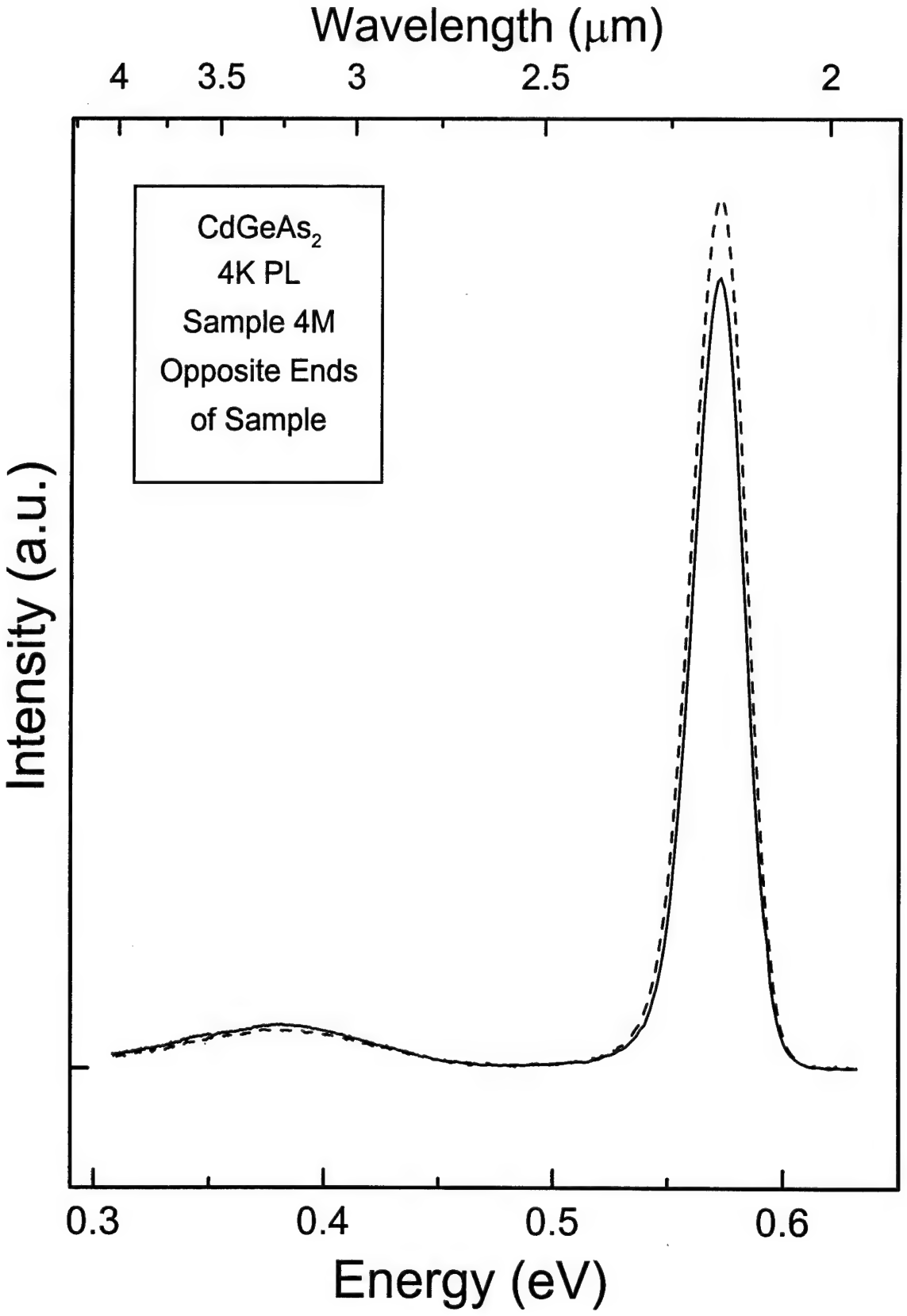

Figure 36. Variability of PL Spectrum for $CdGeAs_2$ Sample 4M.

semiconductor is proportional to the product of the density of states and the Fermi function for the distribution of carriers;[30] that is:

$$\rho(E) \propto \left(E - E_g\right)^{1/2} \exp\left(-\frac{E}{kT}\right) \qquad [3]$$

where ρ is the PL measured, E is the energy of the detected photons, k is Boltzmann's constant, T is the temperature of the carriers, and E_g is the semiconductors bandgap. If the carrier distribution is degenerate this equation should not be used. This equation fits fairly well to the right side of the spectrum as seen in Fig. 22 and Fig. 23, but it has far too sharp of a turn-on compared to the low energy tails seen here. Since this material is p-type, at room temperature there are plenty of holes available, so the carrier temperature here should be that of the electrons. Additionally, since the carriers recombine quickly, the electron temperature may be elevated from the lattice temperature, not having enough time to equilibrate with the lattice before recombining. Defects in a crystal cause band-tailing - the effective density of states does not go to zero at the band-edge, but rather it falls exponentially for energies below the bandgap. This effect can be incorporated into the above equation by convolving such an exponential function across the density of states as follows:

$$\rho(E) \propto \left\{\left(E - E_g\right)^{1/2} \bigstar \exp\left(\frac{E}{E_0}\right)\Theta(-E)\right\}\exp\left(-\frac{E}{kT}\right) \qquad [4]$$

where we have added E_0, the Urbach parameter, which characterizes the steepness of the density of states near the band-edge,[31] Θ, the unit step function which serves to restrict the tunnelling involved in band-tailing to states of lower energy, and the convolution operator, $\bigstar$. This function now has the minimum number of parameters necessary to match the coarsest features seen on Fig. 23. Other than the overall scale, we have E_g which locates the peak (within about kT), T which governs the slope on the high energy

side of the peak, and E_0 which governs the slope on the low energy side of the peak. Fig. 37 shows a comparison of the spectrum shown in Fig. 22 to this function using parameters: $kT = 27.7$ meV, $E_0 = 10.4$ meV and $E_g = .543$ eV. It is easy to see that this model has some deficiencies. The side slopes and the peak position are all not quite right, and fixing one feature only makes the others much worse. This best fit is a compromise due to one basic problem: the model spectrum has a sharper peak than the experimental data, and there is no variable in the fit which addresses sharpness. There are several possible causes for this. The instrument resolution will broaden the peak measured experimentally, but again this effect should be much smaller than the discrepancy seen here. Variations in the bandgap throughout the studied part of the sample could certainly account for the differing peak curvatures. If an additional parameter were added to account for possible bandgap variations in the sample, an excellent fit between the model and the experiment could be expected. Convolving a Gaussian across the density of states incorporates this effect into the model spectra, the Gaussian's variance being the only new parameter added. The risk here is that this combination of parameters is now large enough to give an excellent fit to a wide range of possible peak shapes, even if the physics underlying the actual peak shape has little to do with the justification used for the model. Still in this case all 5 parameters now involved in fitting a peak carry physical meaning: overall intensity, band-gap, carrier temperature, band-tailing, and band gap variability.

Of course, a discrepancy in peak shapes between the model and the data could also mean that the model is wrong. The posited source of the luminescence could be incorrect, an important effect could have been assumed to be unimportant (for instance reabsorption of the luminescence, or the electrostatic attraction between electrons and holes), or if the quasi-fermi levels have been driven into the bands, the lineshape would be changed.

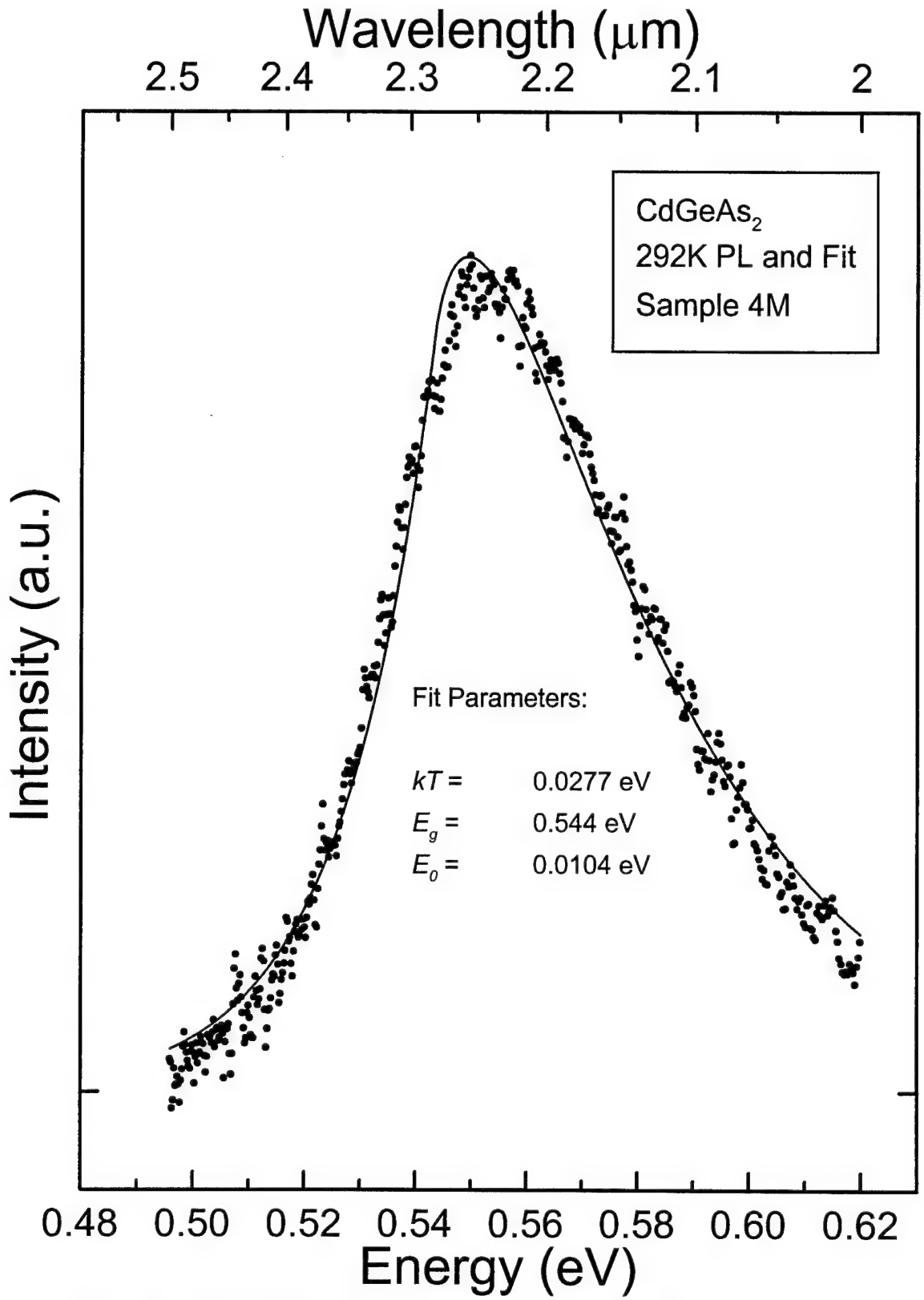

Figure 37. Comparison of $CdGeAs_2$ Room Temperature PL Spectrum with Proposed Model

Adding a Gaussian distribution to Eq. 4 results in a predicted PL lineshape given by:

$$\rho(E) = A\left\{\left(E - E_g\right)^{1/2} \bigstar \exp\left(\frac{E}{E_0}\right)\Theta(-E) \bigstar \exp\left(-\frac{E^2}{2\sigma_E^2}\right)\right\}\exp\left(-\frac{E}{kT}\right) \qquad [5]$$

Where σ_E is the width of the Gaussian used to soften the peak, and A has been added to make the overall amplitude of the lineshape explicit. Using a non-linear least-squares fitting routine based upon the Levenberg-Marquardt algorithm[32] to compute the parameters of Eq. 5 for the data of Fig. 22 results in the fit presented on Fig. 38. The program required as inputs the measured spectrum (Fig. 22) along with a noise estimate (if meaningful error bounds are desired), plus the fit function (Eq. 5), the derivatives of this function with respect to each of the parameters to be fitted, and a starting guess for each of these parameters. The output from the program included least-squares sense optimized values for each parameter, and error bounds for these values. The computer implementation of this the function and its derivatives uses FFT's to evaluate the convolutions, and simple linear interpolation to move from the evenly (but tightly) spaced FFT data to the unevenly spaced (in energy) PL data.

The determined parameters shown for the fit curve on Fig. 38 all seem quite reasonable. The determined bandgap value of 0.547 eV coincides quite closely with the peak position in the spectrum. This number falls between bandgap values reported by others (as discussed in section 2.5); further analysis of the appropriateness of this value will be addressed in the conclusions. The value determined for kT of 0.0249 eV corresponds to a temperature of 289 K, very close to the room temperature measured in the laboratory of 292 K at the time the data was taken. There is little with which to compare the Urbach parameter value of 9.2 meV, but this value is comparable to E_0's measured for other materials. The amount of spread or uncertainty in the bandgap,

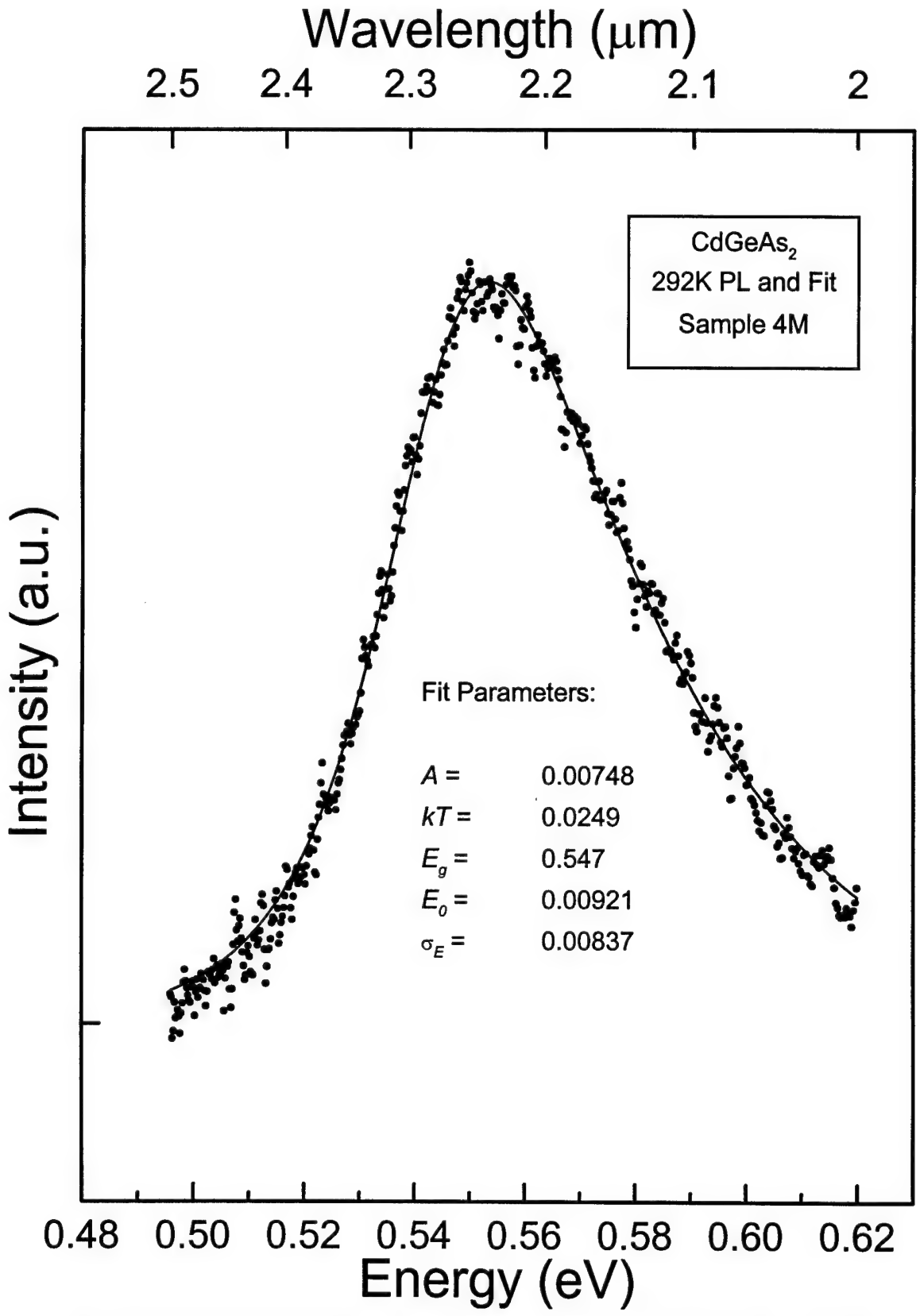

Figure 38. Room Temperature PL Spectrum and Improved Model for $CdGeAs_2$.

characterized by σ_E, was determined to be 8.4 meV. This value is relatively small with respect to the bandgap determined, amounting to 1.5%, and it is also relatively small relative to the difference in bandgap values determined otherwise (as discussed in section 2.5).

Excellent results were obtained by using this fitting program to compute less noise sensitive peak positions for the noisier of the curves seen on Fig. 18. Fig. 39 shows the PL spectrum obtained at 225 K, along with the curve fit through this data. The fitted curve tracks the trend of the experimental data very closely. The fitted curve peaks at 0.565 eV; this is about the peak position which would be picked by eye from this data. The fit curve appears uninfluenced by the two outlier data points which fall near 0.577 eV. This is a big improvement over attempts to find a peak position after smoothing the data by adjacents averaging, where the maximum remained near the outlier points even after averaging the 10 points on both sides of each data point into every data point.

Fig. 40 shows the results obtained at 120 K. The fit function only addressed data points above 0.54 eV, because there is evidence of a broad weak peak below this energy. If the function were fitted to the whole range the low energy side of the fit function would be greatly distorted by the presence of this additional peak. Again the fit function appears to follow the trend of the data with good fidelity, and accurately identifies the peak location.

Fig. 41 shows the results obtained at 70 K. The fit does not work on this spectrum. The parameters of Eq. 5 cannot be adjusted to give a spectrum with the shape of the PL spectrum seen in this figure. This is evidence that the physical model Eq. 5 is based upon does not apply in this case. At lower temperatures the fit continues to be equally poor. The transition from bad to good quality fits of the model to the spectra coincides with the jump in PL peak energy seen on Fig. 20 in the 80-100 K region.

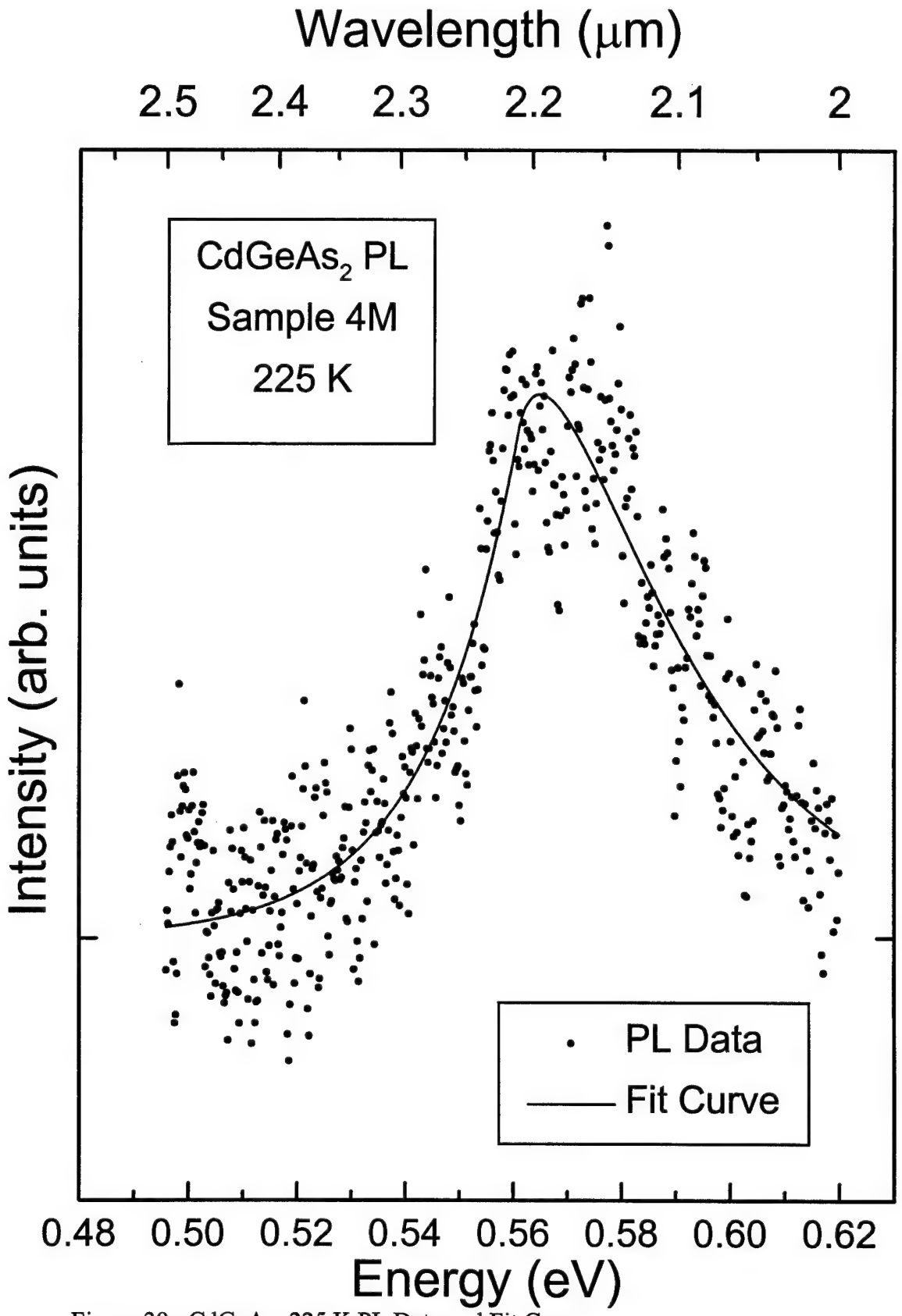

Figure 39. $CdGeAs_2$ 225 K PL Data and Fit Curve

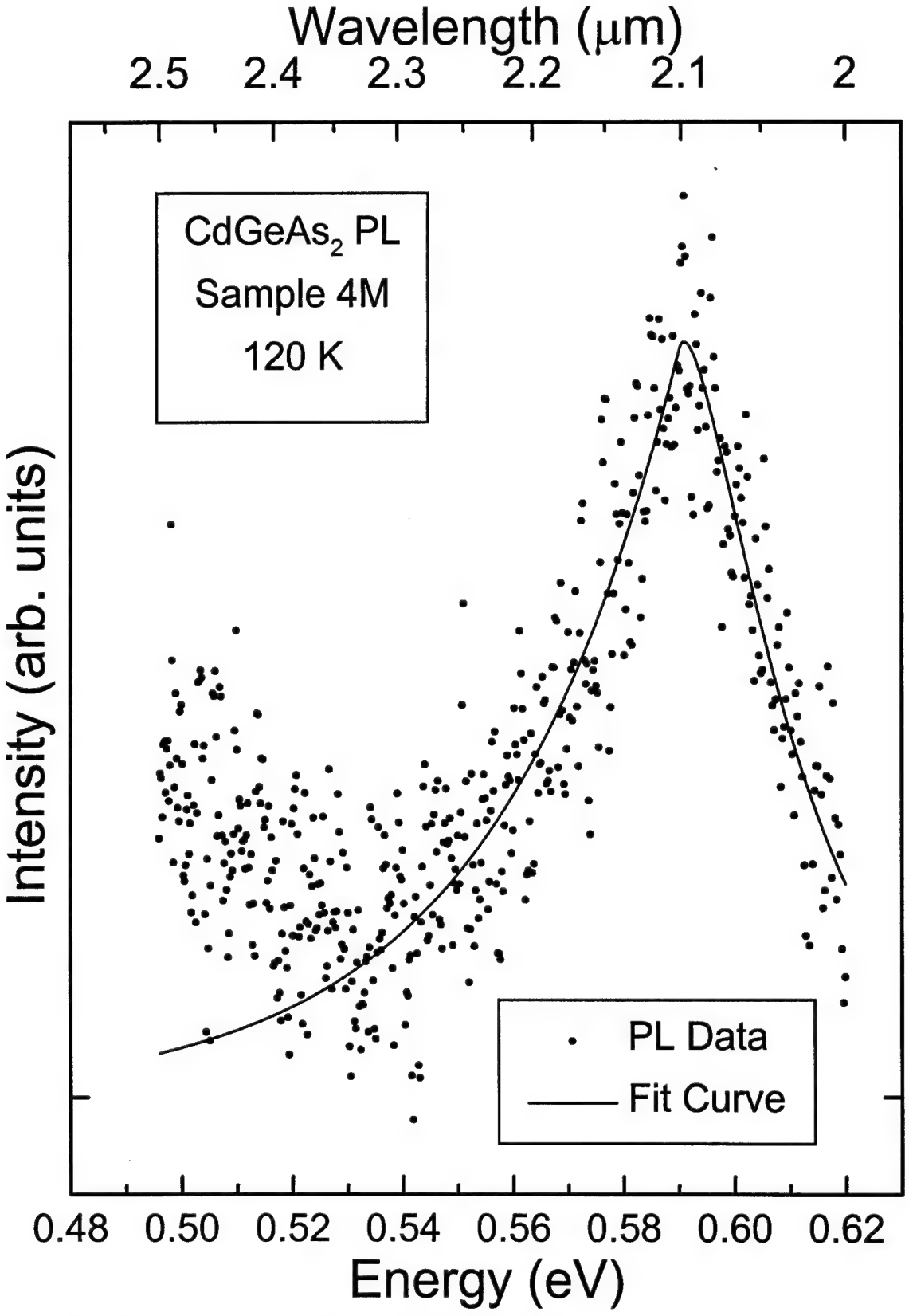

Figure 40. $CdGeAs_2$ 120 K PL Data and Fit Curve

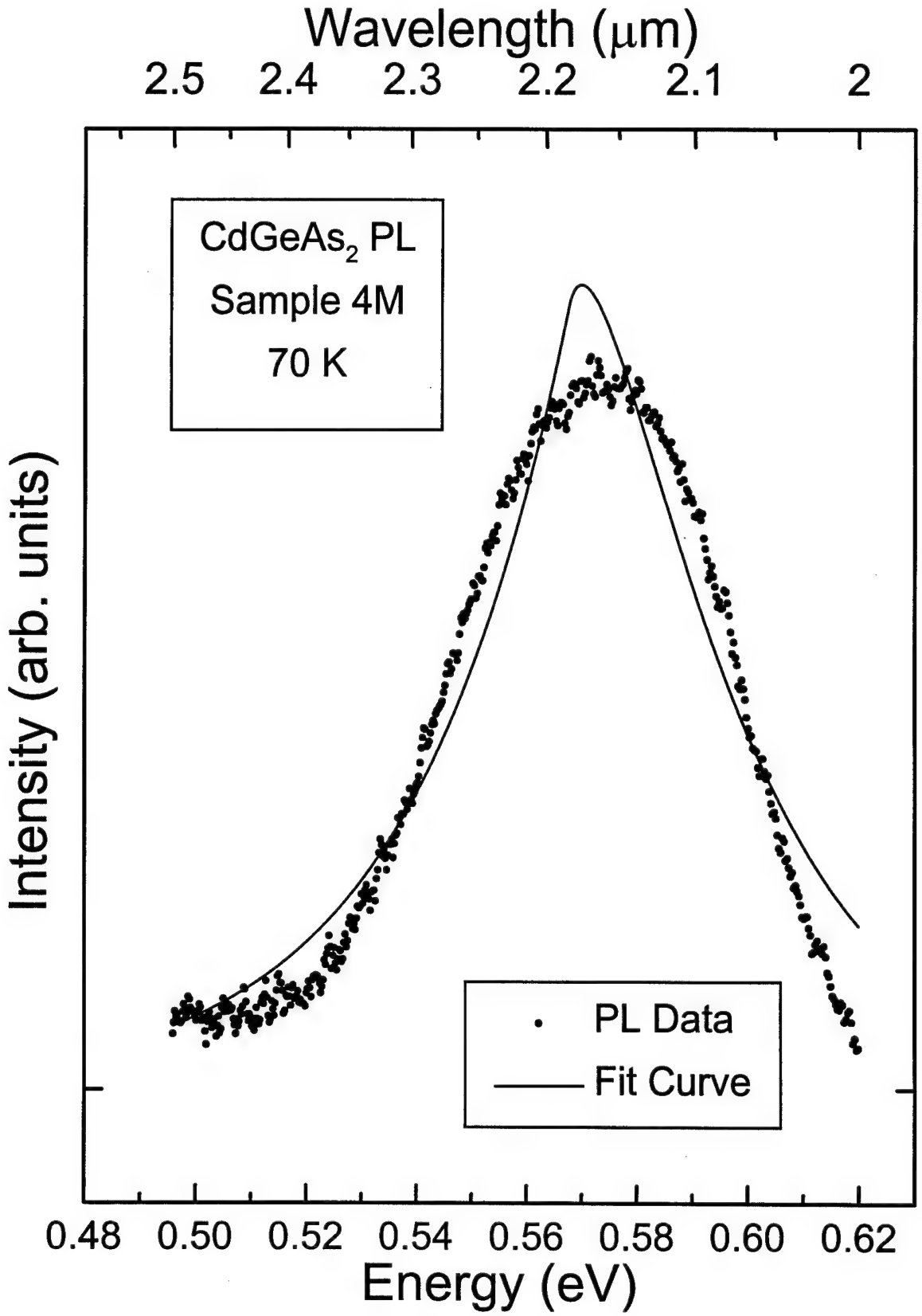

Figure 41. $CdGeAs_2$ 70 K PL data and fit curve

This fitting program was applied to all the PL spectra responsible for the wide scatter of data points seen on Fig. 20. Fig. 42 shows the resulting fitted and smoother peak position dependence, along with the original scattered data.

3.4. PL on $ZnGeP_2$.

3.4.1. PL on $ZnGeP_2$ through the Mid-Infrared.

The broad peak of the PL signal from $ZnGeP_2$ has been seen still tailing down when the response limit is reached for Ge detectors and photomultiplier tubes; this happens at around 0.7 eV and 1.2 eV respectively.[33] There have been no reported efforts to study the luminescence of this material further into the infrared. The mid-infrared PL equipment used for $CdGeAs_2$, as discussed above is ideal to this purpose. When $ZnGeP_2$ is excited with 500 mW of power from the 1μm diode laser an additional small peak is seen near 0.35 eV, just past what appears to be the dying tail of the main peak. Fig. 43 shows a spectrum obtained under these conditions. Fig. 44 shows this spectrum again, but now corrected for the instrument's response. Prior to this successful experiment several attempts to obtain PL from the same sample (16c) of $ZnGeP_2$ with a shorter wavelength laser and an InSb detector had failed to measure any PL at all. The laser used for these unsuccessful experiments was an air cooled argon-ion laser operating at either 514.5 nm or 488.0 nm, and at powers only as high as 40 mW. While this should have been enough power to generate a measurable amount of PL, the signal may have been too weak to acquire based on the kind of careful, but coarser, alignment that can be accomplished before a signal is found.

3.4.2. PL on $ZnGeP_2$ in the Visible and Near-Infrared.

Previous work showed no significant variation of the PL signal for 350 nm radiation as the excitation power was raised from 8 to 85 mW ;[27] the PL peak remained

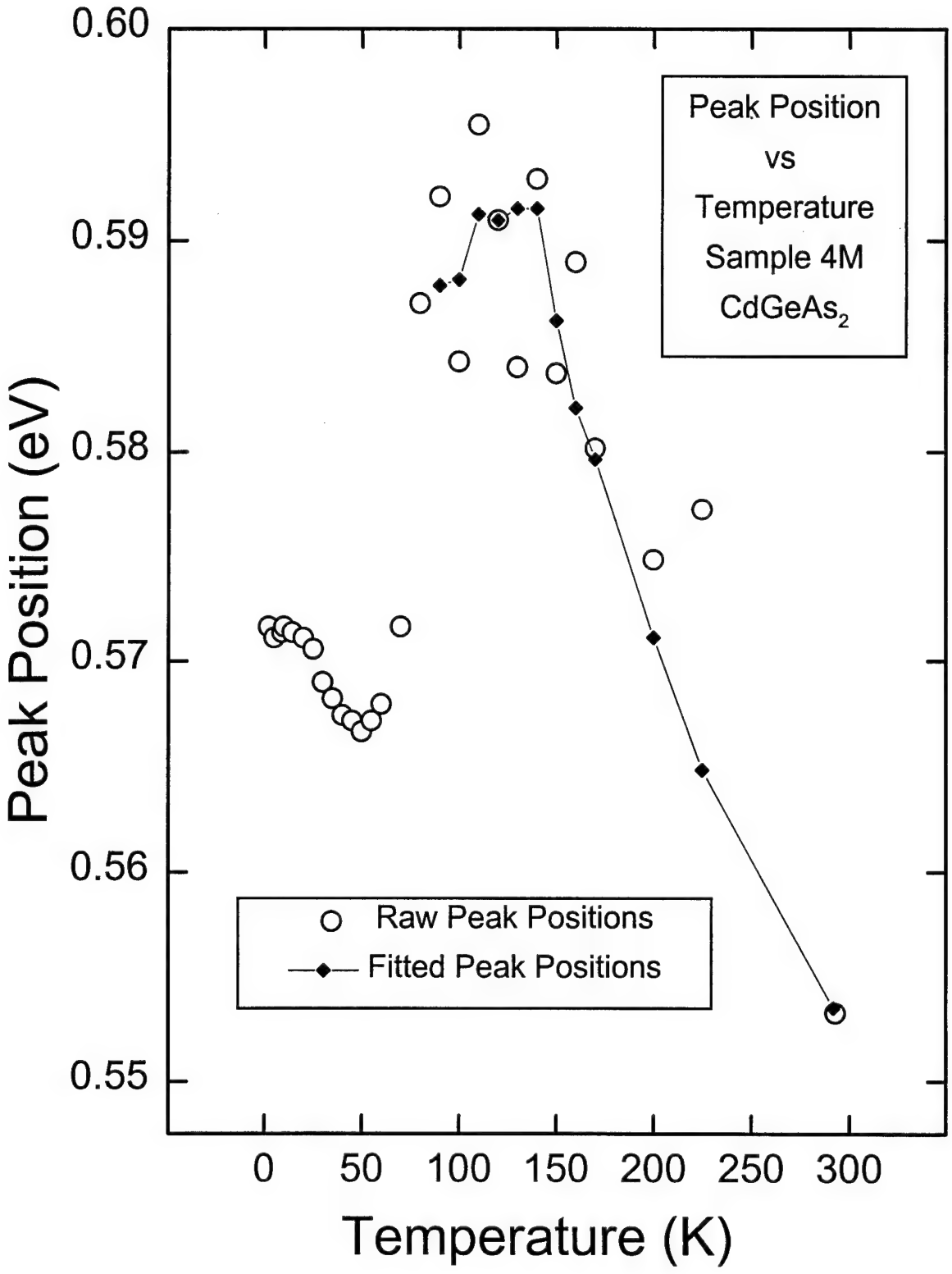

Figure 42. Raw and Fitted PL Peak Position vs Temperature for $CdGeAs_2$

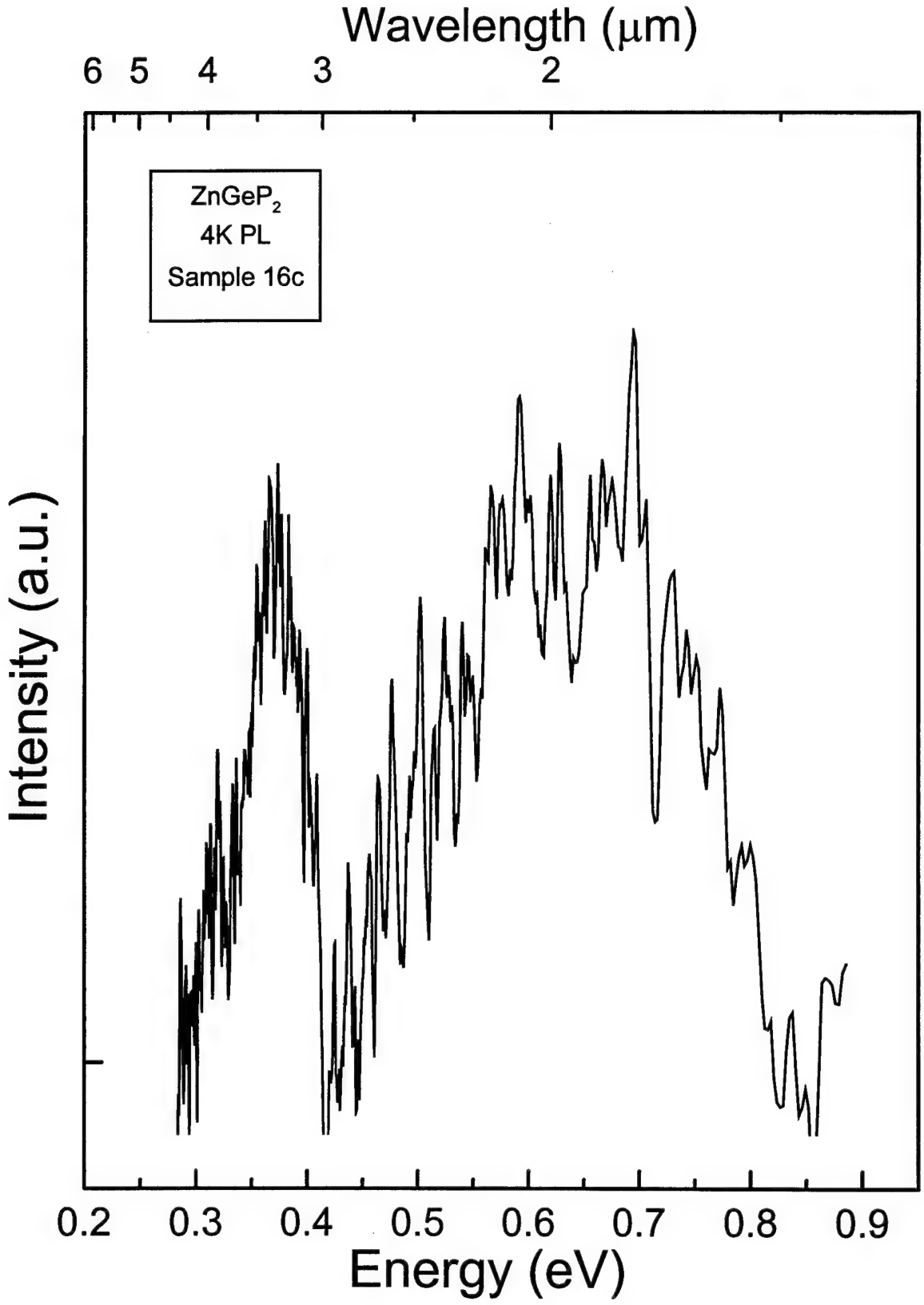

Figure 43. Uncorrected Mid-IR Spectrum for $ZnGeP_2$.

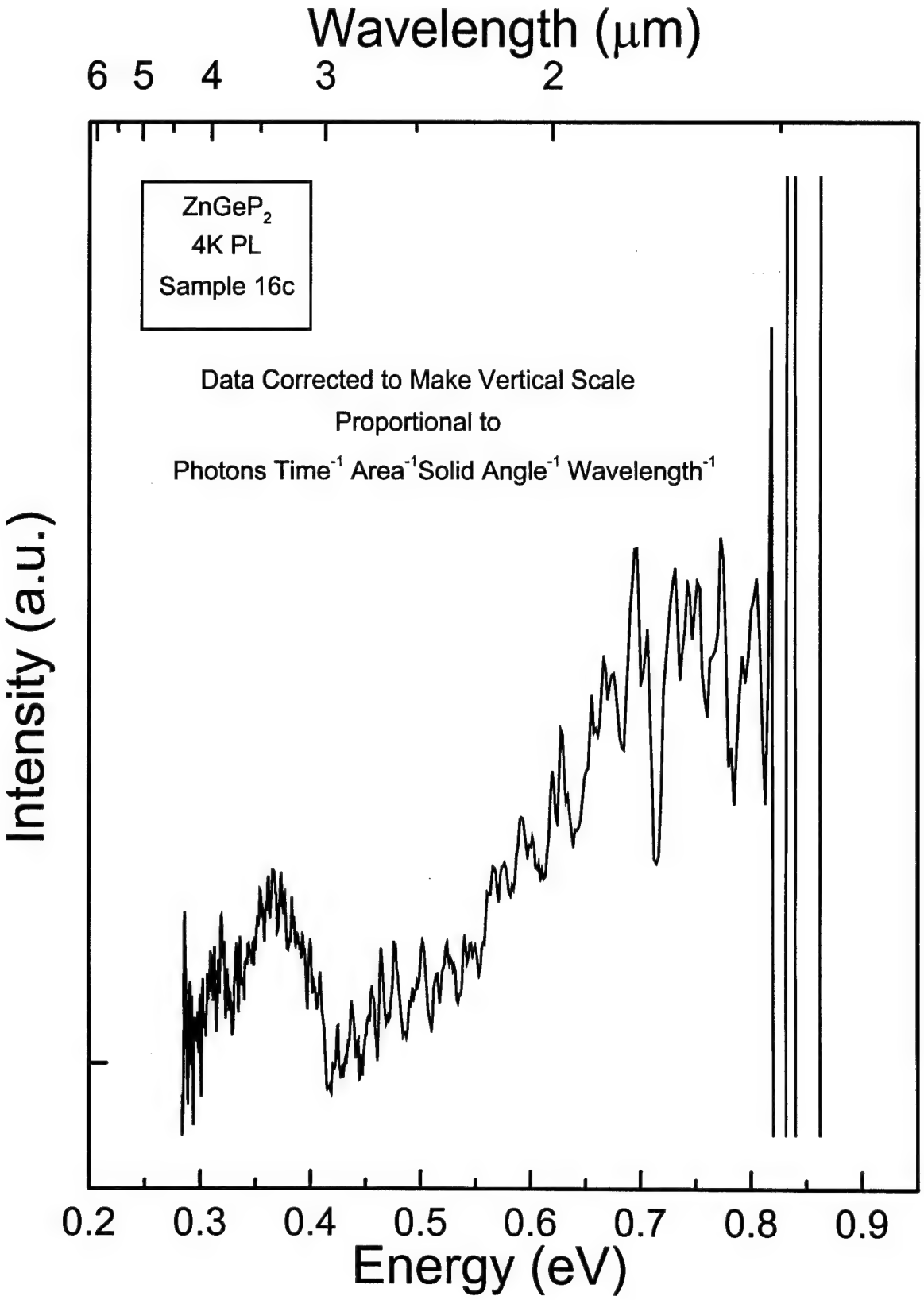

Figure 44. Corrected Mid-IR Spectrum for $ZnGeP_2$.

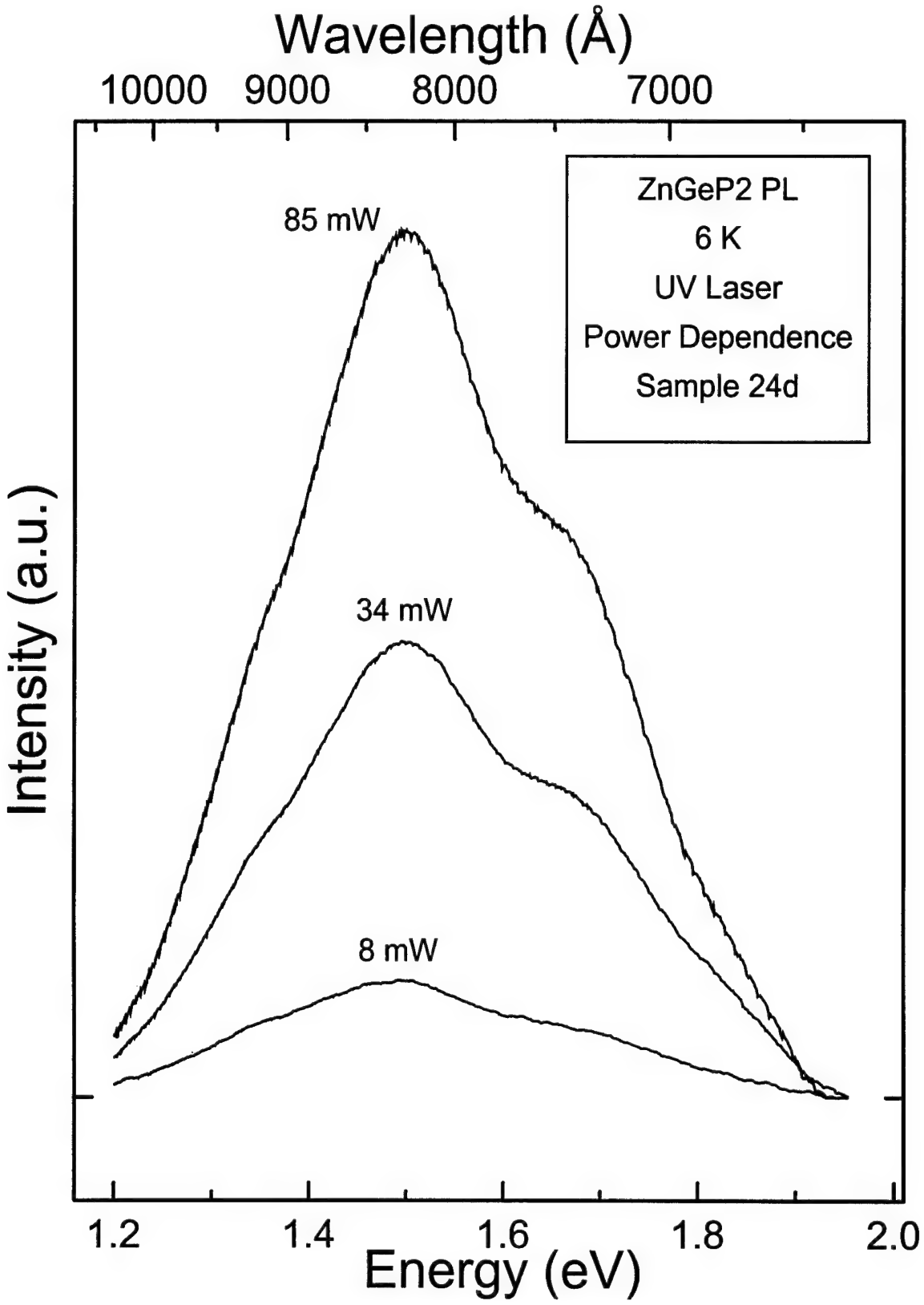

Figure 45. UV Laser Power Dependence, $ZnGeP_2$ PL, Sample 24d.

at 1.5 eV and a strong shoulder peak was always present at 1.67 eV (Fig. 45). Using 530 nm excitation, and varying the power from 3 to 100 mW, a significant peak shift did occur. The PL peak moved from 1.43 to 1.46 eV as the power increased from 10 to 100 mW, and at the lowest excitation level the peak appeared at 1.35 eV. Fig. 46 shows these spectra, the peak shift is somewhat hard to discern since the peak height varies so much over this wide range of excitation powers. Fig. 47 shows these same spectra again, but now each spectrum has been scaled to have the same peak amplitude, and the peak shift is much easier to notice.

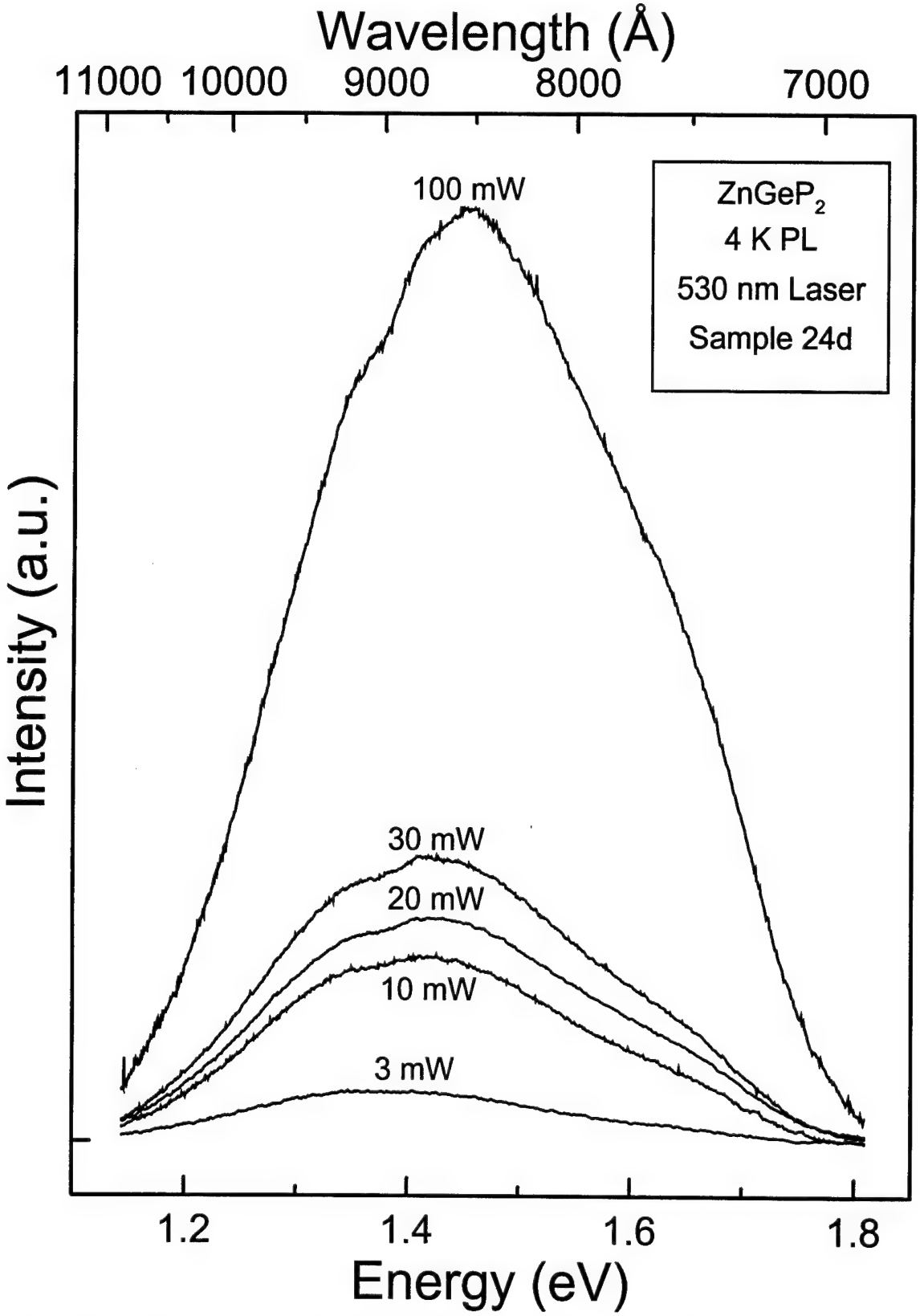

Figure 46. 530 nm Laser Power Dependence, $ZnGeP_2$, Sample 24d.

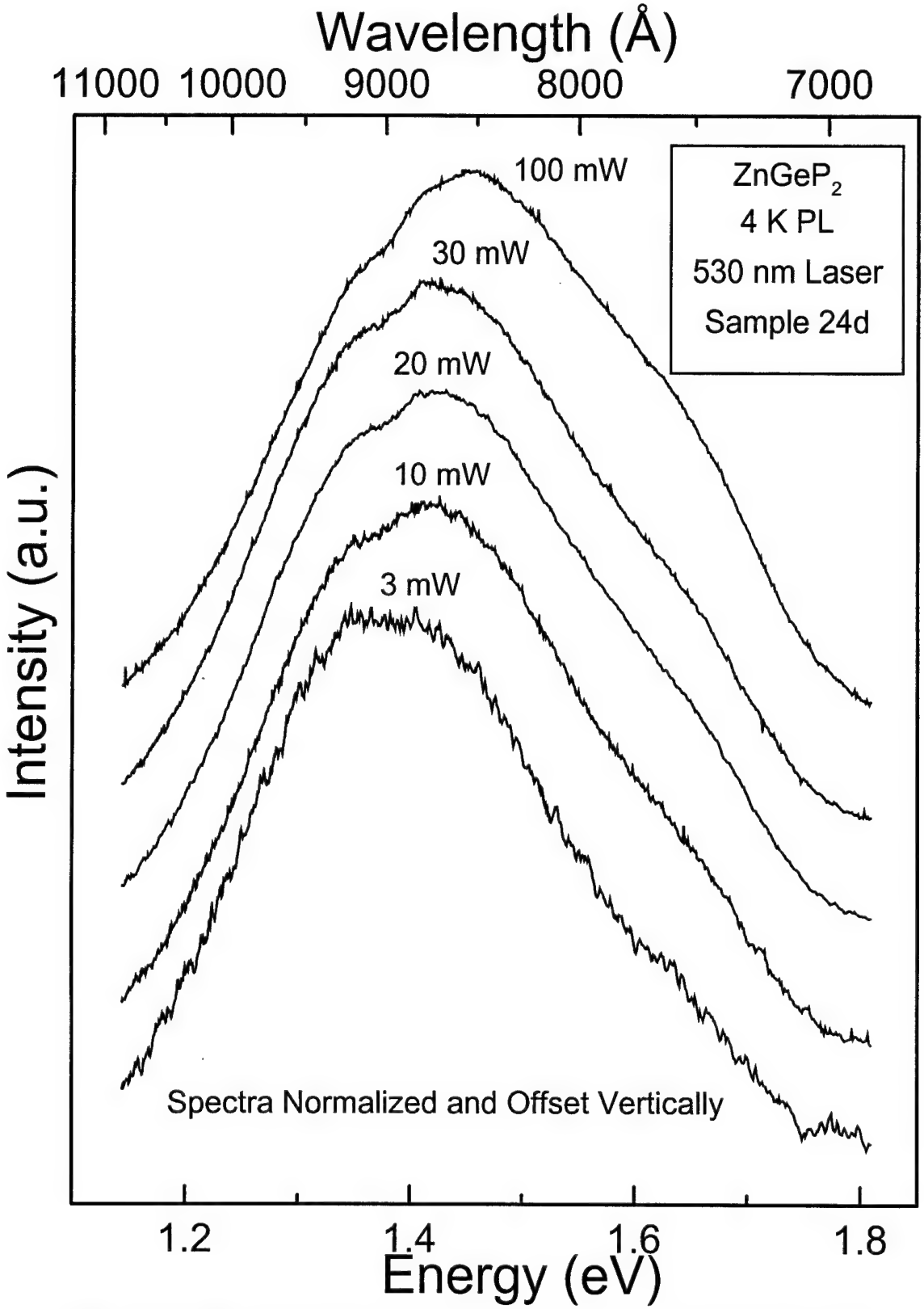

Figure 47. 530 nm Laser Power Dependence, $ZnGeP_2$, Sample 24d, Spectra Normalized and Offset Vertically.

Chapter IV. Photoreflectance.

Photoreflectance spectroscopy consists in measuring the change in the reflectivity of a sample when it is illuminated by another light source. While these changes are small, they can be readily detected under appropriate circumstances, and the data derived yields important information about the band structure of the material under study. Section 4.1 discusses the theory explaining the changes which are observed, section 4.2 discusses the equipment used for this experiment, and section 4.3 details the results achieved in this effort.

4.1. Theory

Photoreflection or photoreflectance (PR) is a useful technique for measuring the energy differences between the valence and conduction bands of a semiconductor. The reflectance depends upon the material's index of refraction, which is simply related to the material's dielectric constant. The dielectric constant will now be called the dielectric function to make explicit our concern in the variation of this function with wavelength and applied field. Knowing how the dielectric function changes in the presence of an electric field, and having a functional form for the changing part of the dielectric function, then the photoreflection signal can be modeled.

The reflectance, R, of light normally incident upon a surface is given by:[34]

$$R = \left| \frac{n - n_a}{n + n_a} \right|^2 \qquad [6]$$

Where n is the (complex) refractive index of the surface under study and n_a is the refractive index of the ambient, which can be taken to be one here. In this case the ambient will be air, vacuum, or helium gas. The refractive indices are related to the

dielectric functions, ε and ε_a, by: $n^2 = \varepsilon$ and $n_a^2 = \varepsilon_a$. Then the proportionate change in R due to a change in ε is given by:[34]

$$\frac{\Delta R}{R} = \mathrm{Re}\left[\frac{2n_a}{n(\varepsilon - \varepsilon_a)}\Delta\varepsilon\right] \qquad [7]$$

$$= \mathrm{Re}\left[(\alpha - i\beta)\Delta\varepsilon\right] \qquad [8]$$

$$= \alpha\Delta\varepsilon_r + \beta\Delta\varepsilon_i \qquad [9]$$

Where $\Delta\varepsilon = \Delta\varepsilon_r + i\Delta\varepsilon_i$ and α and β are called the Seraphin coefficients. As long as α and β are relatively constant over the region of the spectrum being studied the changes in the reflectance is nearly linear with changes in the dielectric function, ε. The actual case is often even simpler than this, for instance in the case of germanium near the band edge α is much larger than β thus $\Delta R/R$ is proportional to $\Delta\varepsilon_r$; this is also true of GaAs.[29]

Ideally the laser beam induces changes in the dielectric function by creating carriers which screen the field created by the depletion layer at the surface of the semiconductor. Thus the chopped laser beam modulates the conduction and valence bands at the surface of the semiconductor the same way an electric field would. In the unfortunate case that there is no depletion region at the surface, then the photo-created carriers will diffuse away from the surface, and this technique will not work.

The change in the dielectric function due to an applied field can be related to the dielectric function by the following physical arguments due to Yu and Cardona.[35] The real part of the dielectric function can be approximated, near a critical point, by :

$$\varepsilon_r - 1 = CE^{-2}\sum_k \frac{1}{E_c - E_v - E} \qquad [10]$$

Where C is a constant, the summation is over all wavevectors, k, in the first Brillouin

zone, E_c and E_v are the k dependent energies of the conduction and valence bands, and E is the energy of the photon interacting with the crystal. This equation shows how the dielectric function is built up from virtual transitions from the conduction and valence bands. The energy-time uncertainty principle shows that these transitions last for a time, τ, given by :

$$\tau = \frac{\hbar}{E_c - E_v - E} \qquad [11]$$

In the presence of an electric field, **E**, an electron emitted from a state in valence band, E_v, to a virtual state of the conduction band, E_c-E, will travel a distance, z, in time, τ, given by:

$$z = -\frac{e}{2}\frac{\mathcal{E}}{m_c}\tau^2 = -\frac{1}{2}\frac{e\mathbf{E}}{m_c}\frac{\hbar^2}{\left(E_c - E_v - E\right)^2} \qquad [12]$$

In travelling this distance the electron gains $e\mathbf{E}z$ in energy, or from the point of view of the electron, the conduction band state, E_c, moves this far with respect to it. Thus the electric field induces an apparent shift in the conduction band given by:

$$\Delta E_c = -\frac{e^2\mathcal{E}^2}{2m_c}\frac{\hbar^2}{\left(E_c - E_v - E\right)^2} \qquad [13]$$

These same arguments apply to a hole emitted from the conduction band into a state in the valence band, creating a shift in the valence band given by:

$$\Delta E_v = \frac{e^2\mathcal{E}^2}{2m_v}\frac{\hbar^2}{\left(E_c - E_v - E\right)^2} \qquad [14]$$

Fig. 48 shows graphically these virtual transitions which account for the dielectric function and field induced changes to it. The equations above for ΔE_c and ΔE_v can easily be combined into one where the shift is now the field induced change to the bandgap:

$$\Delta(E_c - E_v) = \frac{e^2\mathbf{E}^2}{2\mu}\frac{\hbar^2}{(E_c - E_v - E)^2} \qquad [15]$$

where μ is the reduced mass of the electron and hole. Now taking the derivative of the original expression for ε_r with respect to E_c-E_v:

$$\Delta\varepsilon_r = \frac{d\varepsilon_r}{d(E_c - E_v)} \cdot \Delta(E_c - E_v) = -C\frac{e^2\mathbf{E}^2}{2\mu E^2}\sum_k \frac{1}{(E_c - E_v - E)^4}$$

$$= \frac{\hbar^2 e^2 \mathcal{E}^2}{12\mu E^2}\frac{\partial^3 E^2 \varepsilon_r}{\partial E^3} = \frac{1}{6E^2}\Theta^3\frac{\partial^3 E^2 \varepsilon_r}{\partial E^3} \qquad [16]$$

where Θ is called the electro-optic energy. These arguments hold similarly for ε_i, so the field induced change in ε is given by:

$$\Delta\varepsilon = \frac{1}{6E^2}\Theta^3\frac{\partial^3 E^2 \varepsilon}{\partial E^3} \qquad [17]$$

A more rigorous derivation given by Aspnes[34] results in a value exactly twice this large. These results derived above apply to reflectance modulation seen in the limit of low field strength. This limit can be presumed to be satisfied when $|\Delta R/R| \leq 10^{-3}$, a requirement which was always satisfied with the experiments conducted here.

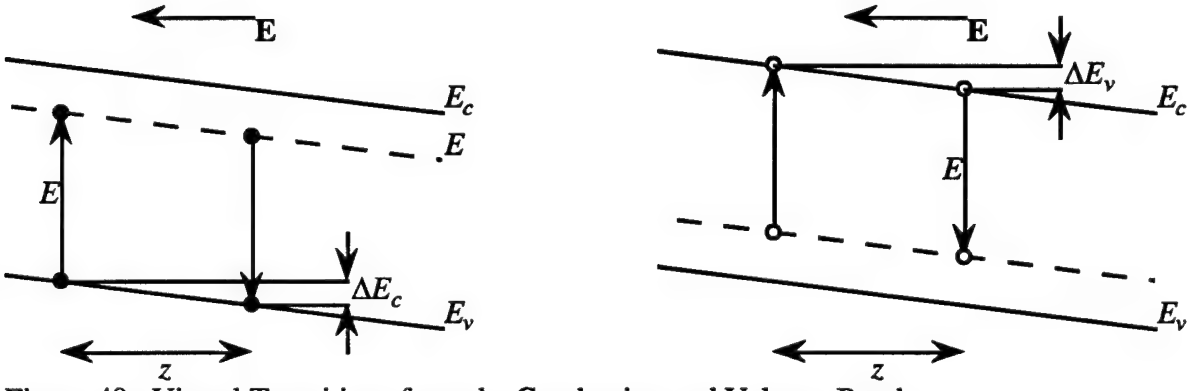

Figure 48. Virtual Transitions from the Conduction and Valence Bands.

Now it only remains to give a functional form to ε in order to predict the photoreflectance lineshapes which will be realized. The contribution to the dielectric function due to a critical point is the only part of the dielectric function which will be strongly varying at energies near this critical point, and since our lineshape will be proportional to the third derivative of the dielectric function, only this part will contribute to the PR signal. This term can be written as:[34]

$$\varepsilon(E,\Gamma) = A\Gamma^{-n} e^{i\theta}\left(E - E_g + i\Gamma\right)^n \qquad [18]$$

Where ε is this changing part of the dielectric function, E is the photon energy as before, Γ is the broadening energy, A is the overall amplitude, n is related to the dimensionality of the critical point, θ is called the phase projection, and E_g is the energy spacing between the conduction and valence bands being considered. The broadening energy, Γ, provides the lineshape with a finite width. Eq. 10 appears to be singular at resonance, that is if $E = E_c$-E_v, the contribution to ε_r becomes infinite. In actuality this doesn't happen, one simple reason that the contribution stays finite is that the virtual transition involved only lasts for a finite length of time. Even though Eq. 11 indicates that, τ, the duration of the virtual transition should increase without bound as E approaches E_c-E_v this virtual transition's longevity must be bounded by the upper state's actual lifetime. Adding $i\Gamma$ to the denominator of Eq. 10 would correct this deficiency, but it would only complicate the development of Eq. 17, however, now this term is needed in Eq. 18 in order to analyze the measured lineshapes. Factoring in Γ^{-n} as well leaves the amplitude at E=E_g set only by A. The phase projection, θ, deserves some more discussion as well. The phase projection depends not only upon the type of critical point involved and the type of spectrum being measured, but also upon the uniformity of the modulation applied. For PR even if the illumination is uniform, there is no guarantee that the induced field in the sample will be so, in fact the electric field can be expected to decrease exponentially from the surface of the sample inward. Furthermore, the depletion depth varies with

temperature, so the field and the field uniformity can both be expected to vary as the temperature changes. For these reasons θ will be left as a free parameter when fitting lineshapes. The exponent, n, is related to the dimensionality of the critical point: for 3 dimensions $n = 1/2$ and $\varepsilon(E,\Gamma)$ takes on the familiar parabolic form seen for the density of states near a 3D critical point. Other cases are $n = -1/2$ for 1D, $n = 0$ for 2D (where a logarithm would be used in practice), and $n = -1$ for excitons. Taking a derivative of $\varepsilon(E,\Gamma)$ with respect to E (or E_g or Γ) then reduces n by one. Having taken this derivative, the extra $-n$ resulting can be absorbed into A, as can the extra $1/\Gamma$, so the functional form remains unchanged. Thus this one function serves to fit all anticipated modulation lineshapes. For PR results choosing $n = -5/2$ is appropriate for third derivative lineshapes of bulk semiconductors.

4.2. PR Equipment and Procedures.

The experimental setup for photoreflectance can be divided into four main subsystems: the liquid helium dewar and sample holder, the modulating laser and associated hardware, the tunable source, and the photodetector and data collection equipment. Each of these subsystems is described below, except the liquid helium dewar and sample holder which is the same as that used for PL as described above. Fig. 49 schematically represents the experimental layout. Finally the preparation and operating procedures for this experiment are detailed.

To modulate the surface field, the sample was floodlit with light from an above bandgap laser. In this case the 514.5 nm wavelength line from an Ion Laser Technology model 5400 air-cooled argon-ion laser was used. The laser beam was chopped at approximately 190 Hz so the reflectance modulation could be detected with a lock-in amplifier. The beam passed through a band pass filter, a periscope, a double concave lens, and a mirror before entering the sample chamber. The band pass filter allowed about 40% of the laser power through. Usually the laser was operated at about 10 mW,

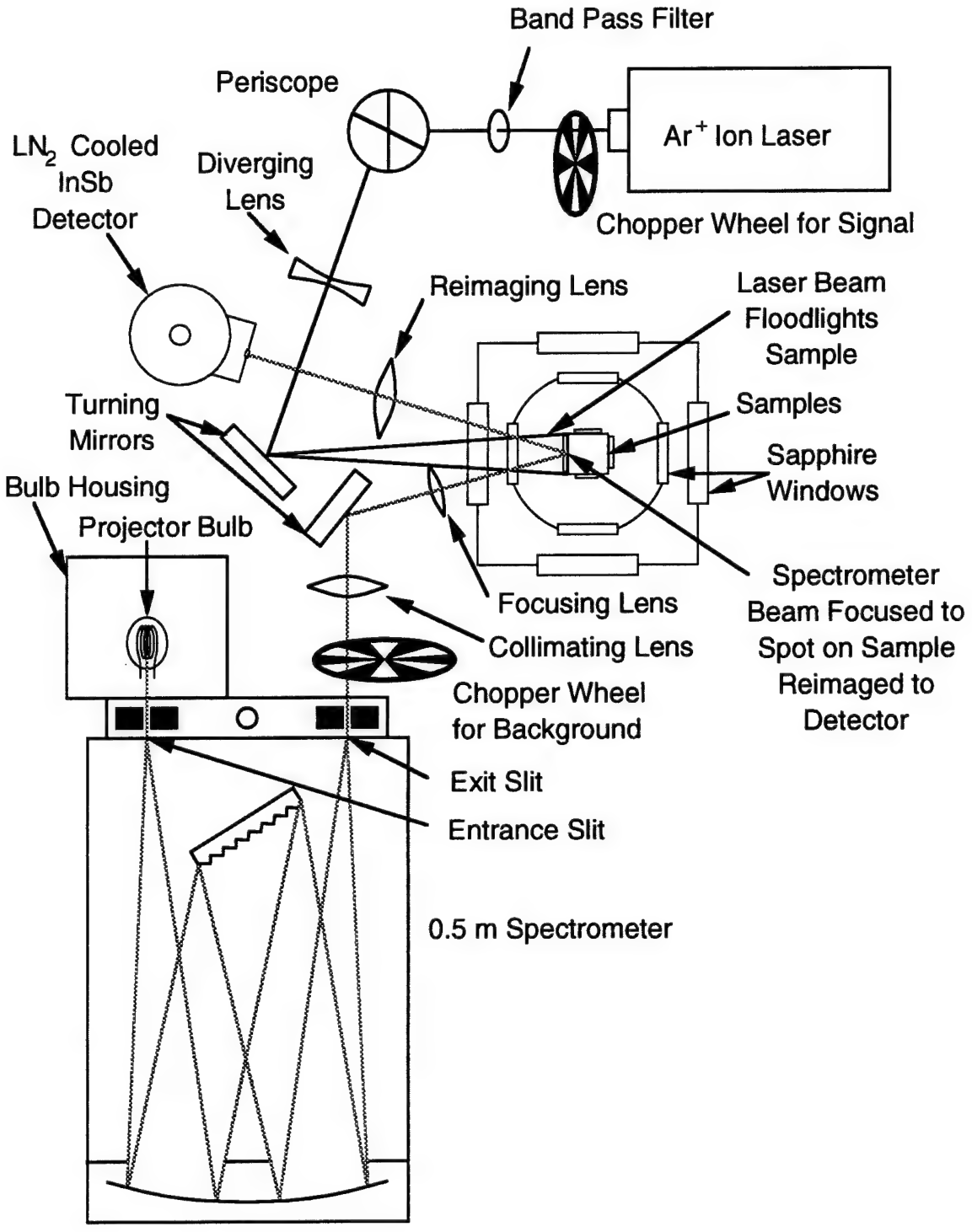

Figure 49. PR Experimental Layout

so 4 mW passed through the filter. The diverging lens expanded the beam to cover the whole sample, at the sample the beam diameter was about 1 cm, resulting in a power density on target of about 4 mW/cm^2. In some cases, especially at high temperatures where the PR signal was very weak, the laser was run at 40 mW and the band pass filter was not used. The final mirror was used to position the beam so the target sample was uniformly illuminated.

The tunable light source used for this experiment was created by passing the light from a 12 V 100 W projector bulb through a Jarrel-Ash 0.5 m monochromator. The monochromator used a 2 inch grating with 600 grooves/mm blazed for 1.5 μm. The monochromator slits were about 2mm wide, so the instrument resolution was completely determined by the instrument's dispersion of 3.3 nm/mm, thus the light used had a bandwidth of about 6.7 nm. The output from the monochromator was collimated with a glass lens, turned towards the sample chamber with a mirror, and focussed onto the sample with another glass lens. The system was arranged so the lenses projected a reduced image of the spectrometer's exit slit onto the sample. The specular reflection of this image was then reimaged onto the photodetector.

The detector was a Judson InSb photodiode operated as a photovoltaic detector. This detector had an integrated cold filter with a nominal pass band extending from 1.6 to 2.8 μm. Experimental evidence indicated that the low frequency cutoff of this filter was closer to 1.1 μm, in any event, this was sufficient to prevent any power from the laser beam (operating at 514.5 nm) from reaching the detector. While it remained possible for light passing through the monochromator in second order to reach the detector, there was little signal in first order where this light could have originated. The signal from this photodetector was boosted with a matched preamplifier, followed by a Stanford Research Systems SR850 DSP lock-in amplifier. The lock-in accumulated data and saved it to a floppy disk.

To prepare the system to take data careful alignment of the beam from the monochromator was necessary since the detector diode is very small, and since the goal was to obtain the reflectance signal from as small an area on the surface of the sample as possible. First, the monochromator was set to about 1.24 μm where the monochromator provided a visible orange beam in second order from the projector bulb. This beam was traced through the system with an index card to verify that the beam was well centered on each lens used and not being clipped by the edges of the mirror or sample chamber windows. Then an incandescent lamp was shined into the sample chamber to form a visible image of the sample on an index card placed on the face of the detector. The orange beam from the monochromator was simultaneously visible on this image, verifying that the monochromator exit slit was tightly focussed upon the sample, and also verifying that reflections from the sample chamber windows were not being directed into the detector mistakenly. The sample was floodlit with the light from the laser, so the data collected was insensitive to the exact positioning of this beam.

Data collection consisted of two runs: first a background run was taken with the laser blocked while the output from the monochromator was chopped with the lock-in phased onto this; then the chopper on the monochromator was stopped and the laser was unblocked, the lock-in was phased onto the chopped laser beam by briefly removing the band pass filter from the laser beam path. For both runs the monochromator scanned across a fixed wavelength region (usually 2.4 μm - 1.2 μm) while the lock-in logged data at a constant rate. The use and interpretation of this data is discussed in the following section on PR results.

4.3. PR Results

The PR experiment described above was carried out as a function of temperature and polarization. Before the data will be analyzed for bandgap information the individual data runs described above will be discussed. The data so generated was processed to

generate temperature dependent bandgap data. Laser power was varied to verify that the spectra measured were not strongly influenced by it. Sample to sample variation was investigated as well.

4.3.1. Raw PR Data

One typical piece of data produced by this PR experiment is given in Fig. 50, these curves represent the raw PR signal, that is they are proportional to ΔR not to $\Delta R/R$. More precisely these curves represent $I\Delta R$, where I is the spectrum of light reported by the detector due to the wavelength dependence of every element in the system, except the sample under study. I then comprises the product of the spectrum of light generated by the projector bulb and the wavelength dependence of each element in the system. These factors include the monochromator (it is most efficient near the blaze wavelength of the grating, 1.5μm), the transmissivity of the lenses and windows, an optional polarizer, and the wavelength dependent response of the detector. Because the data on Fig. 50 is proportional to $I\Delta R$ and not to $\Delta R/R$ it cannot be used for analysis of the bandgap, but several important qualitative features can be most easily seen on this figure.

The main peak on Fig. 50 is due to the material's bandgap, the second peak is due to the gap between the second valence band and the conduction band, while the third valence band lies too deep to appear on this figure (See Fig. 9). The selection rules shown on Fig. 8 are seen to be approximately satisfied. While the selection rules on Fig. 8 suggest that the second peak should not appear at all for **E**||**c**, this condition is only approximately satisfied because the monochromator beam is not quite normally incident upon the sample, and the sample's **c**-axis lies in the plane of incidence. The noise level apparent on this figure is about 0.5 μV, this will be shown to be the dominant noise source in the analysis which follows. The resulting signal-to-noise ratio (SNR) is then about 25 for the larger peak. The polarization dependent curves make it apparent that the minimum which falls between the two main peaks is being influenced by both peaks. That is these two transitions have slightly overlapping lineshapes. This overlap can only

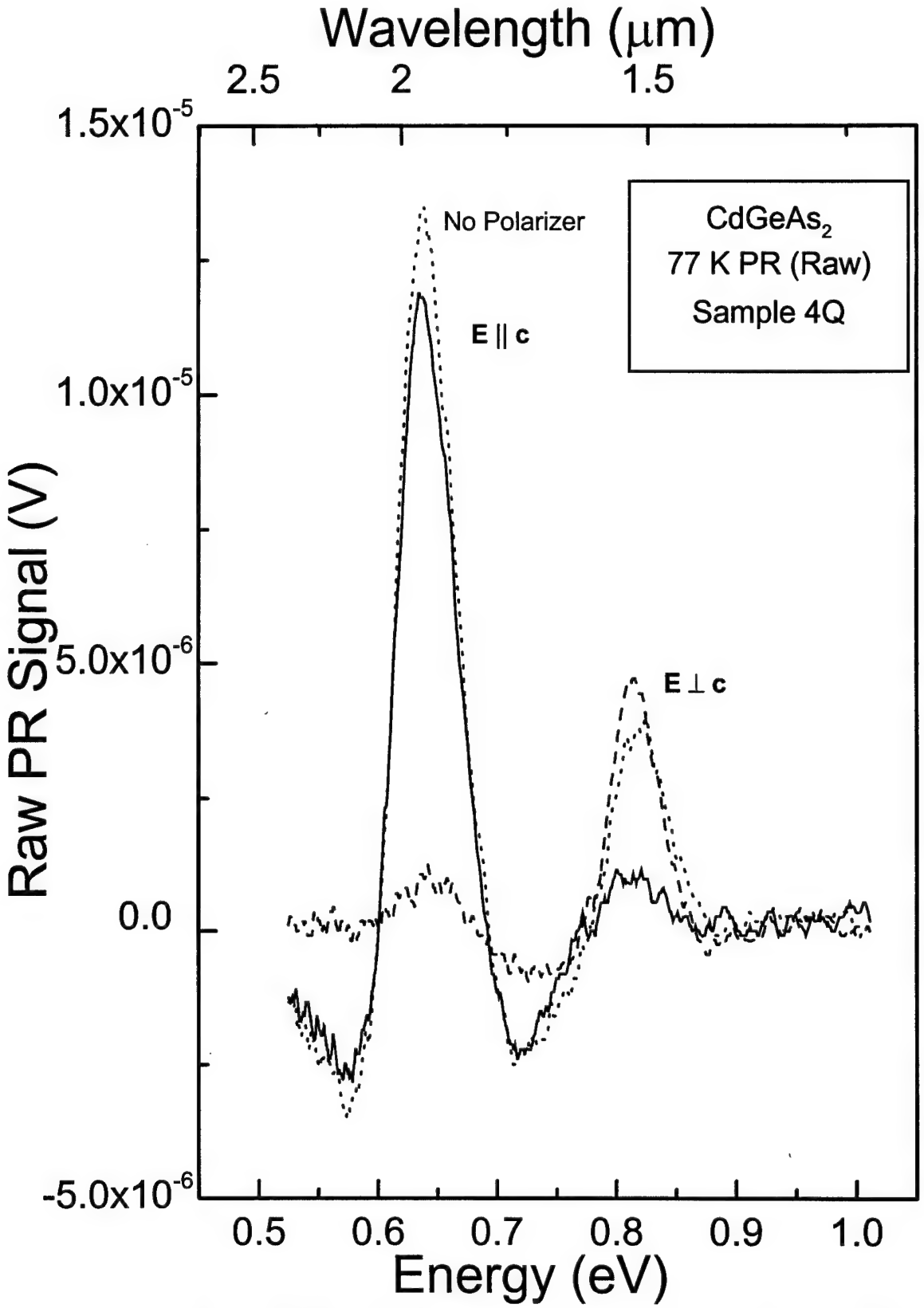

Figure 50. Polarized Raw PR Signal for $CdGeAs_2$ sample 4Q at 77 K

be expected to get worse as the temperature increases. The curve for unpolarized light is seen to follow the maximum excursion made for either polarization case, this is just what is expected since the unpolarized signal should be just the sum of the two orthogonally polarized signals.

Fig. 51 shows both the X and Y phases of the data taken by the monochromator. The X phase is in phase with the modulating laser, and the Y phase lags by 90°. These phases are independent from each other, so different information might appear on each phase. If strong data appears on the Y phase, it might be preferable to use the Y phase for data analysis since any PL coming from the sample or laser light leaking through to the detector would be out of phase and thereby cancelled out. Fig. 51 shows this to not be the case here. The Y phase data appears proportional, but much weaker, than the data which appears on the X phase. This suggests that there is a phase choice which would in fact null out the Y phase completely and maximize the signal appearing on the X phase. This phase is not quite the phase selected here, because either the phase was not set to be exactly in-phase with the modulating laser, or the PR signal is slightly out of phase with the modulating laser. Setting the phase perfectly is difficult because the laser leakage which is used to lock in on is quite small (4.5 μV with the laser at full power); setting the phase perfectly is also unimportant since the amplitude of the signal in the phase we care about is only falling like $\mathrm{Cos}(\Delta\phi)$, while the amplitude data on the phase we will ignore grows like $\mathrm{Sin}(\Delta\phi)$, where $\Delta\phi$ is the phasing error. So if the amplitude in the Y phase is 10% of that in the X phase, then misphasing has only cost 1% of the amplitude off the X phase signal. These factors seem about right for the data presented on Fig. 51. The X and Y phases discussed here do not relate to the phase projection, θ, of Eq. 18.

4.3.2. Reflectance Background Data.

Data such as that presented in Fig. 50 and Fig. 51 can not be used to estimate the bandgap or other parameters, until these curves have been divided by reflectance

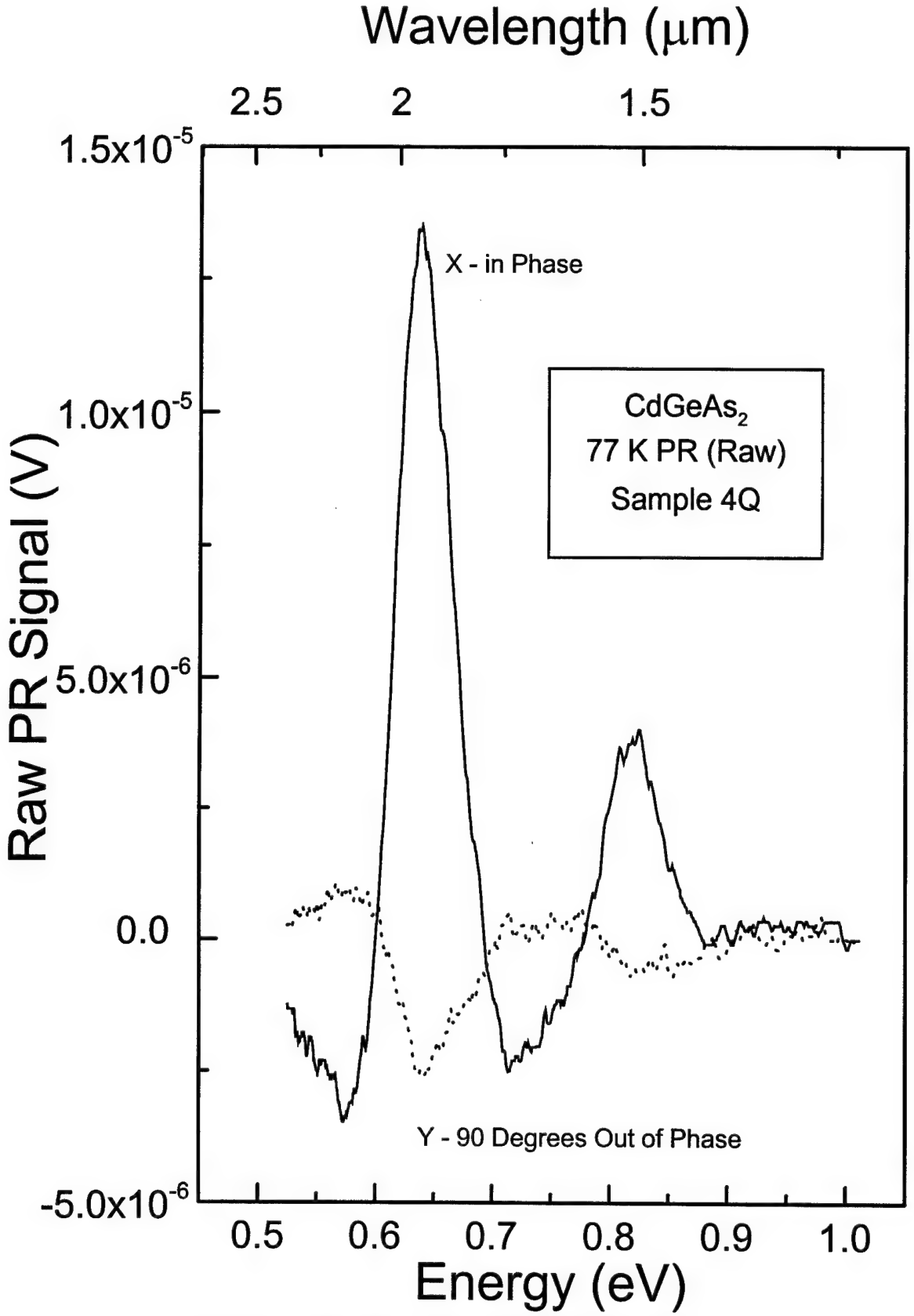

Figure 51. Raw PR at 77 K - Phase Dependence.

background data. Before advancing to spectra which have been processed in this way the denominator used for this division can be investigated. Fig. 52 shows the polarization dependence of the reflectance background. Just as the raw PR data curves represent $I\Delta R$, these curves now represent IR where R is the reflectance of the sample. Almost all of the noticeable motion seen on these curves can probably be attributed to I. R can be expected to be relatively constant over the range investigated here, Eq. 6 predicts a reflectance of 0.33 based on an index of refraction of 3.7. The strong polarization dependence seen in Fig. 52 can be attributed both to the diffraction grating in the monochromator, but also to the windows on the sample chamber. The many grooves on a diffraction grating act with a polarization preference favoring light polarized with its **E** field perpendicularly to these grooves, just as would be expected if the grooves were wires (the grating is metallized, but the coverage is continuous). While the angle of incidence is small, light does not enter or exit the sample chamber normally to the windows. Light polarized with **E** in the plane of incidence is preferentially transmitted compared to light polarized perpendicularly to the plane of incidence. Keeping the angle of incidence small minimizes this effect, but there are 8 sapphire-air interfaces encountered in passing in to and out of the sample chamber (two windows each way), so any effect present is multiplied by 8. The experimental arrangement is such that both of these effects favor light polarized with **E** horizontally, that is parallel to the floor of the room. Fig. 49 is qualitatively correct in illustrating this arrangement. Other important features of Fig. 52 are the atmospheric absorption lines seen centered about 0.66 eV and 0.9 eV, these are due to water vapor and CO_2 in the air. Neither the PR features being investigated here, nor their spacing coincide with those of these absorption lines. Additionally, these absorption lines should affect both the PR data and the reflectance background equally and therefore cancel out. When the degree of polarization of the system throughput is computed by dividing the difference between the two orthogonal polarizations shown on Fig 52. by their sum, these lines do indeed disappear. This shows these absorption lines

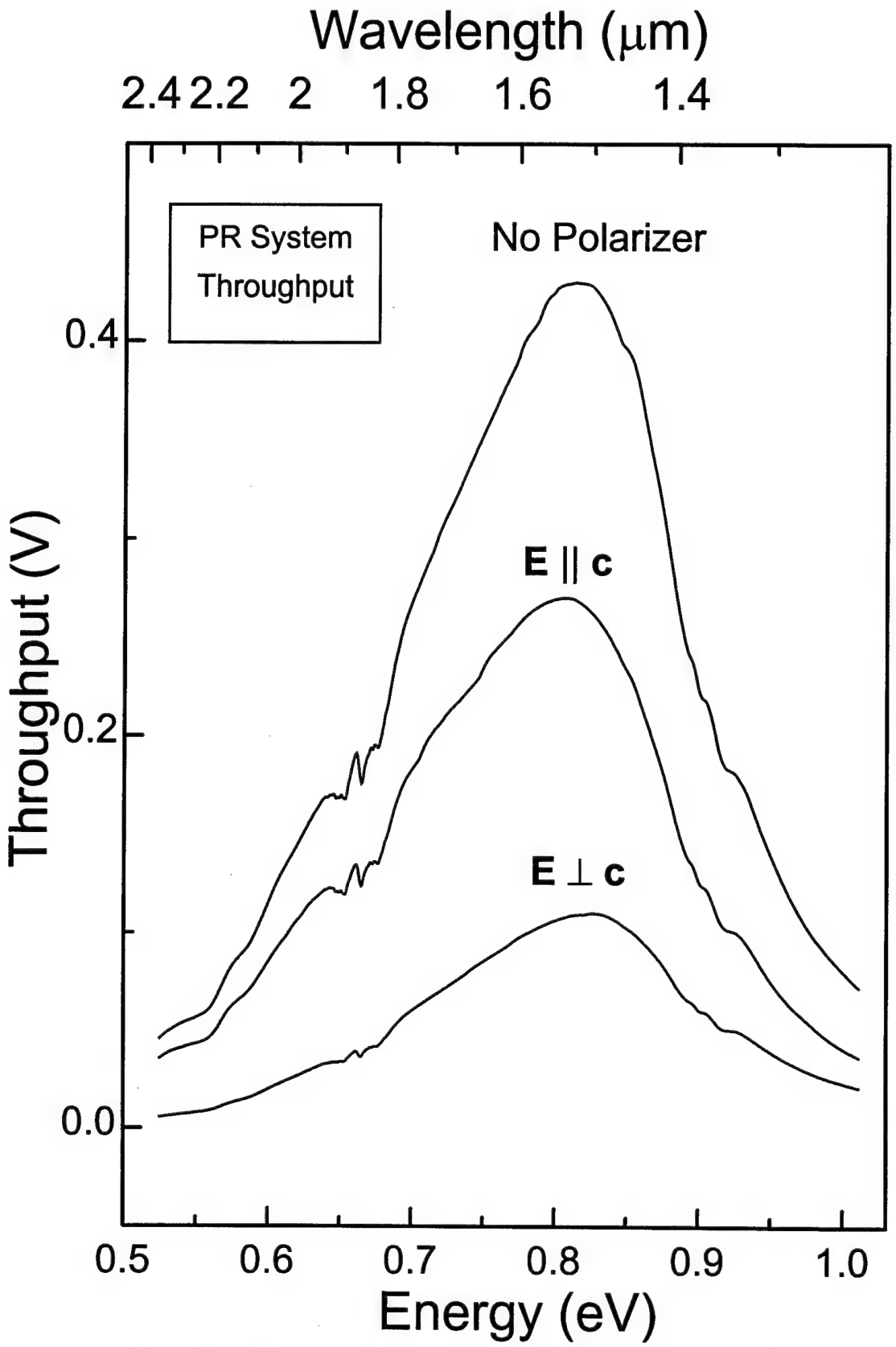

Figure 52. PR system throughput and polarization dependence

to be unpolarized, and thereby provides another way to identify any interference they might cause. Nothing on these curves looks like noise, such as the noise apparent on Fig. 50. Using the data which makes up Fig. 52 at the start of the vertical polarization curve (0.525 eV), the throughput takes on a value of 5.615 mV. Using a much finer scale to look for noise in this data reveals that the lock-in's quantization noise is the first noticeable noise source. The least significant bit (LSB) on this scale is worth 30 μV, so the SNR due to this source is then 374 (SNR = 5.615/(1/2 LSB)), this represents the worst case. As the signal strengthens, the quantization noise is unaffected and the SNR grows even larger. This noise source will be seen to be insignificant.

4.3.3. Polarization Resolved PR.

Dividing the data on Fig. 50, which represent $I\Delta R$, by those corresponding curves on Fig. 52, representing IR, cancels out the system dependence carried in I, and yields the desired PR data, $\Delta R/R$. These curves are displayed on Fig. 53. $\Delta R/R$ is dimensionless, so the data presented on these curves has an absolute scale, and may be compared directly to results achieved elsewhere. The requirement that $\Delta R/R$ be less that 10^{-3} for the low field limit to apply is seen to be well satisfied.

The unpolarized case and the case polarized with **E**||**c** are seen to be very similar, this happens because the light passing through the system has the strong polarization preference shown on Fig. 52. The second PR peak is responding mostly to light polarized with **E**⊥**c**, but on the unpolarized curve it is divided by not only **E**⊥**c**, but also the much stronger **E**||**c** which it does not respond to. The experimental arrangement is thus seen to give good data for **E**||**c** with or without a polarizer, but transitions with strong selection rules favoring **E**⊥**c** can only be exhibited through the use of a polarizer (or by rotating the crystal to interchange the system's bias).

The high noise seen at the lowest energies on the **E**⊥**c** curve on Fig. 53 is due to the very small amount of throughput with this polarization over this region. This is not a

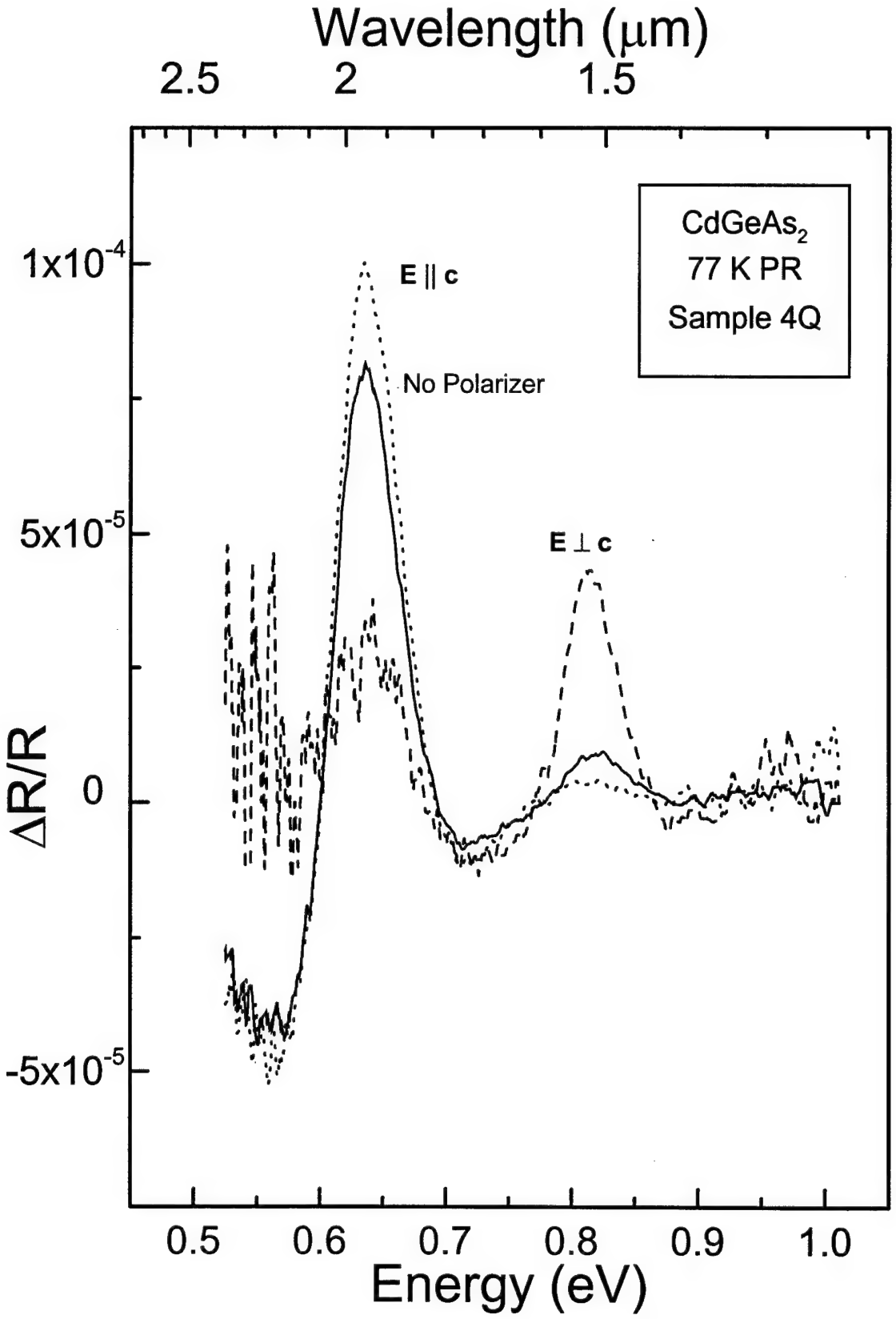

Figure 53. Polarized photoreflectance spectrum for $CdGeAs_2$ sample 4Q at 77 K

problem because this particular curve would only be used for analysis of the peak near 0.82 eV, where the noise has improved substantially. This curve for **E⊥c** is expected to be a weaker (and noisier) copy of the **E||c** curve over the first lineshape; most of its failure to do so can be easily explained. The fact that this curve is largely positive at the lowest energies, while the **E||c** curve is negative implies that a small amount of light from the laser was reaching the detector in some way. In this case, instead of $I\Delta R$, the raw data consists of $I\Delta R$ + leakage, so the $\Delta R/R$ curve becomes $\Delta R/R$ + leakage/(IR). In cases where the signal is weak, this leakage must be estimated and subtracted away before the division is accomplished. If this is not done, this leakage/(IR) term imprints the inverse of the throughput curve onto the $\Delta R/R$ curve, which results in the $\Delta R/R$ curve rising up at both extremes of the wavelength range making this problem easy to identify. In the case of the **E⊥c** curve under discussion here, this leakage is comparable to, but still smaller than the amount of noise present. This means that for the **E||c** curve errors due to this leakage should also be smaller than the noise present, making this effect ignorable in this case.

The $\Delta R/R$ curves were formed by dividing two data sets, the noise present on the $\Delta R/R$ curve is then a function of the noise found in each of these data sets. To track noise though a function of two variables we can use:

$$\sigma_f^2 = \left(\frac{\partial f}{\partial x}\right)^2 \sigma_x^2 + \left(\frac{\partial f}{\partial y}\right)^2 \sigma_y^2 \qquad [19]$$

Where f is a function of x and y, σ_f is the uncertainty associated with f, and σ_x and σ_y are the uncertainties associated with x and y respectively. This equation presumes that the noise associated with x and y is uncorellated. For the case here, where $f = x/y$, it is easy to show that the SNR's of x and y add in inverse quadrature. That is:

$$SNR_f^{-2} = SNR_x^{-2} + SNR_y^{-2} \qquad [20]$$

For the data used to create Fig. 53, the SNR associated with $I\Delta R$ was shown to be 25 at best, while the SNR associated with IR was seen to be 374 as a worst case. The resulting SNR for the $\Delta R/R$ curve is then 24.9. The SNR, considering the signal to be the height of the main peak, is then seen to be almost completely dominated by the noise in $I\Delta R$, as previously stated.

Eq. 1 predicts a ratio of about 12:1 for the relative strengths of the **E**||**c** and **E**⊥**c** transitions at the band edge. The **E**⊥**c** case is so noisy that it is difficult to be sure of the strength of this transition, but the amplitude from bottom of the first trough to the top of the first peak can be estimated to be between 2.5×10^{-5} and maybe only half of this. The amplitude for the **E**||**c** case is easily estimated to be 12.5×10^{-5}. These values suggest a polarization ratio of 5:1 to 10:1. This is reasonably good agreement with the 12:1 ratio predicted, considering the noisiness of the data, and is also in good agreement with what was measured by PL.

This data was collected at 77 K, which proves to be nearly an optimum temperature for this work, since at higher temperatures the signal becomes much weaker, and lowering the temperature further does not improve the signal any further, while lower temperatures do result in a significant amount of PL being generated and picked up by the detector.

4.3.4. Fitting to the PR lineshape.

In order to use PR to estimate the bandgap a lineshape function is fit to the data. An example of this fit is given on Fig. 54, which shows the unpolarized 77 K $\Delta R/R$ data from Fig. 53, along with the fitting function determined for this case. The function used consists of the sum of the real parts of two of the lineshape functions given in

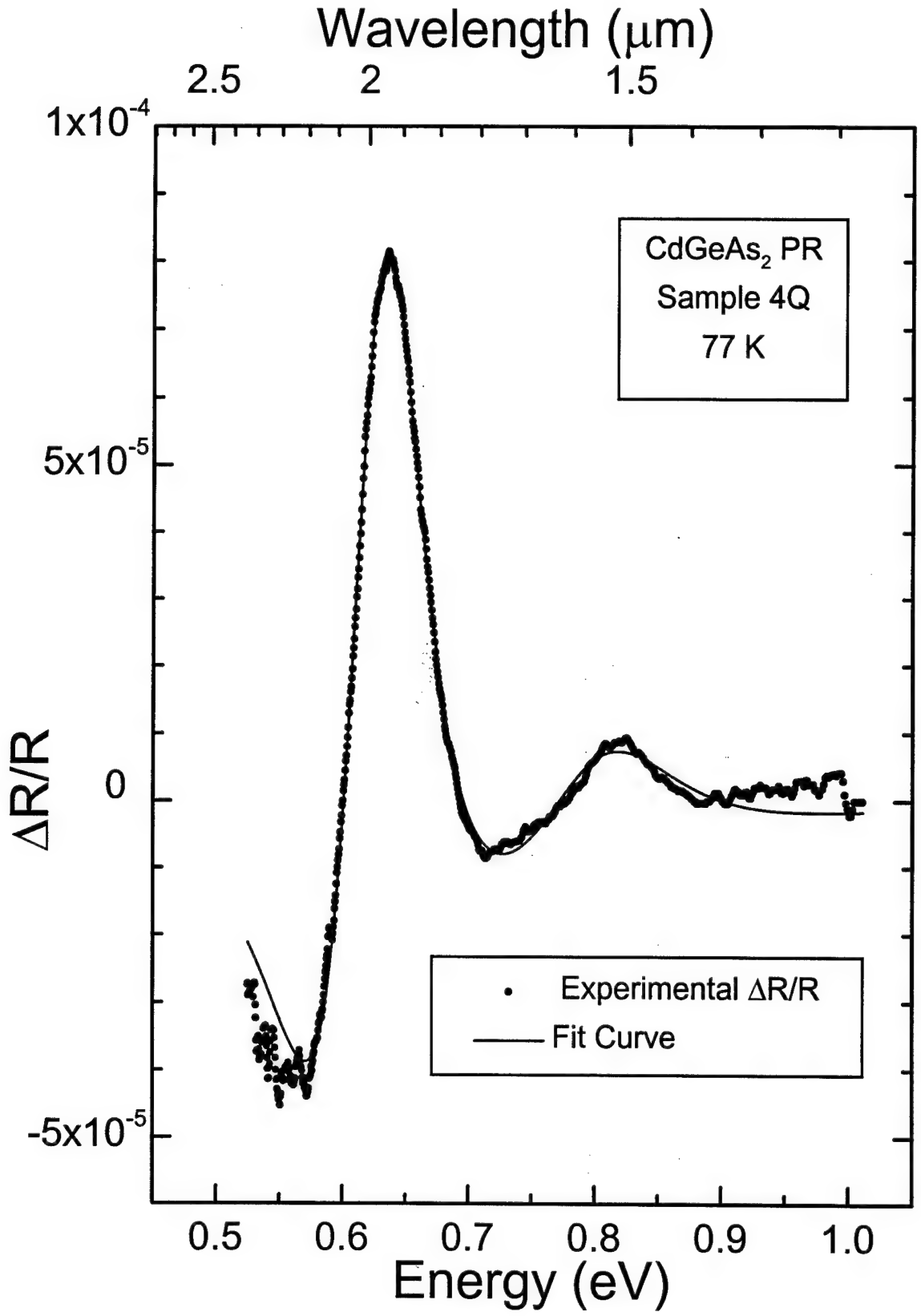

Figure 54. 77 K PR results with fit curve for $CdGeAs_2$ sample 4Q

Eq. 18. The fit was accomplished with a non-linear least-squares fitting routine based upon the Levenberg-Marquardt algorithm.[32] The program required the data being fit to along with error estimates, the function to be fit to this data, the derivatives of this function with respect to each of the parameters being sought, and a starting guess for each of parameters. The output from the program included least-squares sense optimized values for each parameter, and error bounds for these values. Table 2 shows the parameters determined (the exponent, n, was fixed at 5/2). Two lineshape functions were used, since two different transitions were seen to be involved (labelled v1 and v2 in Table 2). The error was estimated to be 0.5 μV/IR, so the noisier portions of the curve were appropriately less heavily weighted. The bandgap was estimated to be 0.6218 ± 0.0004 eV (at 77 K); while this uncertainty is tiny, it only pertains to this particular data set. Changing this estimate of E_g would shift the first lineshape on the fit curve in energy, and it is clear from Fig. 54 that this would worsen the fit quite quickly. On the other hand, the broadening parameter, Γ, could be taken as a measure of the spread in bandgap values encountered, especially to the extent to which it exceeds kT. That is while a reasonably broad range of values may be present, their mean is very well determined.

Table 2. Lineshape Parameters for Fig. 54 (77 K PR).

	v1	v2
A	9.14×10^{-5}	1.18×10^{-5}
E_g (eV)	0.622	0.791
Γ (eV)	0.0633	0.114
n	5/2	5/2
θ (Rad)	3.19	3.21

The fit curve on Fig. 54 matches the data well, but not perfectly. Since the fitting function depends nonlinearly on most of the fit parameters, the fit found by the computer program is the not necessarily the true best fit, in fact there is no guarantee of uniqueness for the true best fit. None the less, the fit of Fig. 54 is believed to be effectively the best fit possible for the fitting function used, because convergence to this solution is quick for a wide range of initial guesses, and deviations between the fit and the data can be explained in terms of effects that the fit could not address. At the high end of the energy scale (0.9-1.0 eV) the fit falls mostly below the data, the rise in the data is probably due to a small background level in the raw modulation data. The fit curve has no lineshape function in this region, therefore the fit here cannot be improved without moving one of the lineshape functions towards this region, which would make things much worse elsewhere. At the low energy limit, the fit climbs above the data. In this case we have one maximum, and two minimums which need to be accounted for by the first lineshape function, but only two parameters, A and θ, affect these heights independently. So the fit here cannot be improved without making things worse elsewhere again. While the second minimum is actually influenced by both lineshape functions about equally, some trade-offs could be made here, but still there are insufficient degrees of freedom to expect the fit to be improvable. That the fit is so good given these constraints lends further support to the applicability of the model chosen.

4.3.5. Temperature dependence of the PR.

The PR measurement and fitting procedure described above was carried out across a wide range of temperatures. Fig. 55 shows the results achieved at 5 K. At this low temperature a significant amount of PL is generated by the laser used to modulate the surface field, this leakage, estimated to be 3.5 μV, was subtracted away from the raw modulation data before it was divided by the reflectance background. As the temperature increases above 77 K the PR signal quickly diminishes in strength. Increasing the

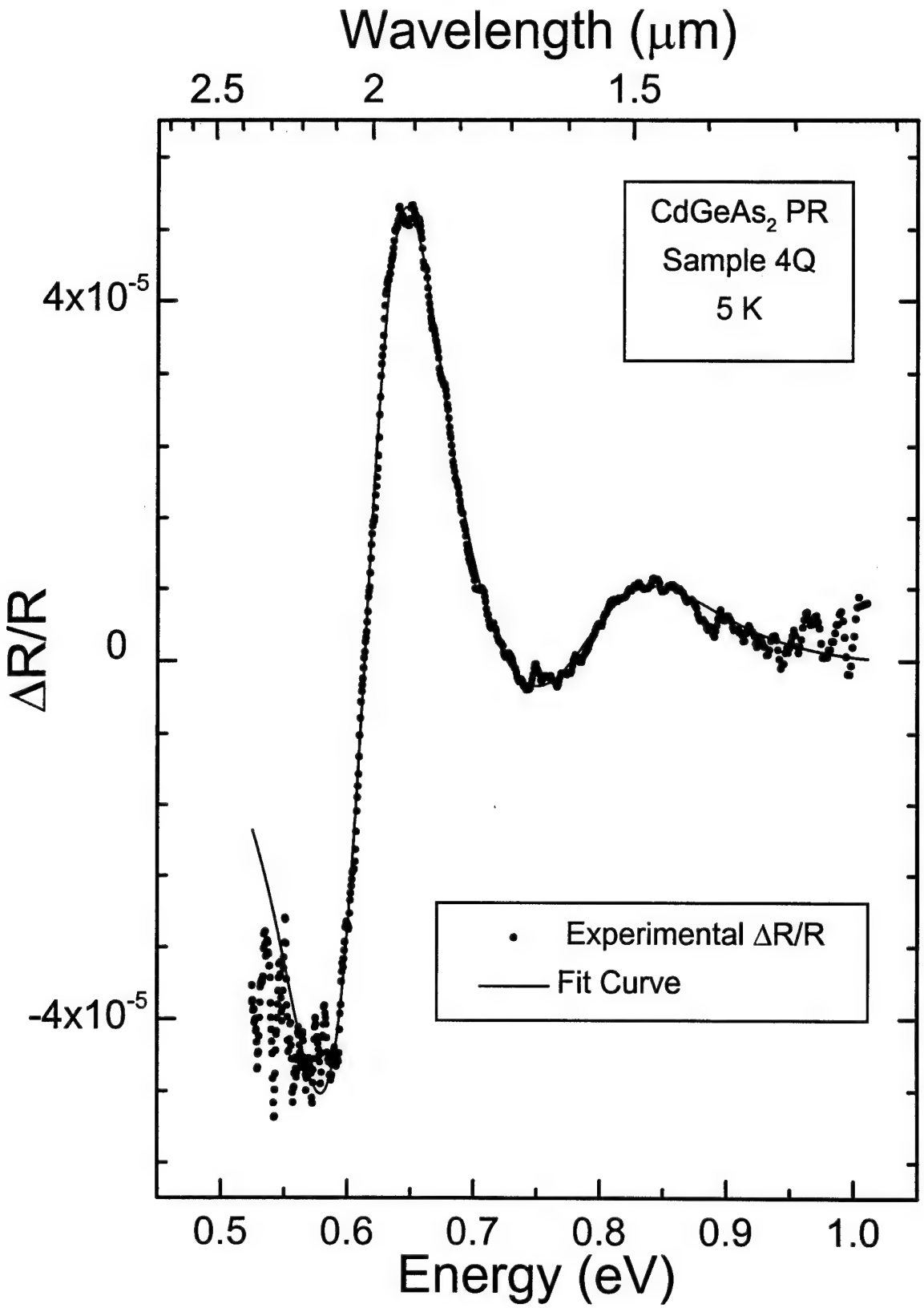

Figure 55. 5 K PR results with fit curve for $CdGeAs_2$ sample 4Q

lock-in's time constant and scanning more slowly helps to maintain the SNR to a point, but by room temperature the signal has virtually disappeared. Fig. 56 shows the results achieved at 250 K. In this case the lock-in time constant was increased from 3 to 10 seconds, presumably reducing the noise by a factor of $\sqrt{10/3} \approx 1.83$, but the signal strength has fallen by more than an order of magnitude. This noise reduction does make a background level of 0.4 μV quite noticeable on the raw modulation data, this value was subtracted off in processing this data.

At room temperature the signal is weaker still. Lengthening the time constant further to achieve acceptable signal quality has become impractical at this point, so a number of steps were taken to improve the SNR. The sample was remounted in a different chamber to reduce reflection losses and allow tighter focussing of the monochromator beam on the sample. The laser was operated at its maximum power level (30-35 mW), and the band pass filter was not used. While the PR signal is only expected to increase sublinearly with laser power any possible improvement in signal was sought. These steps alone were insufficient, so 17 consecutive data runs were collected and averaged together. Fig. 57 shows one data run (the first), along with the average of these 17 runs. Raw modulation data was selected for presentation here to simplify the behavior of the noise. Features due to transitions from the conduction band to each of the first two valence bands are distinguishable even on the unaveraged curve, although just barely since the signal and noise are comparable in strength. The PR features sought are quite clear on the averaged data. The noise that remains after averaging is estimated to be 0.05 μV. Subtracting the background of 4.5 μV seen on Fig. 57 from the averaged data and dividing by the reflectance background generates the data presented on Fig. 58. Also presented on this figure is the lineshape fit through this data. At the low energy end of the spectrum the data is very noisy, but it does appear that the fit curve represents the trend present. The fitting routine makes use of the data even here. Since this fitting

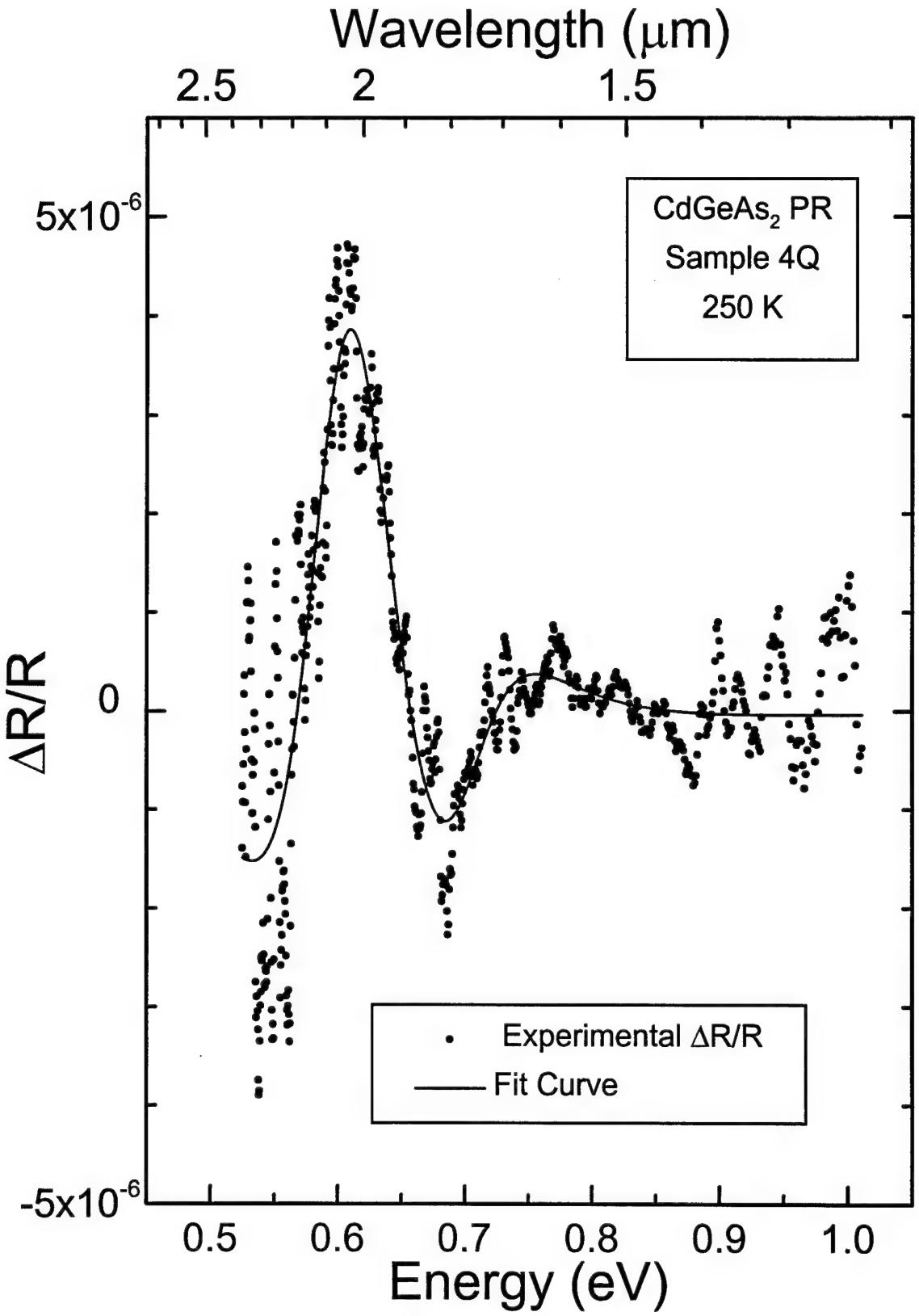

Figure 56. 250 K PR results with fit curve for $CdGeAs_2$ sample 4Q

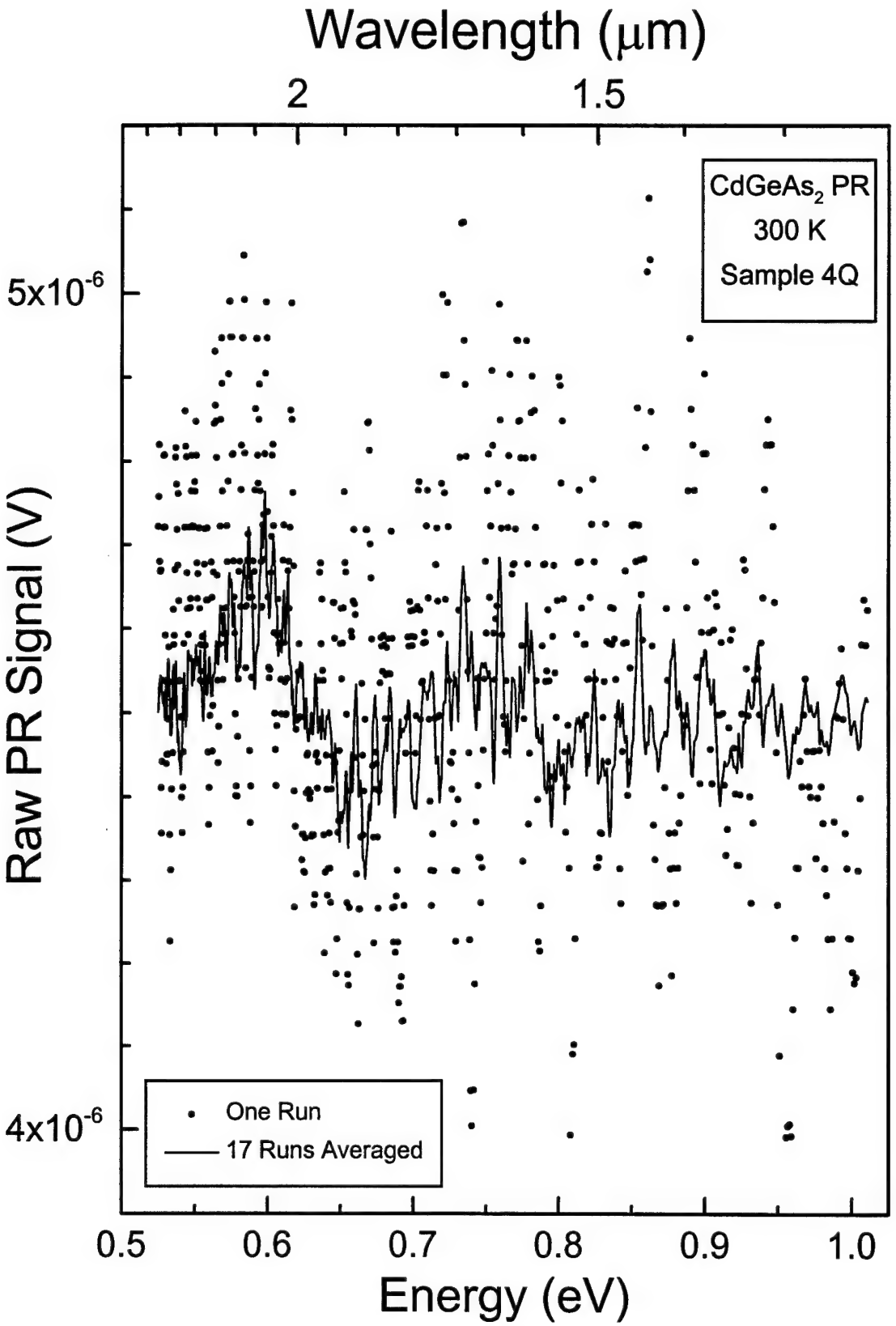

Figure 57. 300 K raw PR signal, single run and average of 17 runs

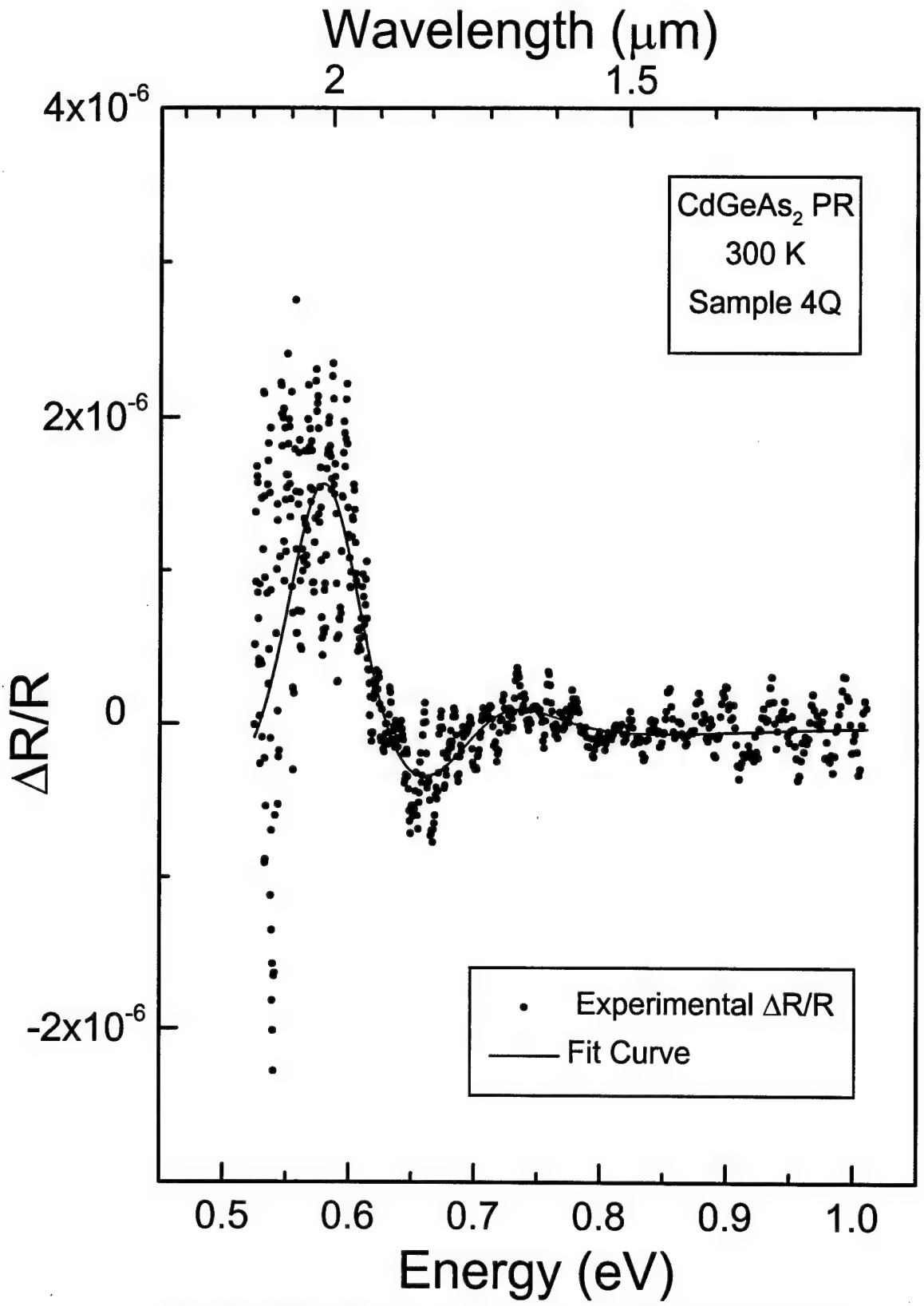

Figure 58. 300 K PR results with fit curve for CdGeAs2 sample 4Q

technique uses all the data provided to estimate just a few parameters, it can be thought of as another form of averaging.

The value of amplitude fit parameter, A, for the first lineshape function is shown on Fig. 59 as a function of temperature. The rapid decay of the strength of the PR signal with increasing temperature is clearly seen. The last data point (at 300 K) cannot be compared directly to the others, since the 300 K data was obtained by the somewhat different means described above.

The bandgap values from the lineshape fits discussed above, plus several additional values from data taken at other temperatures are plotted on Fig. 60. Included with this data is the location of the PR peak based upon each of these sets of fitted parameters. Also shown is the fit of a Varshni-type expression[36] to the bandgap values given. This fit does not take the error bounds for the bandgap values into account. These error bounds were discounted because the small error values given by the PR fitting program at low temperatures dominated an attempted fit, resulting in poor behavior at higher temperatures. These error bounds were also discounted because they appear unrealistically small given the spread of data points present. Even with this attempt to improve the fit to the bandgap curve, the result is still not very satisfactory. The equation fit to the data is:

$$E_g(T) = E_{g0} - \frac{\alpha T^2}{\beta + T} \qquad [21]$$

Where the fit determines the parameters E_{g0}, α and β. E_{g0} is the bandgap at T = 0 K. The parameters α and β are best described phenomenologically. The value of α sets the curvature of the bandgap curve at low temperatures, β is the temperature where the curve transitions from quadratic to linear behavior, and $-\alpha/\beta$ is the high temperature limit of the

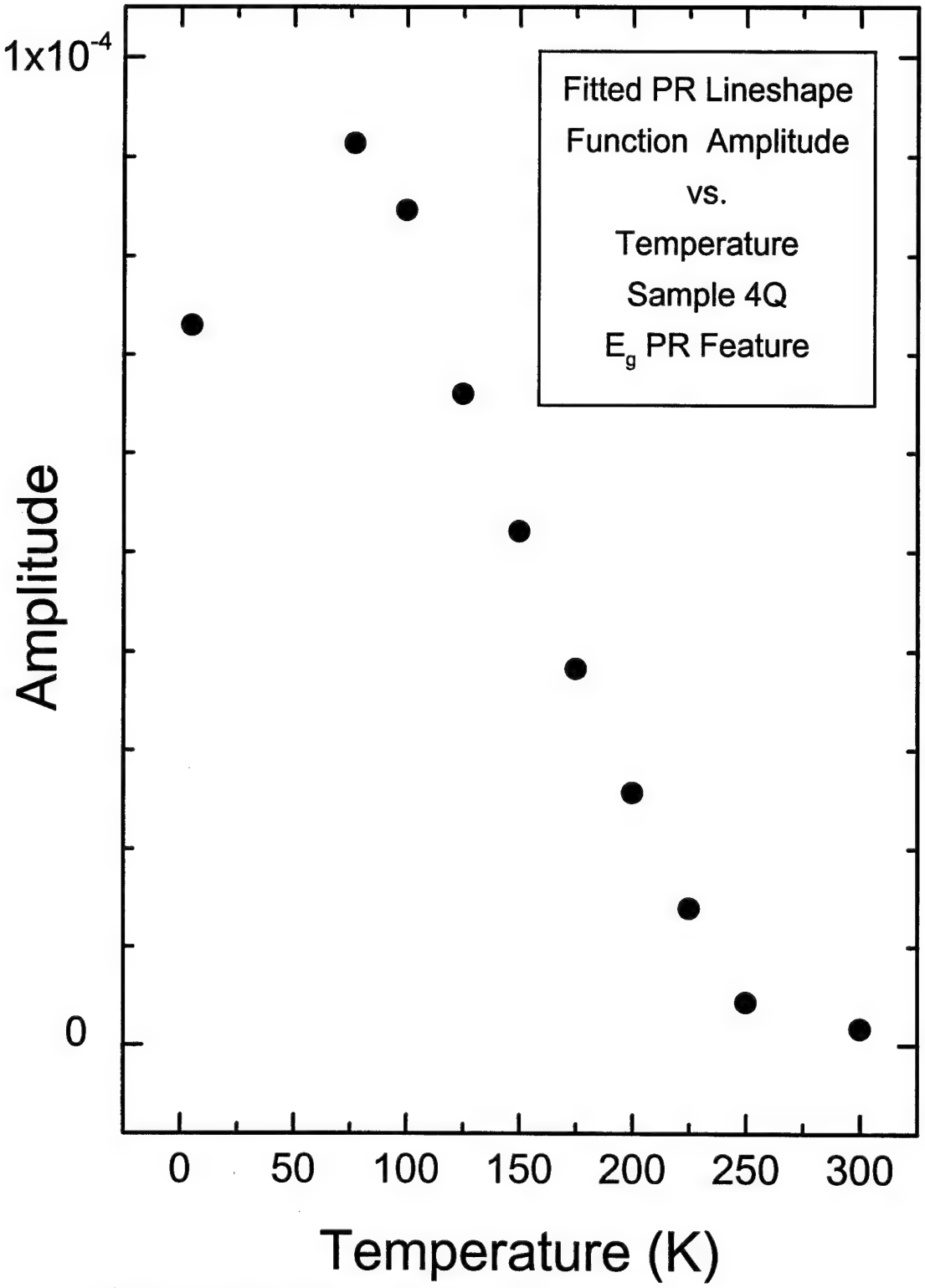

Figure 59. PR Lineshape Amplitude vs Temperature

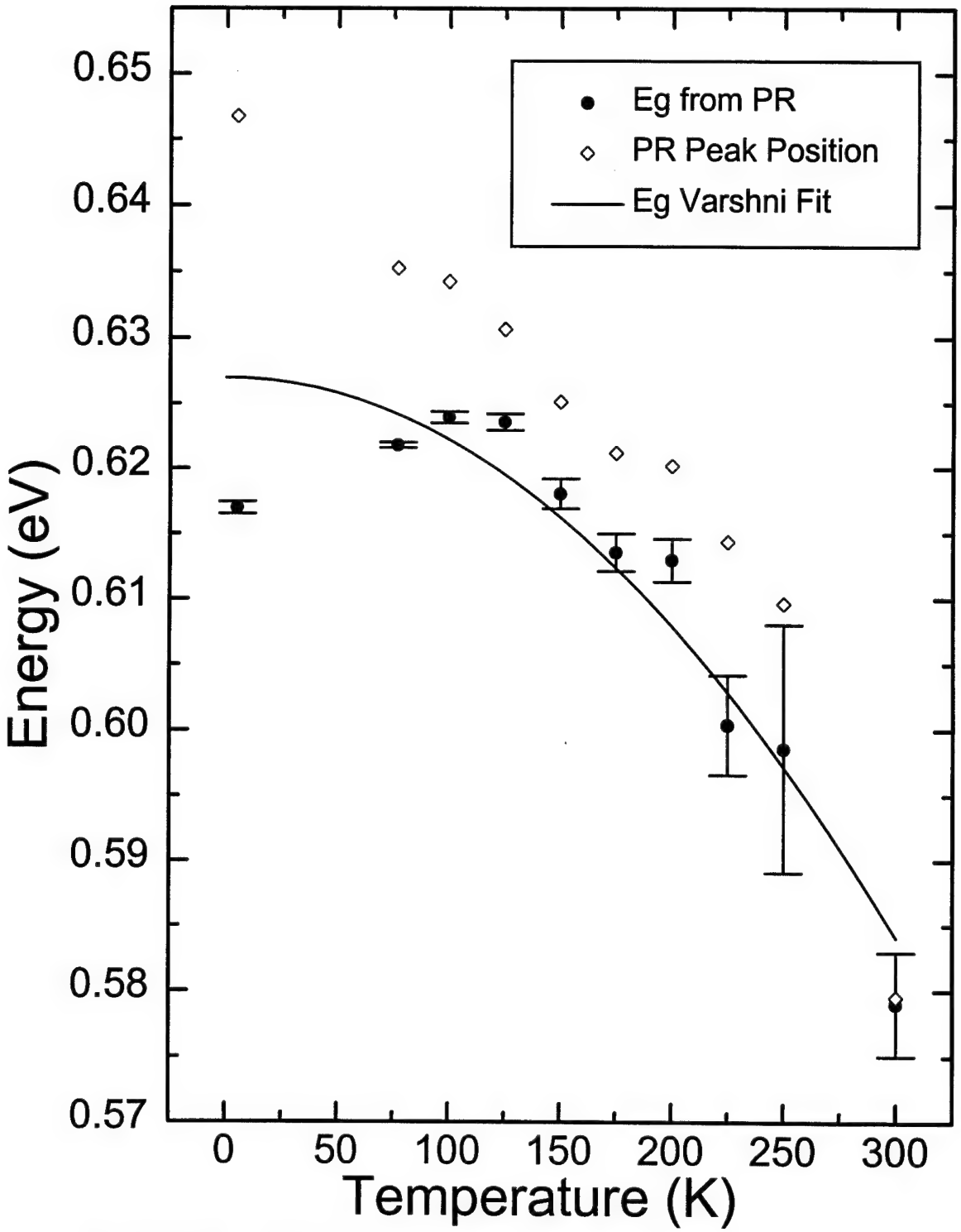

Figure 60. E_g from PR and PR peak position, plus Varshni fit to E_g, disregarding error bars.

slope of the curve. The fit actually determined results in very large values for β, making the curve quadratic for all practical purposes. This fit curve is then given by:

$$E_g(T) = 0.627 - 4.77 \times 10^{-7} T^2 \qquad [22]$$

Where T is in Kelvins and $E_g(T)$ is given in electron-volts. The PR peak position data is included as well because bandgap values reported for $CdGeAs_2$ have been based upon the peak in the modulation spectrum as measured by electroreflectance.[7,9] Unless the phase projection chosen by the fitting routine has moved in the wrong direction, with respect to a symmetric lineshape, the PR peak position forms a reasonable upper bound for the bandgaps measured here as well.

Chapter V. Hall Effect on $CdGeAs_2$.

5.1. Hall Effect Theory.

A carrier of charge q moving through a (semi-) conductor with velocity, **v**, in the presence of both an electric field, **E**, and a magnetic field, **B**, is subjected to the Lorentz force, **F**, given by (in cgs units):

$$\mathbf{F} = q(\mathbf{E} + \frac{\mathbf{v}}{c} \times \mathbf{B}) \qquad [23]$$

Where c is the speed of light. If current is passing through a material perpendicularly to an applied magnetic field, the charge carriers will be bent from their previous courses by the magnetic field, in a direction perpendicular to both **B** and **v**, accumulating at the sides of the sample. This accumulation will continue until the electric field created by these redirected carriers balances the effect of the magnetic field. The applied magnetic and induced electric fields can be measured, and the forces are in balance, so the carrier drift velocity could thus be determined experimentally. A more useful piece of information which can also be ascertained from this data is the carrier concentration. The average carrier drift velocity, **v**, the current density, **J**, and the carrier concentration, n, are related simply by:

$$\mathbf{J} = nq\mathbf{v} \qquad [24]$$

where q is the electric charge of a carrier, $-e$ for electrons, and e for holes. If the current flows in the z direction and the magnetic field is applied in the x direction, the induced electric field will be in -y direction. With this choice of directions, the balance of forces from Eq. 23 can be expressed:

$$E_y = -\frac{v_z}{c} B_x = -\frac{J_z}{nqc} B_x \qquad [25]$$

Collecting the current density and the fields on the same side of the equation and defining the Hall coefficient, R_H, this becomes:

$$R_H = -\frac{E_y}{J_z} B_x = \frac{1}{nqc} \qquad [26]$$

Thus a measurement of the Hall coefficient reveals the carrier concentration, and the sign of R_H reveals the carrier type. The foregoing development ignores the fact that the carriers involved have a spread of velocities, and it presumes that carriers of a single type dominate electrical conduction in the material.

The temperature dependence of the carrier concentration can be used to determine the binding energy of the dominant source of carriers. The $CdGeAs_2$ crystals studied here were always p-type when a carrier concentration could be determined, so it will be an acceptor binding energy which this analysis will reveal. For compensated material, at the lowest temperatures, the carrier concentration can be approximated by:[37]

$$n \approx -\frac{\beta N_v (N_a - N_d)}{N_d} \exp\left(-\frac{E_a - E_v}{kT}\right) \qquad [27]$$

Where β is a degeneracy factor for the donor, N_v is the valence band effective density of states, N_a is the density of acceptors present, N_d is the density of donors present, E_v is the energy of the top of the valence band, and E_a is the acceptor binding energy. Since the energy of interest is the depth of the acceptor level, that is how far above the valence band the acceptor level lies, E_v can be taken as the reference for zero energy, and E_a will be measured with respect to this level.

5.2. Hall Effect Equipment.

Resistivity and Hall Effect measurements were carried out using the van der Pauw method, which allows determination of the Hall coefficient, resistivity, carrier type, carrier concentration, and mobility using just four small contacts on the perimeter of a uniformly thin sample of arbitrary shape. For these measurements a turn-key system was used which featured an electromagnet capable of 7 kG, a closed cycle helium cooler capable of temperatures as low as 10 K, or as high as 320 K with use of a heater, and an automated data collection system.

Fig. 61 is an image of sample 4Q mounted on the Hall Effect sample holder. Samples were glued to the top of the sample holder with a small dot of rubber cement. The sample holder's surface had a thin sheet of sapphire attached to isolate the sample electrically from the metal body of the sample holder. The wires from the sample holder posts were soldered directly to the surface of the sample with indium metal. A tiny blob of molten indium, on the tip of a hot soldering iron, was found to make a good ohmic contact to the sample's surface after several seconds of contact. Effort was taken to use a clean, oxide free, blob of indium, but no flux was used.

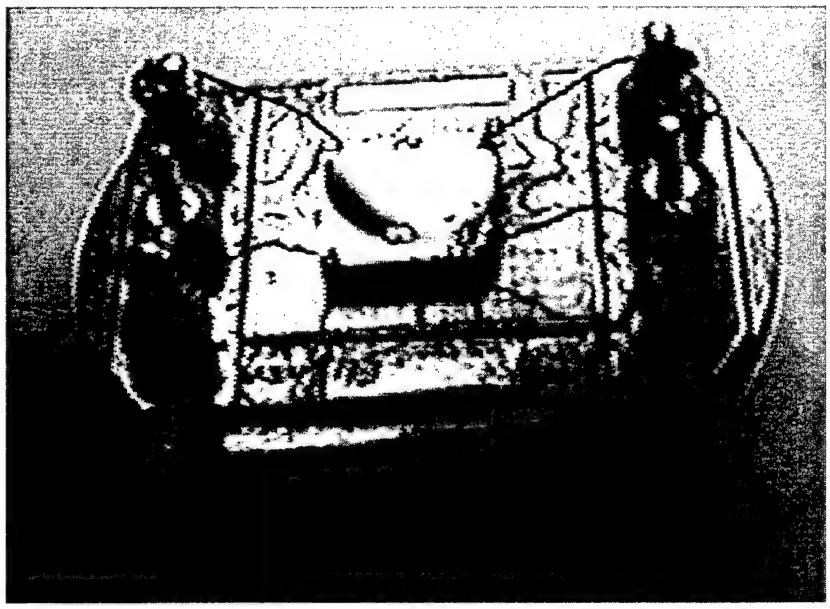

Figure 61. Hall Effect Sample Holder with Sample 4Q.

5.3. Hall Effect Results

The resistivity for samples 4M, 4O, and 4Q is plotted on a logarithmic scale on Fig. 62 as a function of inverse temperature. The resistivity rises quickly and fairly linearly as the temperature starts to decrease from room temperature, but soon the resistivity rolls over and levels off. The slope of a line drawn through the linear parts of this data can be used to estimate the depth of the acceptor level which gives rise to the carriers responsible for the electrical conduction observed. That is if the resistivity, ρ, varies with temperature in the proportion:

$$\rho \propto \exp\left(\frac{E_a}{kT}\right) \qquad [28]$$

then on a logarithmic scale this becomes:

$$\ln(\rho) = \log_{10}(\rho)\ln(10) = \frac{E_a}{kT} + C \qquad [29]$$

where the constant of proportionality is absorbed into the constant C. Since the ordinate on Fig. 62 is $1000/T$, the slope of a straight line on this figure is:

$$m = \frac{E_a}{1000\ln(10)k} \qquad [30]$$

and the activation energy sought is just:

$$E_a = 1000\ln(10)km. \qquad [31]$$

This estimate for E_a is based upon the presumption that the resistivity is inversely proportional to the carrier concentration. This presumption is not completely correct because the variation of mobility with temperature is often too large to ignore. However,

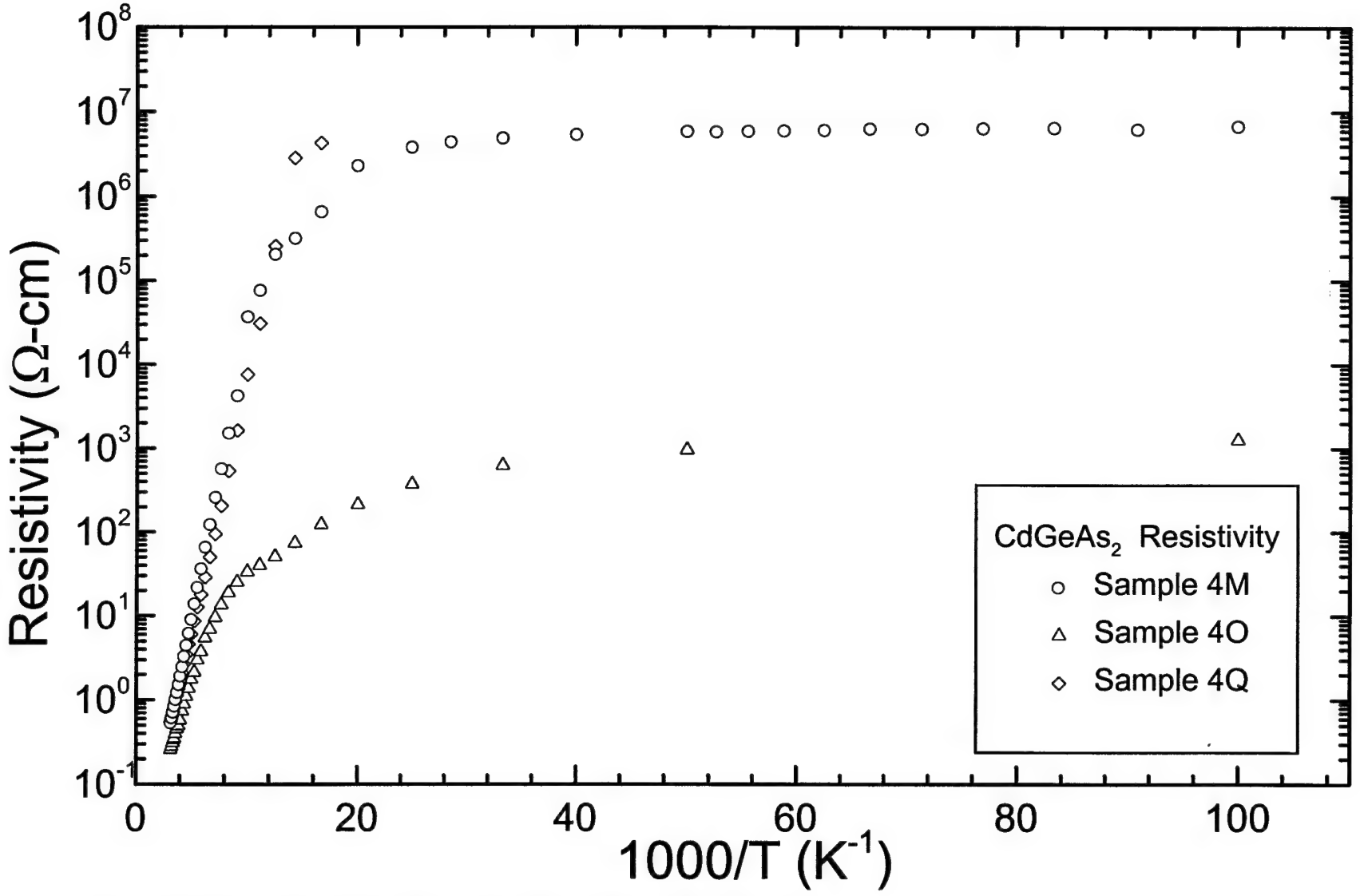

Figure 62. Resistivity vs. Temperature (Whole Range) for $CdGeAs_2$.

if the carrier concentration cannot be determined this approach provides a rough estimate of $1000\ln(10)k$ Fig. 63 shows a smaller range of the data from Fig. 62 along with straight line fits to the linear portion of the data sets. The range of values estimated for E_a (86 meV-133 meV) is too large for this acceptor to be a part of the DAP responsible for the 0.57 eV low temperature PL peak.

Fig. 64 shows the resistivity of sample 4M measured at the lowest temperatures achievable by the closed cycle cooler. This section of the data set looks flat when considered on Fig. 62, but a straight line fit here is not very convincing. The energy level implied by the straight line shown is also too small to suggest that this is an acceptor level. At these low temperatures, where a consistent carrier type could not be determined, conduction is probably due to electrons (or holes) tunnelling or hopping between defect sites.

The variation of carrier concentration with temperature gives a much more consistent prediction of E_a. Fig. 65 shows the carrier concentration of these same samples as a function of inverse temperature. From Eq. 27 it is apparent that the previous analysis for resistivity applies here as well, and the relationship between the slope of data and E_a derived there now only changes by a minus sign, that is:

$$E_a = -1000\ln(10)km. \qquad [32]$$

Now the range of values estimated for E_a has narrowed to 107 meV-123 meV. This is further evidence ruling out the participation of this acceptor level in the low temperature 0.57 eV DAP PL luminescence observed, since this level is too deep.

The disagreement between the slope of the carrier concentration and resistivity data is due to the variation of mobility with temperature in these samples. The mobility as a function of inverse temperature is shown on Fig. 66. No clear trend is apparent in this data. Mobility is expected to be low at high temperatures, due to increasing

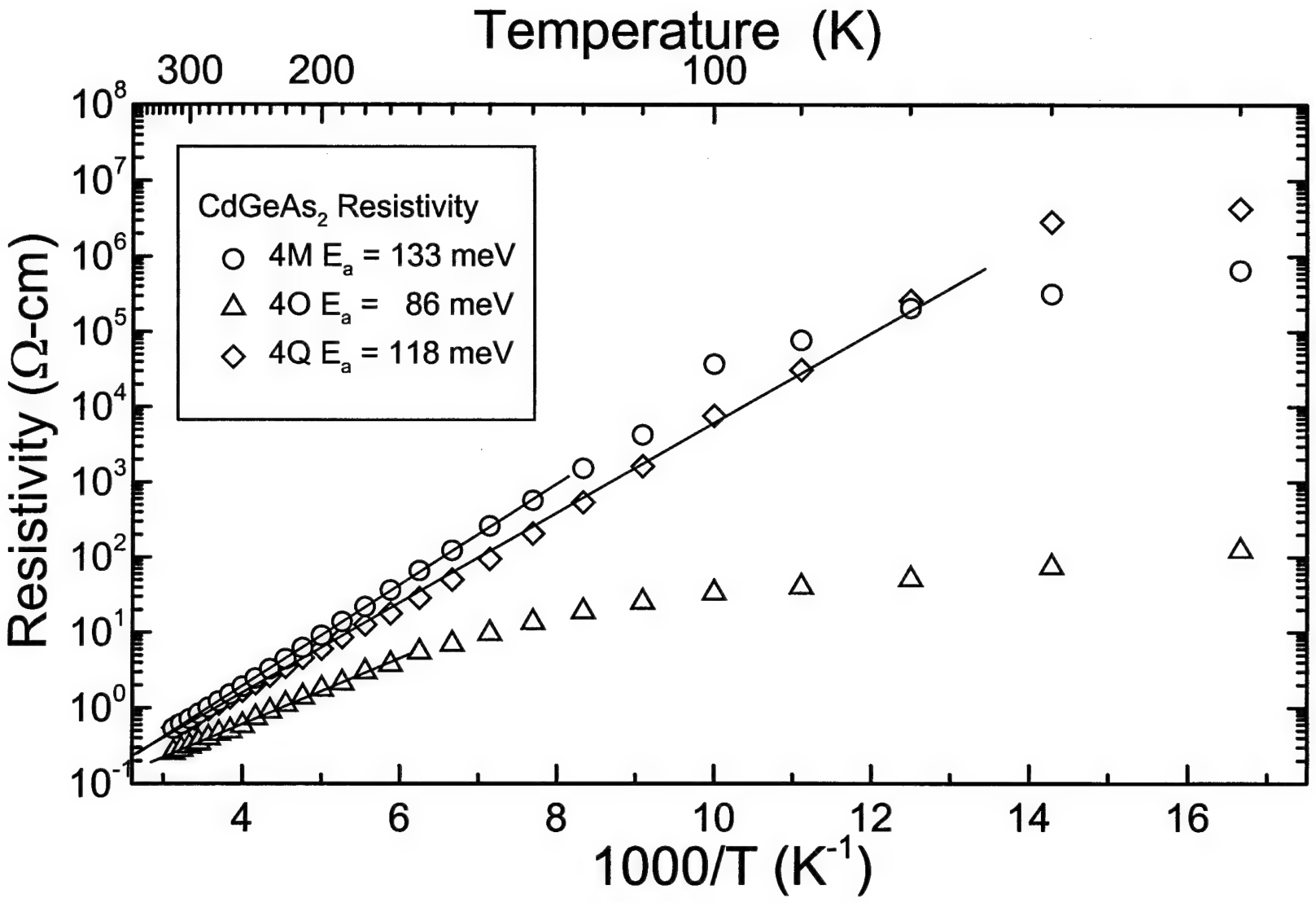

Figure 63. Resistivity vs. Temperature (High Range) with Straight Line Fits for E_a

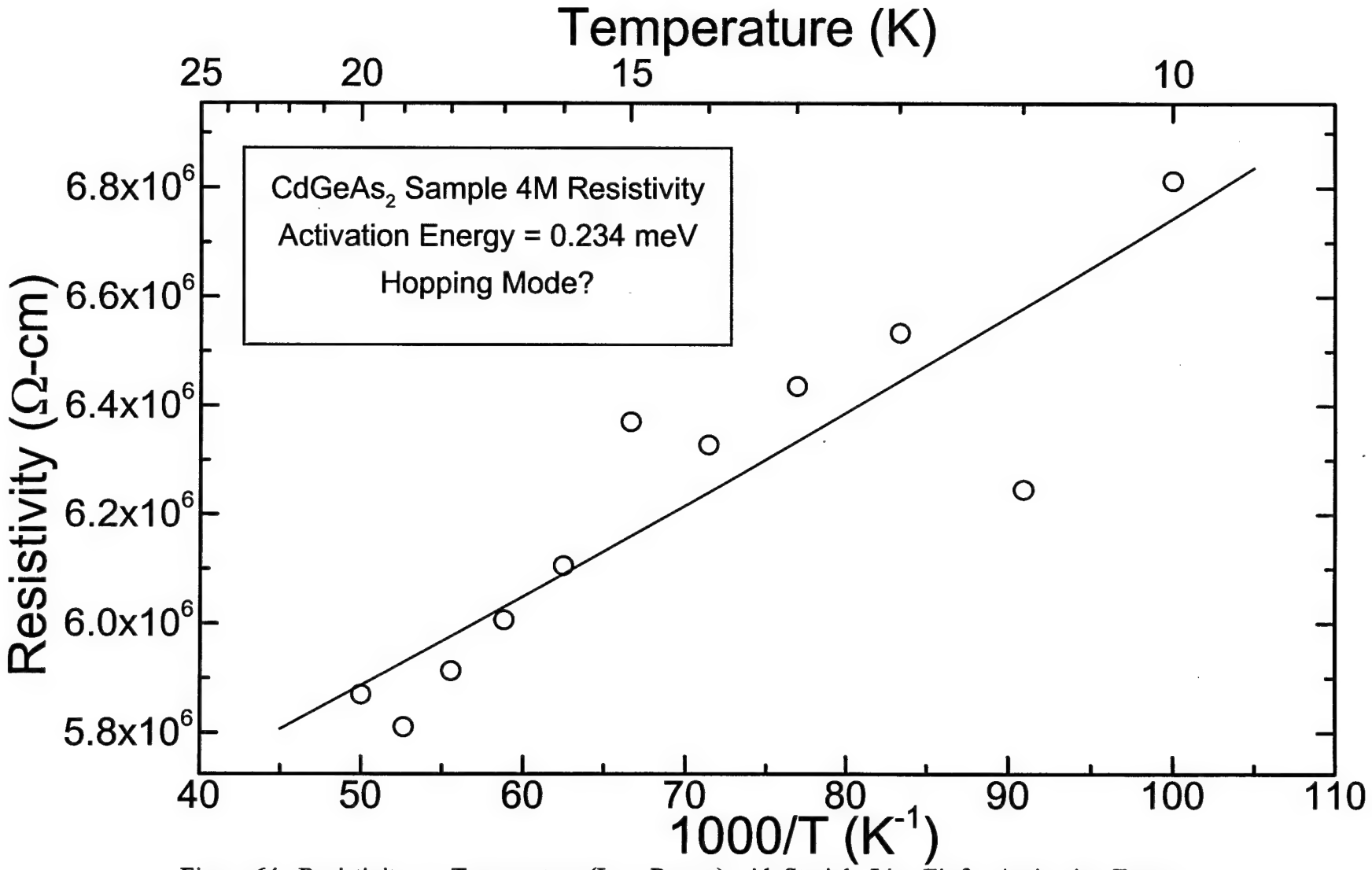

Figure 64. Resistivity vs. Temperature (Low Range) with Straight Line Fit for Activation Energy.

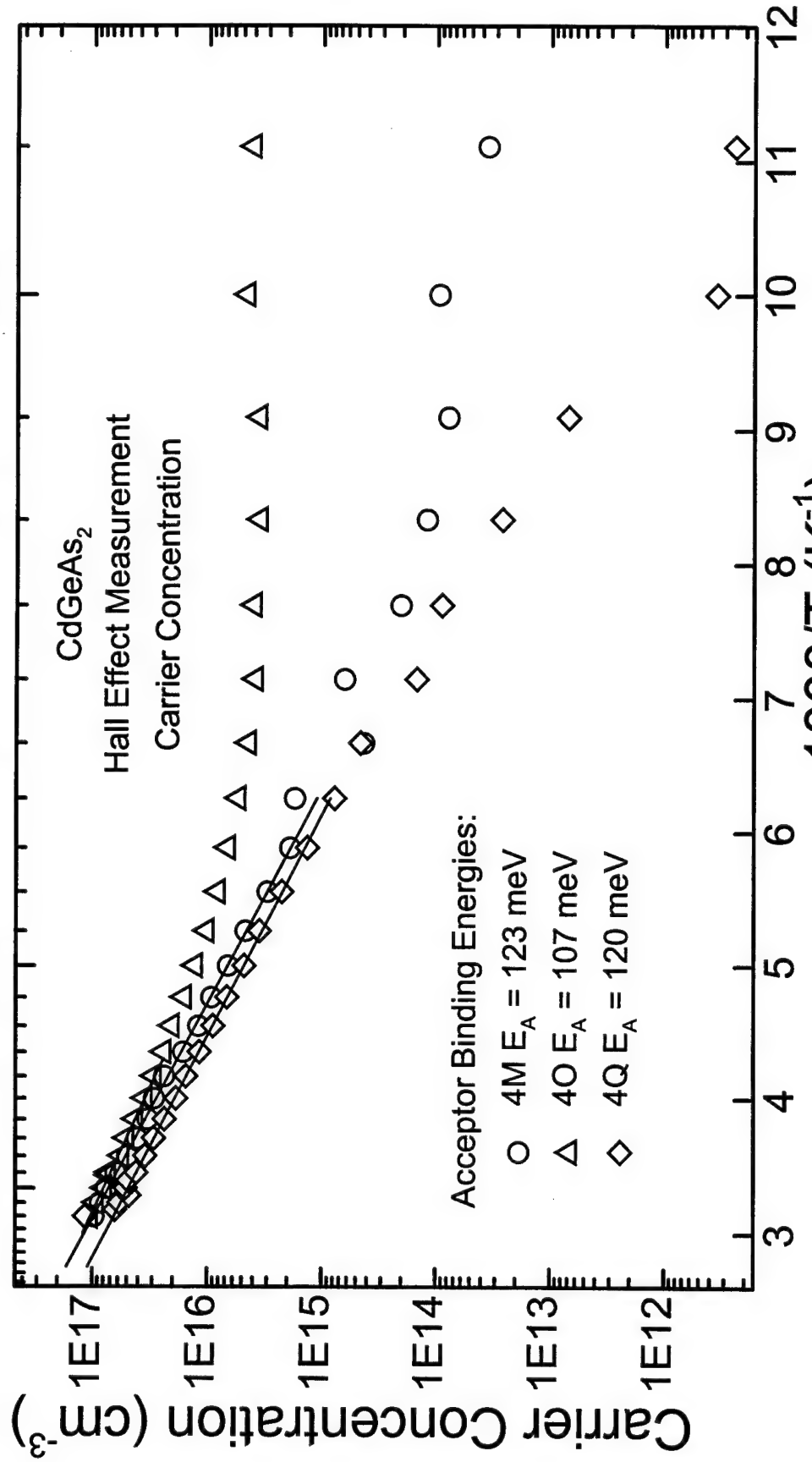

Figure 65. CarrierConcentration vs. Temperature for $CdGeAs_2$, with Straight Line Fits for E_a.

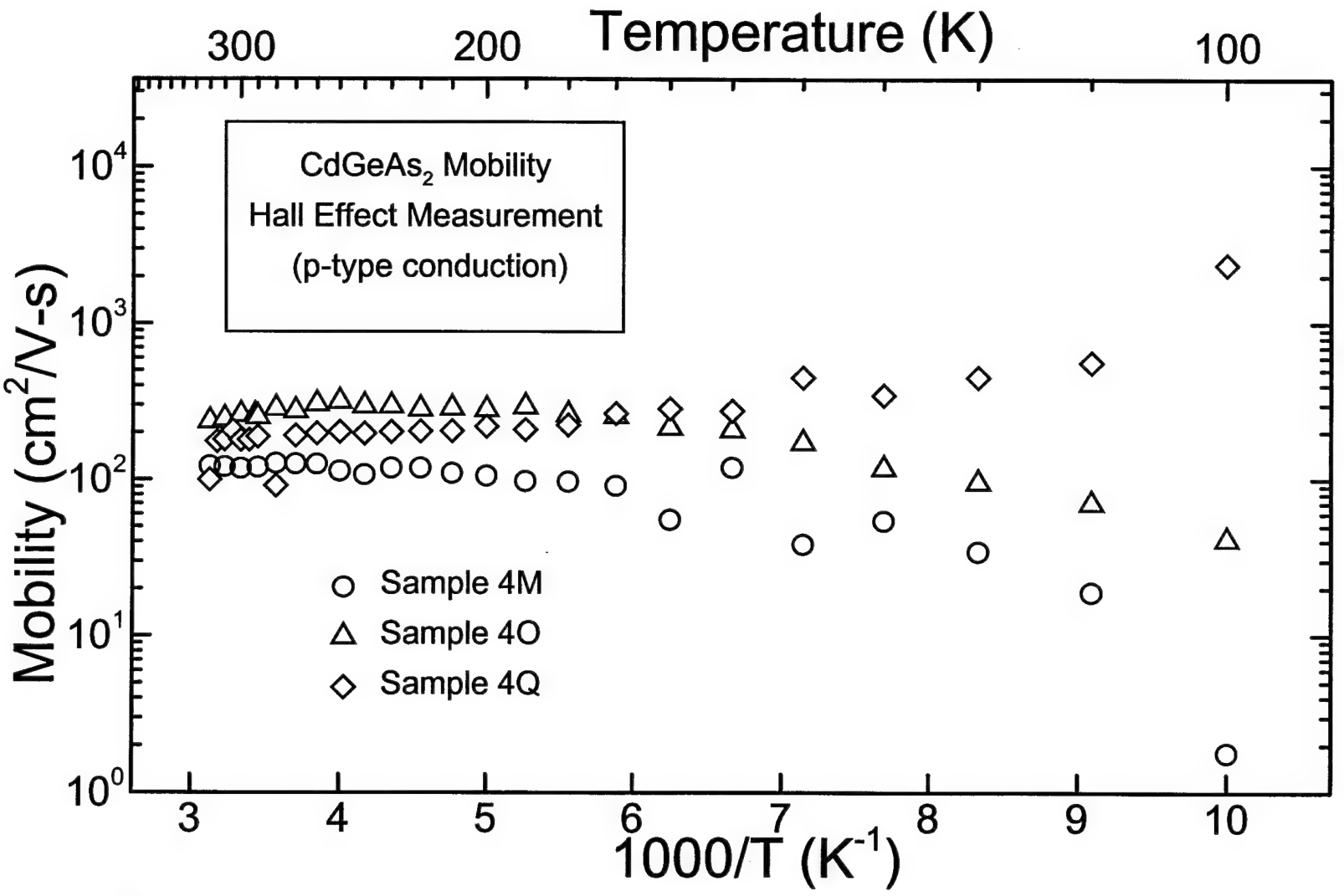

Figure 66. Mobility vs. Temperature for $CdGeAs_2$.

scattering due to lattice vibrations, and it is also expected to be low at low temperatures, because the carriers are moving more slowly and thus have more time to interact with ionized impurities. So mobility can be expected to peak at some intermediate temperature. It does not look like this intermediate temperature is necessarily captured within the domain of temperatures over which measurements were made for any of these samples.

Chapter VI. Conclusions

6.1. Reconciliation of the PR and PL Results.

The PL and PR results can be compared to provide more evidence that the high temperature PL is dominated by band-to-band recombination. Fig. 67 shows the PL peak position data from Fig. 42, combined with the bandgap curve from Fig. 60. Just below 100 K the PL peak position jumps up in energy as the temperature rises. The magnitude of this jump is around 25-30 meV. From the low laser power value of the low temperature peak position this jump is even bigger. This transition is presumably due to one or both of the levels involved in the DAP being ionized before radiative recombination can take place. If only one of the levels involved in the DAP is being ionized where this jump occurs, it should be the level with the lower ionization energy since this level will be easier to ionize thermally. The remaining level would then be estimated to be much deeper than the 25-30 meV jump seen below 100 K, since this level remains unionized at a temperature three times as high (292 K). If the high temperature PL was due to free-to-bound transitions involving this level, the bandgap would then have to be much more than 25-30 meV above the PL peak position observed. This proposition is seen to disagree with the bandgap curve on Fig. 67, where only about 32 meV separates the PL peak position from the bandgap. Ruling this possibility out leaves band-to-band recombination the leading candidate for the source of the room temperature PL.

The remaining difference between the bandgap curve and the PL peak position data can be explained by realizing that different methods for estimating the bandgap can result in different values. The 0.547 eV peak position of the room temperature PL falls squarely between values found for the bandgap of this material based upon optical absorption (0.53 eV), and the value obtained by electroreflectance (0.57), or here by PR

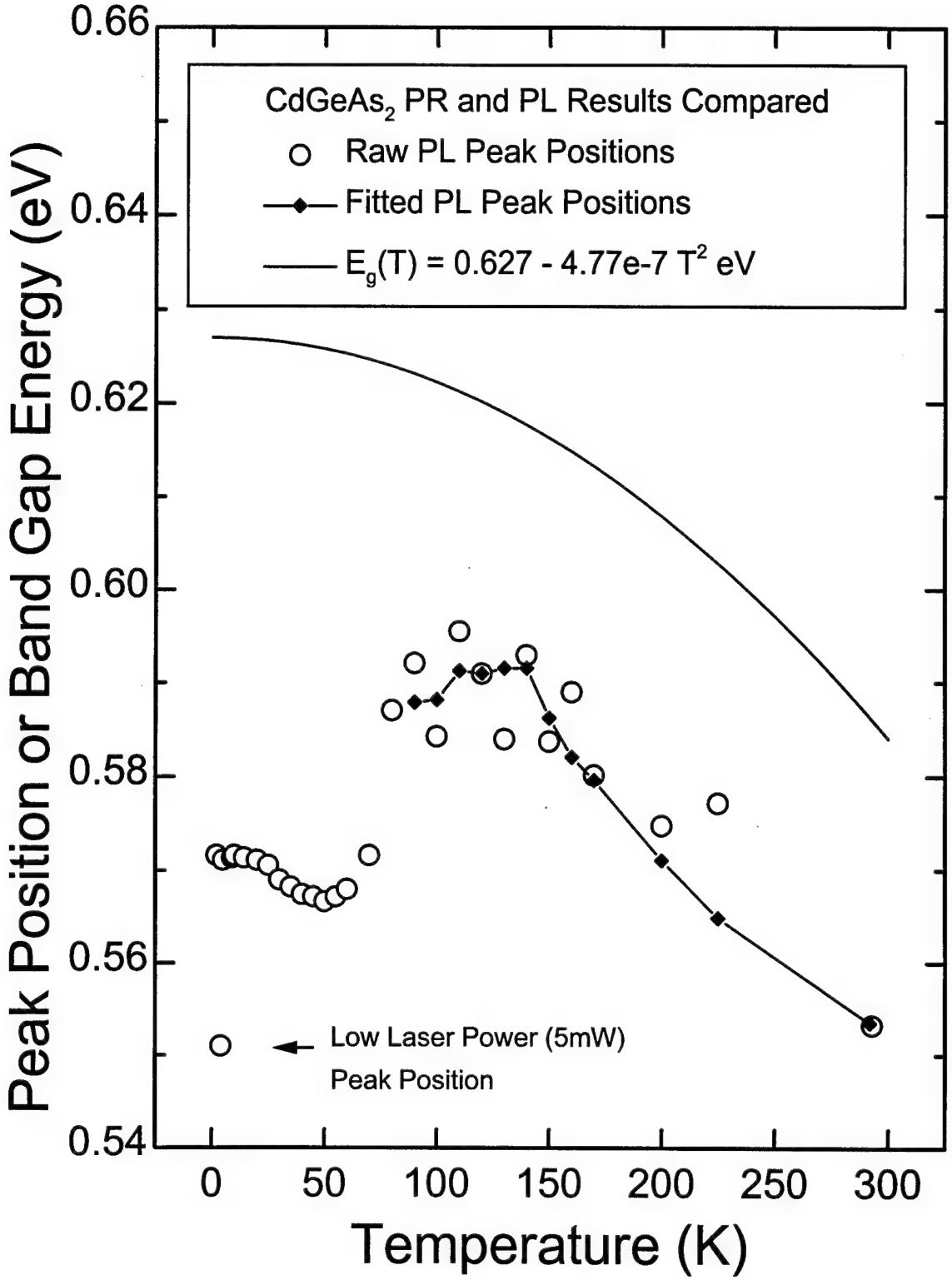

Figure 67. PL and PR Results Compared

(0.58 eV). Since these techniques are based upon different effects, this difference isn't too surprising. If a spread of bandgap values were present in a sample it would be expected that absorption would find a low value, since the absorption would increase rapidly when the density of states starts to grow. Reflectance modulation, on the other hand, should be strongest where the rate of change of the density of states is the steepest, since it is a derivative technique. This could then be expected to result in a higher value found by modulation means than by absorption methods, especially for material with a significant amount of band-tailing or inhomogeneity present.

6.2. Comparing $CdGeAs_2$ and $ZnGeP_2$.

While $CdGeAs_2$ and $ZnGeP_2$ are both II-IV-V_2 chalcopyrites, and their non-linear optical coefficients and birefringence make the two of the most promising non-linear optical materials being pursued today, many of their other electronic and optical properties are very different. $ZnGeP_2$ has GaP as a III-V analog, so its band structure can be well approximated by folding the GaP band Structure into the chalcopyrite Brillouin zone, $CdGeAs_2$ has no exact binary III-V analog, and its structure would then be expected to lie somewhere between that of GaAs and InAs placed into the chalcopyrite Brillouin zone. $ZnGeP_2$ has a pseudodirect bandgap, which is essentially indirect for most purposes, while $CdGeAs_2$ has a direct bandgap. The near band edge optical absorption problem in $ZnGeP_2$ is believed to be due to photoionization of acceptors, (or perhaps donor-acceptor pairs). While this may also be the case in $CdGeAs_2$, its near band edge absorption problem is clearly aggravated, at least at room temperature by band-to-band absorption between the top valence band and the valence bands split off by the interaction of the non-cubic crystal field and spin-orbit coupling. One key feature both semiconductors share is a plentiful acceptor state near the middle of the bandgap, caused by a native defect, probably a group II cation vacancy.

6.3. Optical Absorption and Crystal Quality.

Absorption measurements made by the Air Force Materials Lab order the quality of several of the crystals studied here as follows: 2G>4Q>4M>4O. Where greater means less absorption. Fig. 68 shows these absorption measurements.[38] At room temperature measured carrier concentrations and resistivities agree with this order, that is low carrier concentrations and high resistivities correlate with high crystal transparency. The Materials Lab conducted these electrical measurements on sample 2G. The level at which the low temperature resistivity saturated mixes this ordering, finding: 4Q>4M>2G>4O, where higher resitivity is presumed to be better. Judging by the brightness of PL observed at low temperature, the opposite is concluded: 4M>4Q>2G, where bright PL is presumed to be a sign of a good crystal. While PL from sample 4O wasn't measured, this trend obviously cannot continue forever - a sufficiently bad sample would be expected to give little or no PL.

These various rankings of this set of samples can be largely explained by considering both the concentration of defects, as well as the compensation of each crystal. For a crystal to be highly transparent it must have a low concentration of defects, but the defects present must also be well compensated to stop intervalence band absorption. Room temperature measurements of resitivity and carrier concentration can be expected to follow this prescription as well. At low temperatures, where the semiconductor is frozen-out, compensation becomes unimportant and the defect density should determine the ranking of these crystals. Indeed, the low temperature resistivity and the low temperature PL brightness measurements agree somewhat here (samples 4O and 4Q aren't extremely different in either of these measures).

This leads to the conclusion that sample 2G doesn't have the lowest optical absorption because it has the fewest defects, but that it has the lowest optical absorption because it has a relatively small number of defects and it also happens to be very well compensated. Likewise, samples 4Q and 4M, which don't have the lowest optical

absorption, have a lower defect density, and would presumably be the lowest loss samples, if they were more closely compensated. Electron beam irradiation has been shown capable of making $CdGeAs_2$ more n-type. PL and low temperature resistivity measurement appear to be good candidates for selecting which crystals optical properties might be improved by such processing.

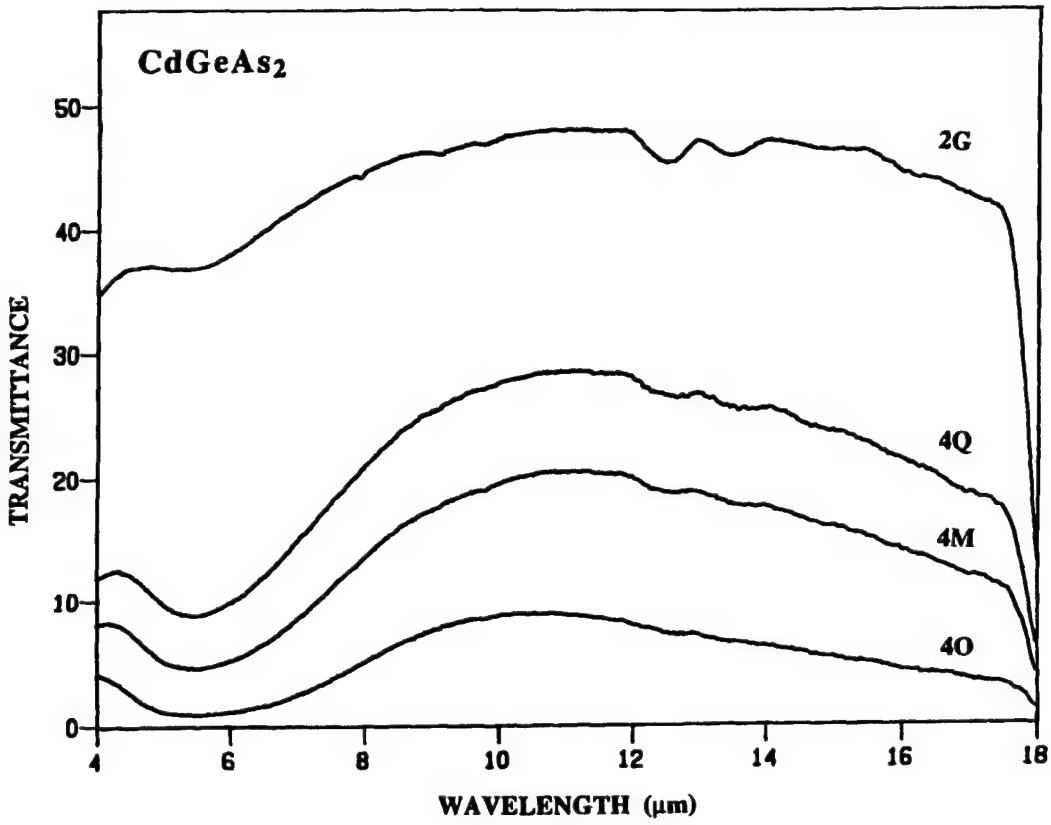

Figure 68. Infrared Transmission Spectra for $CdGeAs_2$ Samples[38]

6.4. Recommendations.

Knowledge of the bandgap of $CdGeAs_2$ is important to interpretation of PL results, and important in predicting crystal performance in non-linear optical systems. Knowledge of the motion of the bandgap with temperature is of particular interest when predicting what kind of improvements can be expected in crystal transparency as the temperature is lowered. Reported bandgap values are in disagreement with each other,

and in some disagreement with what is measured here. The Varshni-type equation presented in this work for the bandgap of $CdGeAs_2$ assumed a quadratic form. For these reasons additional effort to more positively quantify the bandgap is warranted.

Several trade-offs had to be made in assembling the PR experiment used for this work. The windows on the sample chamber used are small, so getting the beam of light from the spectrometer both in and out through these windows interfered with attempts to focus as tightly as possible on the sample. Additionally, a good bit of light is lost because there are two windows between the sample chamber and the room. Use of a helitran or closed cycle type cooling system would improve this situation, especially if the window on the sample chamber were larger, at least in terms of numerical aperture. The spectrometer used for the tunable light source also limited the quality of the data measured. The grating used was blazed for 1.5 μm, the use of a grating blazed for 2 μm would put more light in the region around the bandgap, and allow data to be taken out to longer wavelengths.

In combination, the above recommendations should make PR measurements on this material easier and more valuable. Since ER and PR results for $CdGeAs_2$ are in some disagreement, both experiments could be carried out on the same sample. These experiments are compatible enough that this could be done almost simultaneously.

Many of the questions raised here about of $CdGeAs_2$ could be answered with a more comprehensive study involving many more samples. The use of electron beam radiation and annealing to compensate p-type crystals would be most valuable if several nearly identical samples were available at the start. This would allow the relationship between absorption, compensation, PL and defects to be quantified. Also, the role of compensation in PR could also be addressed.

6.5. Contributions.

The first $CdGeAs_2$ PL spectra that have been reported for this material are presented here. The single previous report[5] of luminescence from this compound being based upon strong electron beam excitation. The temperature, laser power, polarization/sample orientation, and sample-to-sample dependences of the PL reported here provide new insight into the nature of the optically active defects in this material. The Mid-IR PL reported on $ZnGeP_2$ also represents a heretofore unresearched area, as none of the many previous reports of PL from $ZnGeP_2$ used a detector capable of operating this far into the infrared; it was only done here because both $ZnGeP_2$ and $CdGeAs_2$ were being studied. This work includes the first reported PR spectra from $CdGeAs_2$. In this case results obtained by others via ER[7,9] should have yielded similar results. This proves to be not quite correct, as the bandgap indicated via PR at low temperature for the samples studied here is lower than that found in the literature (for other samples). Additionally, neither of the previous ER efforts looked at temperature dependences.

Appendix A: Calibration and Resolution of the Monochromators.

The grating spectrometers used for PL and PR are capable of achieving high spectral resolution and accuracy, but the actual resolution and accuracy obtained depends upon how they are used. The ultimate resolution limit of a grating monochromator is given by $\lambda/\Delta\lambda = mN$, where m is the diffraction order in which the instrument is used, and N is the total number of grooves on the grating.[39] The grating used for PL, as stated in section 3.2, had 300 grooves/mm and was 4 inches in size, while the grating used for PR, as stated in section 4.2, had 600 grooves/mm and was 2 inches in size. Thus each grating had about 30,000 grooves. At 2 μm $\Delta\lambda$ corresponds to 0.066 nm, a resolution far finer than any needed for this work. When the spectrometer slits are not set to an extremely narrow width, the actual resolution achieved will not be near this limit, and the instrument's dispersion will completely dominate the resolution achieved. The instrument's dispersion is computed by differentiating the grating equation (for wavelength) with respect to the angle of diffraction.[39] The grating equation is:

$$d(\sin\alpha - \sin\beta) = m\lambda \qquad [33]$$

where d is the spacing between grating grooves, α is the angle of incidence and β is the angle of diffraction (both with respect to the grating normal), m is the order, and λ is the wavelength. Thus, in first order the angular dispersion is given by:

$$\frac{d\lambda}{d\beta} = -d\cos\beta \qquad [34]$$

The angle β itself varies with wavelength, and also depends on the geometry of the spectrometer. When the spectrometer is set at λ=0, β is half the angle between the grating and the mirrors, 11.7° for the Spex monochromator. When the spectrometer

reaches the 3 μm, for which the grating is blazed, this angle has fallen by about the blaze angle of 26.75°, so β is now about -15°. Here $\cos\beta = 0.97$, so the cosine term in Eq. 34 will be taken as 1 for the purpose of this analysis. The spread of wavelengths across the exit slit, is then the angular dispersion times the spread of diffraction angles escaping through the slit. In the present case, the slits were usually set to 2 mm, so the range of diffraction angles escaping, $\Delta\beta$, is this divided by the instruments focal length of 0.5 m, thus $\Delta\beta$=0.004 Rad, and $\Delta\lambda = \Delta\beta$/300 grooves/mm = 13 nm. This resolution is still far narrower than any of the features seen in this work. Opening the entrance slit up to the same width as the exit slit does not degrade the resolution further, as a narrow spectral line will have the same full-width half-maximum, albeit with a triangular instead of rectangular profile. The above has shown that the instrument resolution is more than sufficient for the work conducted here, but the accuracy of these instruments is independent of these arguments and must be addressed separately.

Often a spectrometer is calibrated with a gas discharge lamp, because many well determined wavelengths are available from such a source for this application. In the infrared this was not so easy, since no such sources were available. The accuracy of these spectrometers was insured by measuring where on the spectrometer dial the various orders of visible lasers appeared. Since the detectors used for the infrared had filters designed to block out short wavelengths, the detector was removed, and the spectrometer output was viewed on a card. In the case of the Jarrel-Ash monochromator used for PR experiments, the dial read half the actual wavelength, so the calibration was related back to the dial. Fig. 69 shows the difference between what the dial read, and what the dial would be expected to read, as a function of the dial wavelength. The straight line on this figure is the difference between a least squares fit of these dial readings and the expected readings. The straight line thus represents the correction needed at a given place on the dial. Even with this correction, some disagreement between the straight line and the data

points is present. This error amounts to 10-15 nm at the extreme, and is comparable to the instrument resolution achieved with the actual slit widths used. Fig. 70 shows the disagreement between dial and actual wavelengths for the Spex monochromator used for PL; this disparity is far smaller than the instrument resolution achieved, so it was not necessary to try to correct for the small trend observed.

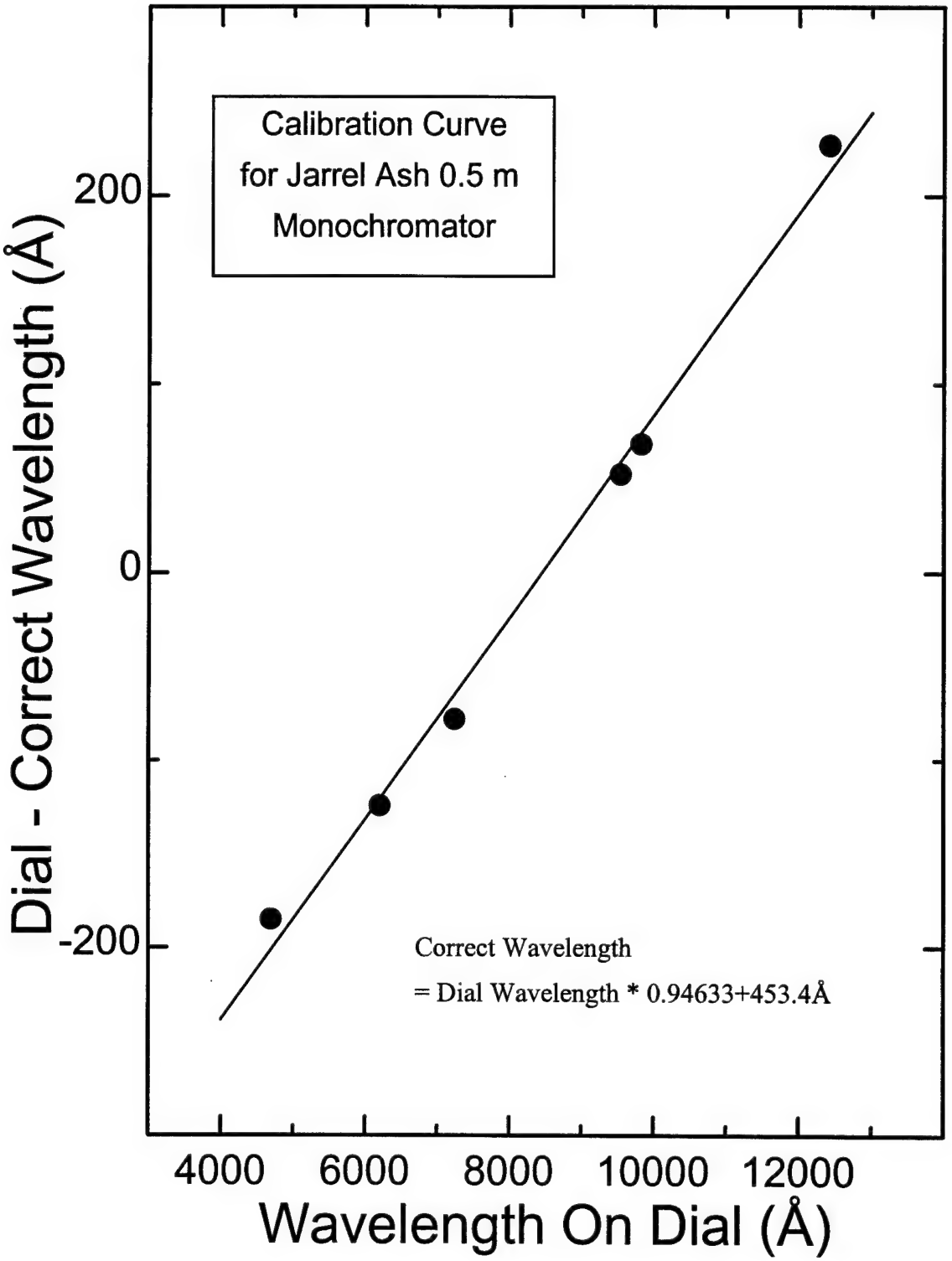

Figure 69. Calibration Data for Jarrel-Ash 0.5 m Monochromator

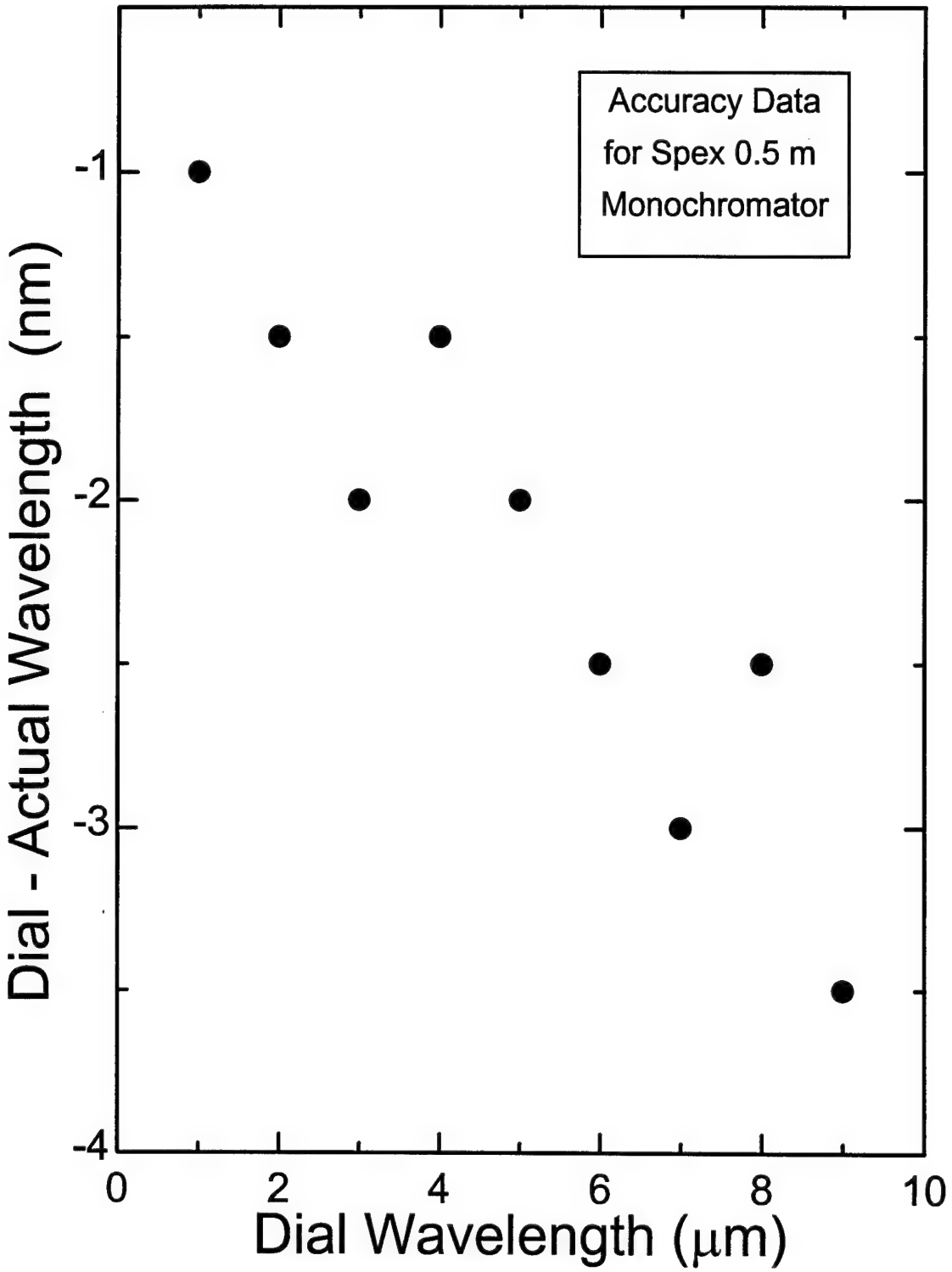

Figure 70. Accuracy Data for Spex 0.5 m Monochromator

Appendix B: Correction of Spectra for System Response.

Measuring the system response is easy. A source with a known broadband spectrum (always a blackbody) is measured. Then any other spectrum may be corrected for the system response by multiplying it (at each point) by the computed spectrum, and dividing this result by the measured one. This simple process removes the wavelength dependent effects of every element of the system. There are a few complications involved however.

There are at least four reasonable choices for the computed spectrum, based on what units are desired for the corrected spectrum. Since photovoltaic detectors and photomultiplier tubes are essentially photon counting devices it makes some sense to base our corrected spectra on photon flux, rather than energy flux. Thus the computed spectrum used will be the blackbody curve for photons per interval. (This amounts to not dividing out the downslope (high energy side) of the detectivity curves for these detectors). Also open to consideration is the ordinate of the computed spectrum; the computed spectrum may be the photon flux per unit wavelength, or per unit frequency (or equivalently energy). These units are inversely proportional to each other and this will affect the shape of the resulting curve. Since the spectrometer takes data per wavelength interval (assuming fixed slits), the corrections used thus far are based on a wavelength interval as well. However, the model spectrum of Eq. 5 is based on an energy interval, thus sometimes an energy interval would be preferred (evenly spaced data on that interval as well, but here we are stuck).

The polarization response of the spectrometer is so large that it must be included in any correction scheme as well, unless it is know that the source being studied is unpolarized. This means that spectra from a source with unknown polarization, or a source which is known to be polarized, must be taken through a polarizer, then

recombined to give a total spectrum. Of course, if the source is totally polarized to begin with, the polarizer is not needed, but the system response needs to be known for this particular polarization. Fig. 71 shows the measured and computed spectra for vertically polarized light, as well as their ratio, which would now be divided into any other measured spectrum to correct it. The noise apparent near 0.5 eV is due to CO_2 or H_2O absorption across the short path through the atmosphere between the blackbody source (and within the blackbody source) and the sample chamber (the blackbody is shined through the sample chamber). This noise is added to the corrected spectra, since the PL beam path is enclosed and well purged. Fortunately, the PL spectra measured show little light in this region. Fig. 72 shows both the vertically and horizontally polarized blackbody spectra measured. Clearly the polarization response is strong. Fig. 73 shows the degree of polarization of the spectra measured in Fig. 72. This is the difference between the spectra divided by their sum. This curve is fully discussed in Appendix C.

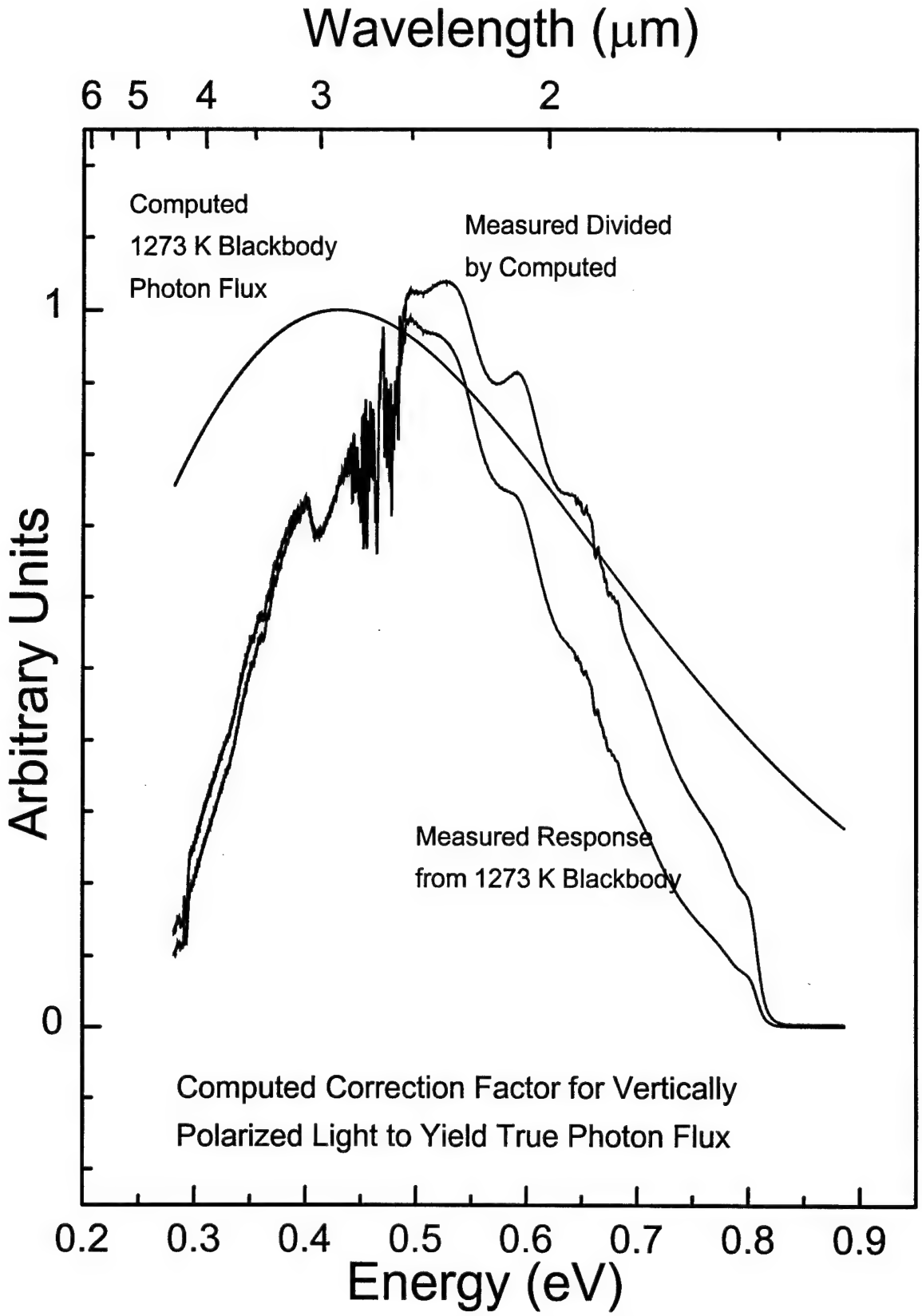

Figure 71. System Response Correction Curve for Vertically Polarized Light.

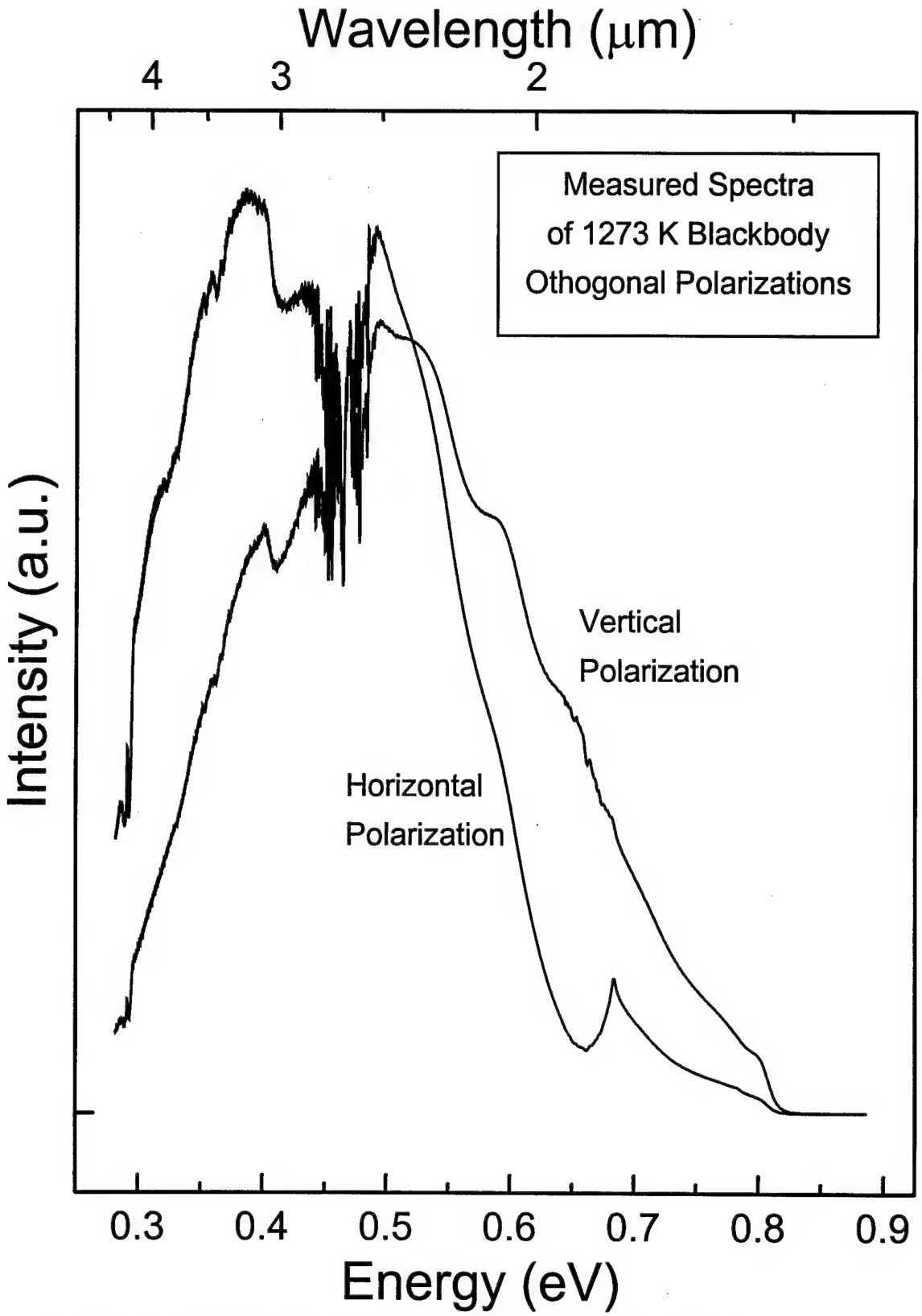

Figure 72. Measured Blackbody Spectra for Orthogonal Polarizations.

Appendix C. Polarization Response of the Spectrometer.

Figs. 72 & 73 discussed above show the strength of the polarization response of the whole system. While the whole system contributes to the responses seen in Fig. 72, the degree of polarization plotted in Fig. 73 is due only to those elements of the system which are polarization sensitive. The only component of the system which can be expected to display much polarization sensitivity in this application is the diffraction grating. At long wavelengths the grating can be expected to act somewhat like a wire grid polarizer, causing greater attenuation for light polarized parallel to the grooves (P), as is shown in Fig. 73. As the wavelength decreases from the blaze wavelength, the angle from the normal of each grating step to the exit slit grows continuously. This leads to a Brewster angle type situation which preferentially scatters light polarized along the direction of the grating grooves. This trend too is seen of Fig. 73, at least up to a point. These overall trends are slow functions of wavelength and unlikely to trouble most experiments.

The strong marked features on Fig. 73 are not explained by this trend. These features are believed to be grating anomalies. The first and simplest explanation for features like these is due to Lord Rayleigh.[40] He suggested that every time a diffraction order passed over the grating horizon, that is reached an angle of 90° to the grating surface, the redistribution of the energy which had been going into this order caused rapid changes in the intensities of the other orders. Not all grating anomalies are explained by this theory. More complicated theories based upon the actual electromagnetics of light interacting with a corrugated metal surface and surface plasmons have been shown to better describe the anomalies observed. For instance, this simple theory provides no information about intensity distributions. In the present case Lord Rayleigh's theory does an admirable job of explaining all three features marked on Fig. 73; furthermore, it

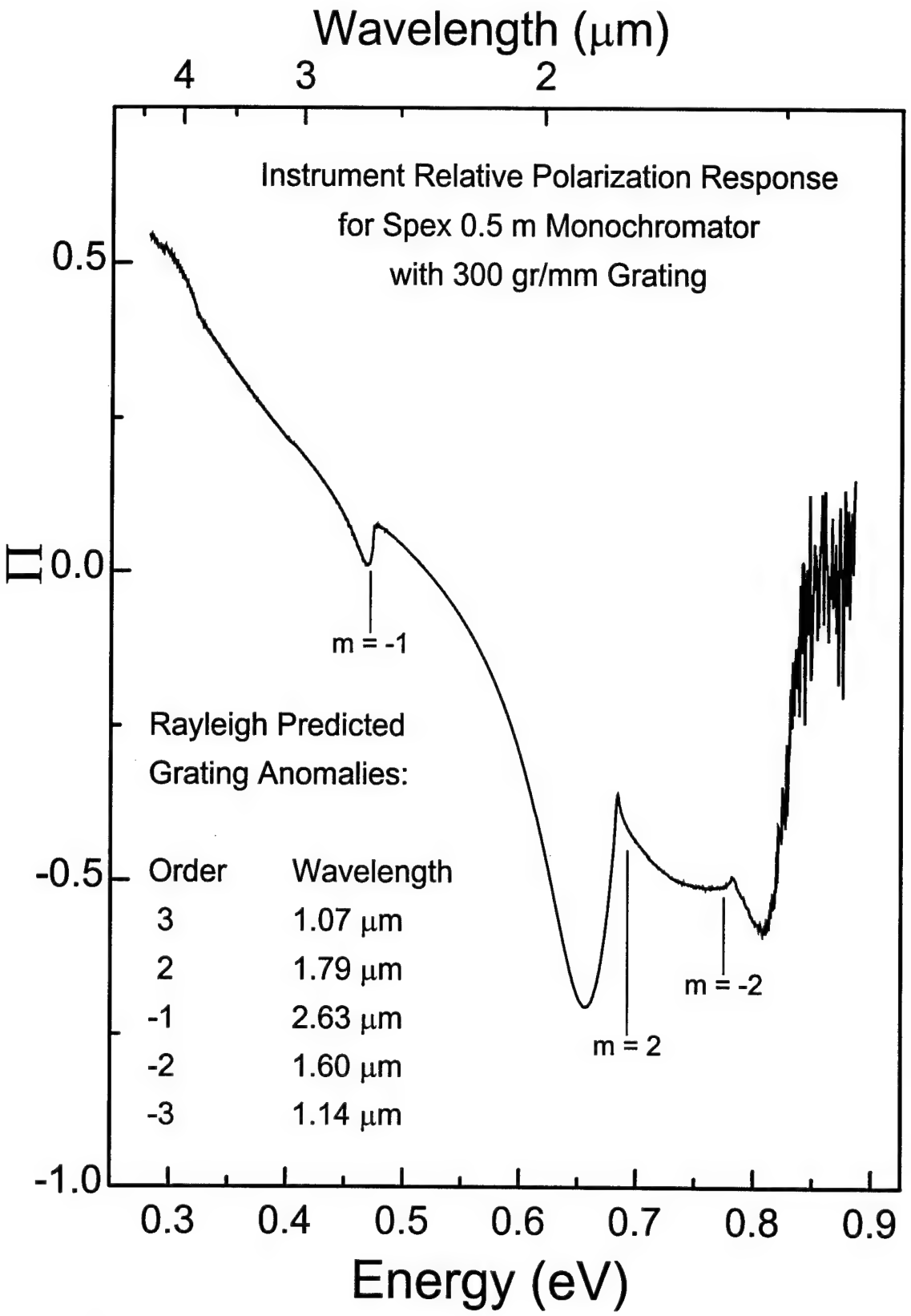

Figure 73. Instrument Relative Polarization Response.

predicts correctly that these are the only grating anomalies which will be observed over the wavelength range plotted. The range of wavelengths shown on Fig. 73 is limited by the cold filter on the detector. While this cuts out any grating anomalies which might have been seen at shorter wavelengths, is was necessary to prevent light at short wavelengths from being detected at higher orders.

Having measured the angle between the centers of the monochromator mirrors and the center of the grating to be 23.4°, it is a simple matter to use the grating equation to compute the location at which each grating anomaly should appear. These results are tabulated on Fig. 73. The predicted positions of the m = 2 and m = -2 orders are seen just inside the cusps observed, this slight motion can be attributed to the accuracy with which the mirror to mirror angle was measured (if indeed the cusps are what this theory predicts). Another possible source of this discrepancy is the extent of the mirrors and gratings. This introduces a spread of angles that the center-to-center-to-center measurement used here ignores.

Appendix D: Effects of Boundary Conditions on Polarization Observed.

Since the face of the sample is not perpendicular to the direction in which light is collected, the measured polarization of the emitted light may be affected by differing transmittance at the surface for different polarizations. This difference can be computed and taken into account when examining the polarization of measured spectra. Fig. 74 shows the coordinate system and variables used for the discussion which follows.

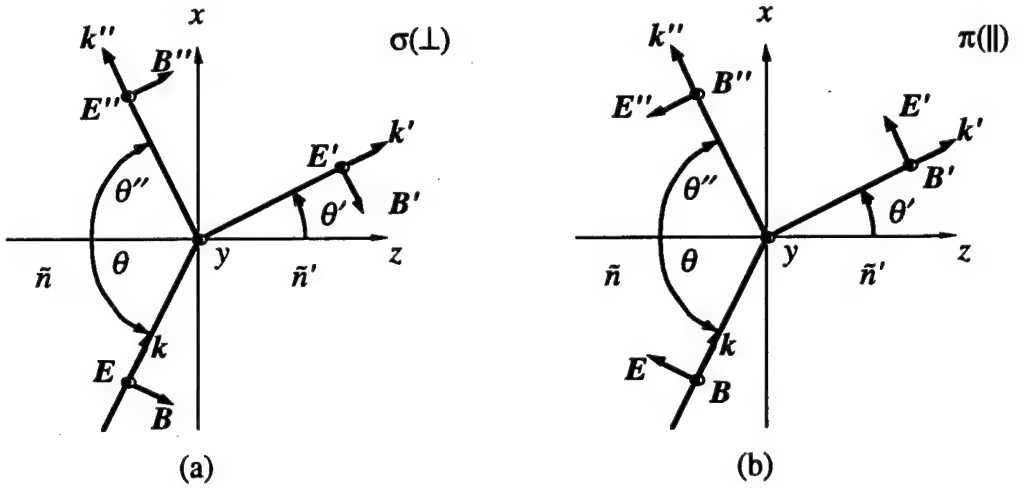

Figure 74. Geometry that establishes the conventions for optics at an interface: (a) ***E*** perpendicular to the plane of incidence; (b) ***E*** parallel to the plane of incidence.[41]

For samples mounted with their c-axis vertical (usually the case if the c-axis is known) light polarized along the c-axis corresponds to the σ case and light polarized perpendicularly to the c-axis corresponds to the π case. The transmission coefficients for these two cases are:[41]

$$\tau_\sigma = \frac{2\sin\Theta'\cos\Theta}{\sin(\Theta+\Theta')}$$

$$\tau_{\pi} = \frac{2\sin\Theta'\cos\Theta}{\sin(\Theta+\Theta')\cos(\Theta-\Theta')}$$

and the transmittance for each case is then:[41]

$$T = |\tau|^2 \frac{n'\cos\Theta'}{n\cos\Theta}$$

The orientation of the sample will be seen to alter the actual polarization ratio by a factor of:

$$T_{\pi}/T_{\sigma} = \sec^2(\Theta-\Theta')$$

Surprisingly, (at least to me) this bias is not maximized at the Brewster angle, where the π component suffers no reflection loss, but rather at the maximum external angle of 90° where both components achieve total internal reflection. As this extreme angle is approached the alteration in the polarization ratio approaches $(n/n')^2$. In the case of $CdGeAs_2$ PL as measured in the lab, the external angle is kept around 45°, the index of refraction, n, can be taken as 3.7, and 1 will be used as the index for air, n'. This results in T_{π}/T_{σ}= 1.45, if the external angle were as big as 50° (it might sometimes be this large) then we would get T_{π}/T_{σ}= 1.61. This effect can then be seen explaining about half of the discrepancy between the observed and predicted polarization ratios. Other effects which complicate this matter further are not included in this analysis. These include birefringence, wavelength dependence of the index of refraction, and losses within the sample. It seems unlikely that any of these effects would be able to explain the trend seen in the degree of polarization of the PL, since the birefringence and wavelength variation of the index of refraction are small effects, and losses in the sample could be expected to make the trend go the other way (losses grow with photon energy and are greater for light polarized along the c-axis).

Bibliography

1. Shay, J. L. and J. H. Wernick. *Ternary Chalcopyrite Semiconductors: Growth, Electronic Properties, and Applications.* New York: Pergamon Press, 1975.

2. Goryunova, N. A., Kesamanly, F. P., and Osmanov, E. O. "Preparation and Some Properties of $CdGeAs_2$ Single Crystals," *Soviet Physics - Solid State, 5*: 1484 (1964)

3. Byer, R. L., Kildal, H. and Feigelson, R. S. "$CdGeAs_2$ - A New Nonlinear Crystal Phasematchable at 10.6 μm," Applied Physics Letters V 19 N 7: 237-240 (1971).

4. Okunev V. D. "Nonohmic Hopping Conduction in Amorphous $CdGeAs_2$" *Soviet Physics - Semiconductors Vol. 19 No. 12* :1367-1369 (1985)

5. Borshchevskii, A. S., Valov, Yu. A., Goryunova, N. A., Osmanov, E. O., Ryvkin, S. M., and Shpen'kov, G. P. "Radiative Recombination in $CdGeAs_2$ and $CdSiAs_2$ Crystals," *Soviet Physics - Semiconductors Vol. 2 No. 9*: 1145-1146 (1969)

6. Isomura, S., Takahashi, S., and Masumoto, K. "Electrical and Optical Properties of $CdGeAs_2$," *Japan. J. Appl. Phys, 16*: 1723-1724 (1977)

7. Shileika, A. "Energy Band Structure and Modulation Spectra of $A^2C^4C^5_2$ Semiconductors," *Surface Science, 37*: 730-747 (1973).

8. Akimchenko, I. P., Borshchevskii, A. S., and Ivanov, V. S. "Optical and Photoelectric Properties of $CdGeAs_2$,"*Soviet Physics - Semiconductors Vol. 7 No. 1.* 98-101 (1973)

9 Akimchenko, I. P., Ivanov, V. S., and Borshchevskii, A. S. "Electroreflection Spectra of Crystalline and Glassy $CdGeAs_2$,"*Soviet Physics - Semiconductors Vol. 7 No. 2*: 309-310 (1973)

10. Polygalov, Yu. I., and Poplavnoi, A. S. "Energy Band Structure of $CdSnAs_2$ and $CdGeAs_2$," *Soviet Physics Journal 24* : 1139-1142 (1981)

11. Madelon, R. ,Paumier, E., and Hairie, A. "Energy Band Structure Calculation of CdGeAs2 by Pseudopotential Method with Spin-Orbit Interaction," *Physica Status Solidi (b), 165*: 435-442 (1991).

12. Kildal, H. "$CdGeAs_2$ and $CdGeP_2$ Chalcopyrite Materials for Infrared Nonlinear Optics," Technical Report AFML-TR-72-277, Air Force Materials Laboratory, Air Force Systems Command, Wright-Patterson Air Force Base, Ohio (1972)

13. Borisenko, S. I., and Karavaev, G. F. "Energy Spectrum and Optical Absorption in p-$CdGeAs_2$" *Soviet Physics Journal 25* : 65-68 (1982)

14. Mamedov, B. Kh. and Osmanov, E. O. "Infrared Absorption in p-Type $CdGeAs_2$ Crystals," *Soviet Physics - Semiconductors Vol. 5 No. 7* :1120-1122 (1972)

15. Schunemann, P. G. et al. "Agile Laser Materials: Crystal Growth of $ZnGeP_2$ for Optical Parametric Oscillator Applications," Technical Report WL-TR-95-4028, Materials Directorate Wright Laboratory, Air Force Materiel Command, Wright-Patterson Air Force Base, Ohio (1995)

16. Iseler, G. W., Kildal, H., and Menyuk, N. "Optical and Electrical Properties of $CdGeAs_2$," *Journal of Electronic Materials Vol. 7 No. 6* : 737-755 (1978)

17. Borshchevskii, A. S., Dagina, N. E., Lebedev, A. A., Ovezov, K., Polushina, I. K., and Rud, Yu. V. "Photosensitivity of $CdGeAs_2$ to Linearly Polarized Radiation," *Soviet Physics - Semiconductors Vol. 10 No. 10* : 1136-1139 (1976)

18. Brudnyi, V. N., Krivov, M. A., Potapov, A. I., Polushina, I. K., Prochukhan, V. D., and Rud, Yu. V. "Change of Electrical Porperties in Electron Irradiated $CdGeAs_2$ Crystals," *Physica Status Solidi (a), 49*: 761-765 (1978).

19. Halliburton, L. E., Edwards, G. J., Schunemann, P. G., and Pollak, T. M. "Electron-paramagnetic-resonance spectra in as-grown $CdGeAs_2$," *Journal of Applied Physics, 77:* 445-437 (1995).

20. Varea de Alvarez, Carmen, Cohen, Marvin L., Kohn, S. E., Petroff, Y., and Shen, Y. R., "Calculated and measured reflectivity of $ZnGeP_2$," *Physical Review B,Vol 10. No. 12*: 5175-5183 (1974).

21. Babonas, G. et al. "Wavelength-Modulated Absorption Spectra of Pseudodirect Bandgap $A^2C^4C^5_2$ Compounds," *Physica Status Solidi (b), 62*: 327-334 (1974).

22. Averkieva, G. K. et al. "Photoluminescence of p-Type $ZnGeP_2$ Crystals," *Physica Status Solidi (a), 39*: 453-457 (1977).

23. Gorban, I. S. et al. "Luminescence of Zinc Germanium Diphosphide Crystals," *Sov. Phys. Semicond.*, 18: 892-893 (1984).

24. Hobgood, H. M. et al. "$ZnGeP_2$ Grown by the Liquid Encapsulated Czochralski Method," *Journal of Applied Physics, 73*: 4030-4037 (1992).

25. Ooe, A. et al. "Optical Studies on Off-Stoichiometry and Zn-Doping for $CuGaS_2$ Crystals," *Proceedings of the7th International Conference on Ternary and Multinary Compounds.* 471-476. Pittsburgh: Materials Research Society, 1987.

26. Gregg, Capt Michael R. *Cathodoluminescence Spectroscopy of Zinc Germanium Phosphide.* MS Thesis AFIT/GEP/ENP/92D-4. School of Engineering, Air Force Institute of Technology (AU), Wright-Patterson AFB OH, December 1992.

27. McCrae, J. E., Jr., Gregg, M. R., Hengehold, R. L., Yeo, Y. K., Ostdiek, P. H., Ohmer, M. C., Schunemann, P. G., and Pollak, T. M., "Polarized Luminescence Study of Ordered Nonlinear Optical Material $ZnGeP_2$," *Appl. Phys. Lett. V 64 N 23* : 3142-3144 (1994).

28. Sze, S. M. *Physics of Semiconductor Devices*. New York: John Wiley & Sons, 1981.

29. Pankove, Jacques I. *Optical Processes in Semiconductors*. New York: Dover Publications, 1971.

30. Saleh, B. E. A., and Teich, M. C., *Fundamentals of Photonics*. New York: John Wiley and Sons, Inc., 1991.

31. Boer, Karl W., *Survey of Semiconductor Physics*, Van Nostrand Reinhold: New York, 1990.

32. Press, W. H., Teukolsky, S. A., Vetterling, W. T., and Flannery, B. P. *Numerical Recipes in C.*(Second Edition) Cambridge: Cambridge University Press, 1992.

33. Dietz, N., Tsveybak, I., Ruderman, W., Wood, G., Bachmann, K. J., "Native Defect Related Optical Properties of $ZnGeP_2$," *Appl. Phys. Lett.* V 65 N 22: 2759-2761 (1994).

34. Aspnes, D. E. "Modulation Spectroscopy/Electric Field Effects on the Dielectric Function of Semiconductors" in *Handbook on Semiconductors, Vol. 2*. Ed. Minko Balkanski. Amsterdam: North-Holland, 1980.

35. Yu, P. Y., and Cardona, M. *Fundamentals of Semiconductors*. Berlin: Springer, 1996.

36. Pavesi, L. and Guzzi, M. "Photoluminescence of $Al_xGa_{1-x}As$ alloys," *Journal of Applied Physics, 75*: 4779-4842 (1994).

37. Blood, P. and Orton, J. W. *The Electrical Characterization of Semiconductors: Majority Carriers and Electron States*. London: Academic Press, 1992.

38. Fischer, D. W., Ohmer, M. C., and McCrae, J. E. "Effects of Temperature and Free Carriers on CdGeAs2 Birefringence", *To be Published.*

39. Demtroder, W. *Laser Spectroscopy: Basic Concepts and Instrumentation* (Second Edition) Berlin: Springer, 1996.

40. Hutley, M. C., *Diffraction Gratings*. London: Academic Press, 1982.

41. Klein, Miles V. and Furtak, Thomas E. *Optics*. New York: John Wiley and Sons, 1986.

Vita

Major Jack E. McCrae, Jr. was born on 10 October 1961 in Summit, New Jersey. He graduated from Middletown High School South in Middletown, New Jersey in 1980. He graduated from the Massachusetts Institute of Technology with a Bachelor of Science in Physics in June, 1984, obtaining a commission in the Air Force, through R.O.T.C. at the same time. He worked at the Air Force Weapons Laboratory, in Albuquerque, NM, from 1984 through 1989 as a Semiconductor Laser Development Project Officer. He was then assigned to the Ballistic Missile Organization, in San Bernardino, CA, where he was the Small ICBM Laser Ordnance Firing System Project Manager from 1989 through 1992. He entered the School of Engineering at the Air Force Institute of Technology in June 1992, and received a Master's Degree in September 1993.

Permanent Address: 49 Orchard Rd
South Burlington VT
05403

REPORT DOCUMENTATION PAGE

Form Approved
OMB No. 0704-0188

1. AGENCY USE ONLY (Leave blank)	2. REPORT DATE	3. REPORT TYPE AND DATES COVERED
	22 Jan 97	Dissertation

4. TITLE AND SUBTITLE

Investigation of the Optical Properties of Ordered Semiconductor Materials

5. FUNDING NUMBERS

6. AUTHOR(S)

Jack E. McCrae, Jr., Major, USAF

7. PERFORMING ORGANIZATION NAME(S) AND ADDRESS(ES)

Air Force Institute of Technology
Engineering Physics Department
WPAFB, OH 45433-6583

8. PERFORMING ORGANIZATION REPORT NUMBER

AFIT/DS/ENP/97-03

9. SPONSORING / MONITORING AGENCY NAME(S) AND ADDRESS(ES)

Dr Mel Ohmer
WL/MLPO
2977 P Street, Suite 1
WPAFB OH 45433-7734

10. SPONSORING / MONITORING AGENCY REPORT NUMBER

11. SUPPLEMENTARY NOTES

Distribution unlimited; Approved for public release

12a. DISTRIBUTION / AVAILABILITY STATEMENT

12b. DISTRIBUTION CODE

13. ABSTRACT *(Maximum 200 words)*

Optical Studies have been conducted upon $CdGeAs_2$ and $ZnGeP_2$, two of the most promising semiconductors being developed for mid-infrared non-linear optics applications. These experiments included photoluminescence (PL) studies of both compounds as well as photoreflectance (PR) measurements upon $CdGeAs_2$. In addition, Hall effect measurements were carried out upon $CdGeAs_2$, to aid in interpretation of the optical data. PL was measured as a function of laser power, sample temperature, and crystal orientation for $CdGeAs_2$. One broad weak peak near 0.38 eV, and another somewhat narrower and often far brighter peak near 0.57 eV were found by low temperature (4 K) PL measurements. Strongly polarized PL was observed with the E field of the PL parallel to the material's c-axis. A polarization ratio as high as 6:1 was observed. PL on $ZnGeP_2$ in the mid-IR revealed a previously unreported PL peak near 0.35 eV. PR measurements on $CdGeAs_2$ allowed the estimation of the bandgap as a function of temperature. Hall effect measurements on $CdGeAs_2$ reveals the dominant acceptor level lies about 120 meV above the valence band.

14. SUBJECT TERMS	15. NUMBER OF PAGES
Cadmium Germanium Arsenide, Zinc Germanium Phosphide, Photoluminescence, Semiconductors, Non Linear Optics,	156
	16. PRICE CODE

17. SECURITY CLASSIFICATION OF REPORT	18. SECURITY CLASSIFICATION OF THIS PAGE	19. SECURITY CLASSIFICATION OF ABSTRACT	20. LIMITATION OF ABSTRACT
UNCLASSIFIED	UNCLASSIFIED	UNCLASSIFIED	UL